FINAL REPORT

U.S. DOT
Pipeline and Hazardous Materials Safety Administration

Competitive Academic Agreement Program

Glass-Polymer Composite High Pressure Pipes and Joints - Design, Manufacture & Characterize

West Virginia University

CAAP Final Report

Date of Report: September 29, 2018

Contract Number: *DTPH5616HCAP02*

Prepared for: U.S. Department of Transportation/Pipeline and Hazardous Materials Safety Administration (USDOT-PHMSA)

Project Title: Glass-Polymer Composite High Pressure Pipes and Joints - Design, Manufacture & Characterize

Prepared by: West Virginia University, Constructed Facilities Center (WVU-CFC)

Project PI/co-PI: Hota V. S. GangaRao, Udaya B. Halabe, John Zondlo, Mark Skidmore
Graduate Students: Ben Imes, Jonas Kavi, Andrew Pacifico, Ronald Alexander, Andrew Cvetnick, Patrick Sisler

Contact Information: Dr. Hota V. S. GangaRao, Professor, CEE Department, WVU

Email: *Hota.Gangarao@mail.wvu.edu*

Phone: 304-293-9986

Project ending date: *September 29, 2018*

Acknowledgement

The authors gratefully acknowledge the funding for this project provided by USDOT-PHMSA's Competitive Academic Agreement Program under Contract No. DTPH5616HCAP02.

Executive Summary

The United States of America has about 2.65 million miles of distribution mains plus transmission lines. Even though it has been established that smaller diameter pipelines are safer to operate, gas pipeline industry needs cost-effective ways to transmit larger volumes of gas over long distances at higher pressures with at least 50 years of service life. Recognizing that current gas pipelines are made primarily of steel which is subjected to corrosion and hydrogen embrittlement, the proposed project focuses on developing glass fiber reinforced polymer (GFRP) composite pipes including a range of joining systems. A few of the many advantages of GFRP composite pipes are their non-corrosiveness, magnetic transparency, and high strength-to-weight ratio. As a part of this project, GFRP pipes and joints were designed, manufactured, and evaluated under static loads. Emphasis was placed in the evaluation of stress-rupture (burst pressure) of GFRP composite pipes that could withstand internal pressures as high as 5000 psi. The report also includes design and testing of high pressure composite joints for these pipes. In addition, the report discusses the use of Ground Penetrating Radar (GPR) for successfully detecting the FRP pipes under buried condition. The report also includes detection of gas leakage from buried pipes using mass spectroscopy.

Table of Contents

List of Figures

List of Tables

1 INTRODUCTION

1.1 Background

The United States of America (USA) has about 2.15 million miles of small diameter (≤6 inch) low pressure natural gas distribution mains and service pipelines. In addition, it has about 0.5 million miles of transmission and hazardous liquid pipelines (USDOT-PHMSA). These gas transmission lines need to be larger in diameter, withstanding higher operating pressures (~ 5000 psi) for economic reasons. Such line pressures can be achieved economically by developing glass-polymer composite pipelines including innovative joining mechanisms. In the USA, approximately 60% of the gas transmission lines are 30 inch in diameter or higher, and mostly made of steel. Even though it has been established that smaller diameter pipelines (≤6 inch) are safer to operate, gas pipeline industry needs to find safe and cost effective ways to transmit larger volumes of gas over long distances at higher pressures [1-6]. For example, existing gas transport technology has to improve pipeline system service-life from 20 to 50 years at higher pressures by: i) overcoming fire hazard from permeation leaks or shrinkage related nano-cracks due to improper/inadequate cure; ii) improving explosion and rupture resistance due to stress-rupture and/or installation related gouging; iii) enhancing corrosion resistance and associated durability response from moisture and pH variations; and iv) adequately designing for a wide range of serviceability factors.

The gas pipeline industry recognizes that steel pipelines are subject to stress-corrosion, hydrogen embrittlement and many other technical challenges including the need for higher line pressures (~ 5000 psi) and longer service life. In spite of recent advances made to overcome corrosion related degradation in gas pipelines, many major technical challenges to pipeline design, manufacture and installation are: i) service-life of at least 50 years with minimal maintenance costs; ii) operating pressures around 2000 psi without stress-rupture and stress-corrosion concerns for the pipelines as well as joints; iii) ease of installation, line location and leak detection; iv) ease of maintenance through nondestructive evaluations; v) cost-effectiveness of manufacture, installation and repair; vi) other safety related functional parameters.

The Achilles heel in designing, maintaining and installing any complex pipeline system is the integrity and durability of joining mechanisms of pipes varying in length from 40 to 80 feet.

Typical joining mechanisms are butt-wrap joint, tongue-groove joint, flanged joint, threaded and bonded joint, matched-taper joints and many others. An additional challenge is to attain design adequacy for time-dependent stress rupture threshold under operating pressures of around 5000 psi and sustain operational integrity over 50 years of service life. Herein, service-life predictions for glass-polymer composites become complex under both the material and bond degradations due to gaseous permeation, especially at elevated internal pipeline pressures (~5000 psi) and also at marginally elevated temperature (~160-180^{0}F) for gathering and transmission lines. The majority of the above said issues will be evaluated by the research and development activities proposed hereunder.

1.2 Safety

The USDOT-PHMSA oversees the development and implementation of federal pipeline safety regulations and ensures compliance with federal safety regulations. The USDOT-PHMSA investigates pipeline accidents and enforces compliance with reference to remedial actions, and even assesses penalties for any violations.

Even though underground pipelines are considered safer than truck or train transport of oil and gas, on average ~100 deaths and serious injuries are reported each year in the pipeline industry. These types of accidents can grow with the advent of transporting higher volumes of natural gas at higher operating pressures. The trends in field implementation are pointing towards the higher use of glass fiber reinforced polymer (GFRP) composite pipelines as an economical alternative to conventional steel pipeline systems due to GFRP’s inherent advantages of nonconductive and nonmagnetic material properties coupled with higher (~8 times) strength to weight ratios [6]. Thus, importance of proper design, manufacturing and field installation of GFRP pipes and joints becomes paramount to avoid unsafe engineering practices and to increase their service life [1-24].

1.3 Research Objectives

To help address some of the major challenges associated with transportation by pipelines, this research aims to develop high pressure GFRP pipes through the following objectives:

1. Develop GFRP pipes capable of resisting high burst pressures.
2. Develop high pressure joints to connect the GFRP pipes.

3. Characterize the behavior and failure mechanisms for GFRP pipes under high pressure.
4. Develop theoretical correlation to predict experimental behavior.
5. Investigate the detectability of the above pipes in buried state using Ground Penetrating Radar (GPR).
6. Investigate the possibility of buried pipe/gas leak detection using Spectroscopy.

2 FRP PIPE DEVELOPMENT

2.1 Introduction

Over the last 18 months, Kenway Corporation, a subsidiary of Creative Pultrusion Inc, has provided two batches of GFRP pipes and two batches of GFRP pipe joints for researchers at WVU-CFC to test and analyze. In addition to the pipes, Kenway also provided a report, prepared by the Advance Engineering Wood Center (AEWC) at the University of Maine, detailing the constituent properties, fiber contents, and longitudinal and hoop strengths. Furthermore, Kenway provided the fabric architectures for the two batches of pipes. This data was used throughout this research project for modelling and for comparison with experimental and analytical results.

The pipes were subjected to burst pressure testing. The testing methodology and results for these tests are discussed later in the chapter. In tandem with pressure testing, analytical processes to evaluate elastic properties and failure properties were explored. Since the beginning of the project, the endeavor has been to, not only test and characterize pipes, but also to produce simple methods to predict these failure pressures.

2.2 Kenway Pipe Specifications

Throughout this chapter, the two batches of filament wound (FW) pipes are considered separately. The pipes are discussed in terms of specifications and geometry, elastic properties, and failure properties. The joints were tested to failure under internal pressure, but have not been evaluated from this mechanics based perspective.

2.2.1 Filament Wound Pipes- ⅜ Wall Samples

2.2.1.1 Dimensions

During the first round of pressure tests, Kenway generously provided three 36-inch long filament wound pipes, and two 48-long jointed pipes for pressure testing. The three pipes and joints have average inner diameters of 9.30 inches and average wall thicknesses of 0.45 inches. By a slim margin, these pipes fall into the category or thin-walled pipes. The D/t ratio is 20.66, slightly over the lower limit value of 20. Therefore, the thin-walled approximation was employed in both analytical and experimental analyses for the first batch of pipes. Since the thin-walled approximation is met, the wall is viewed as a laminated plate, subjected to only longitudinal and hoop stress.

Figure 2-1: *Kenway filament wound pipes*

The main constituent materials in the pipes are E-glass and vinyl ester resin. The fiber content by weight was determined to be 66 percent. Thus, dividing by densities of the constituents, the fiber volume fraction was found to be 47.8 percent. The resin volume content is 52.2 percent. Fiber content was determined in accordance with ASTM D2584, “Standard Test Method for Ignition Loss of Cured Reinforced Resins”.

2.2.1.2 Fiber Architecture

The fabric architecture of the first batch of pipes consists of two primary layers, the corrosion barrier layer (which is not assumed to contribute significant strength or stiffness) and the structural layer. The corrosion barrier layer is around 0.1 inches thick and is primarily provided to offer corrosion resistance against materials within the pipe, although it does offer some strength. The majority of the strength and stiffness comes from the structural layer, which is 0.35 inches thick. These three pipes are henceforth referred to as ⅜ wall pipes, for the approximate thickness of the structural layer. The details of the layup are mentioned below, to the extent Kenway provided.

1. Resin Rich Corrosion Barrier Layer (0.1” to 0.128” thick)

    a. One layer of Nexus Surfacing Veil
    b. Two layers pf 1.5 oz/ft^2 chopped strand mat
2. Structural Layer (0.33” to 0.35” thick)
    a. One layer of 0.75 oz/ft^2 chopped strand mat
    b. Nine layers of ±55 degree filament winding

2.2.2 Filament Wound Pipes- ¾ Wall Samples

2.2.2.1 Dimensions

The second round of tests, also involved three 36-inch long specimens. The pipes have an inner diameter of 9.625” inches and an average wall thickness of 0.8 inches. The second set of pipes was manufactured so that the effective thickness could be doubled between the two batches. The effective thickness was considered to be the thickness of the structural layer. Therefore, the resin rich zone remained 0.1 inches thick, while the structural layer thickness was doubled from 0.35 inches to 0.7 inches. These pipes are henceforth referred to as ¾ wall pipes. This second set of pipes was tested to investigate the possibility of a law of diminishing return. Researchers wanted to determine whether doubling the thickness of the structural layer would result in doubled pressure capacity.

2.2.2.2 Fiber Architecture

The fabric architecture of the second batch of pipes consists of three primary layers, the corrosion barrier layer and two structural layers.

1. Resin Rich Corrosion Barrier Layer (0.1” to 0.128” thick)
    a. One layer of Nexus Surfacing Veil
    b. Two layers pf 1.5 oz/ft^2 chopped strand mat
2. Structural Layer One (0.33” to 0.35” thick)
    a. One layer of 0.75 oz/ft^2 chopped strand mat

        b. Nine layers of ±55 degree filament winding

3. Structural Layer Two (0.33” to 0.35” thick)
    a. One layer of 0.75 oz/ft^2 chopped strand mat
    b. Nine layers of ±55 degree filament winding

2.3 Manufacturing of FRP Pipe

The process of filament winding involves the wrapping of many continuous strands of fiber or continuous mats around a mandrel. The mandrel is made from one of several different materials, such as plywood, aluminum, and steel. Once again, the fibers are wetted by being run through a resin bath prior to wrapping around the mandrel. The member is then cured through the application of heat lamps or by being fed through an oven. Once curing is initiated, shrink-wraps are employed to minimize voids. Shrink-wrap is a flexible, thin plastic that is wrapped around the specimen to provide uniform pressure. The wrap is removed after the curing has finished (GangaRao, Taly, & Vijay, 2007). A key advantage provided by filament winding is the ability of the process to produce a fabric architecture with fibers running in the magic angle. That is to say that fibers run at plus/minus 54 degrees. This angle is the optimum angle for pipes because the combination of hoop stress and longitudinal stress, created by internal pressures, act along this angle. **Figure 2-2** below shows a typical filament-winding machine (GangaRao, Taly, & Vijay, 2007).

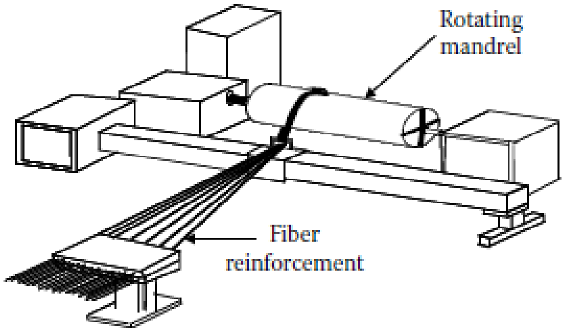

Figure 2-2: *Filament winding machine*

2.4 Hydrostatic Pressure Test Methodology

The main goal of this research is testing of FRP pipe under internal hydrostatic pressures until burst or other failure, thus this section includes a description of the end-closures, the test frames, the testing process, and the types of specimens used in this testing.

2.4.1 Loading System

2.4.1.1 Endcaps

Burst pressure testing introduces a unique challenge that static and fatigue testing do not encounter, i.e.; high magnitudes of hoop and longitudinal forces. The resultant force on each endcap is the product of internal pressure and internal area of the endcap. Thus, large diameter (>10 inch) pipes (large endcap surface area) under high pressures experience high magnitudes of longitudinal forces (200-600 kips). Since cyclic and static tests are conducted under operation pressures, the test pressures are 10 to 20 percent of the burst pressures. Therefore, the longitudinal forces on the endcaps are 5 to 10 times higher during burst pressure tests than for static and cyclic tests, for pipes of a given diameter. The initial project goal was to produce a pipe with a burst pressure of 30,000 psi, which for a 10 inch diameter pipe results in an endcap force of 2.3 million pounds. While end-closures of this type may exist, the closures would likely only be used for one test each, since chemical bonding would be required. The more economical expense of reusable endcaps was preferred. Therefore, burst pressure testing of free-end systems was determined to be unreasonable for this project.

For each of the pipes tested during this project, a restrained-end closure was used using steel to resist the loads and nitrile O-rings to seal. For initial evaluation, endcaps were designed based on the hoop stress equation for an internal pressure of 10,000 psi (factor of safety of 2 based on initial designs of 5,000 psi pipes). The endcaps (**Figure 2-3**) were fabricated from 2.5-inch thick Grade 50 steel. The inner diameter of endcap was machined to 10.000 inches, corresponding to a pipe with an outer diameter of 10.000 inches to match the dimensions of commercially available O-rings. The outer diameter of the endcaps is 14 inches, thereby creating a steel pipe with 2 inch wall thickness to fit around the end of the FRP pipe. The left cap in **Figure 2-3** shows the outer surface of one of the caps, where two fittings are located. These fittings were only installed in one end cap, and were used to fill the pipes and apply pressure during testing.

Figure 2-3: *Steel endcaps for 10 inch od pipe*

The cap was machined so that 1.25 inches of steel endcap would overlap the ends of the pipe. Furthermore, grooves were cut into the inner surface of the walls of the endcaps so that O-rings, for pressure sealing, could be inserted and compressed. The machining, grooves, and O-rings can be seen on the right cap in **Figure 2-3**.

Narrow tolerances were discovered to be a challenge during testing. Although steel can be machined to tolerances of 0.001 inches and 0.0001 inches, the outer diameter of filament wound pipes cannot be fabricated as precisely as the steel end caps. This issue arises because filament wound pipe thickness can only be increased by whole layers of fiber and resin. Furthermore, the filament-winding process does not always result in a perfectly round pipe. Therefore, the pipes were wound to be bigger than 10 inches, and then machined down to 9.995 inches up to 1.25 inches from the end of the each pipe. The smaller OD of the pipe was chosen based on the recommendations for the O-rings, as provided by the Parker O-ring handbook (Parker Hannaflin Corporation, 2007)) for the Parker 2-449 N552-90 O-rings used in the end caps. The endcaps were also machined to accept two backup rings (Parker 8-449 N1444-90) as recommended by Parker as the pressure was over 1500 psi. Full dimensions for the O-rings and backup rings is given in the Parker O-ring Handbook (Parker Hannaflin Corporation, 2007). The substantial wall thickness of the end caps over the pipe is much stiffer than the pipe, thus the steel reinforces the end of the pipe preventing a premature failure due to the machining. The FRP would also push into the steel with a greater and greater force as the internal pressure increased, thereby enhancing the seal and preventing leaks at high pressure. A machined pipe is seen in **Figure 2-4**. Prior to testing, a ¼ inch "round-over" was machined on the OD of the pipe to provide a smooth surface for endcap and O-ring placement.

Figure 2-4: *Machined pipe ends*

2.4.1.2 Load Frame

As shown in Figure 2-5, the test method used an oil-based hydraulic hand pump to load a ram which in turn pressurized water in a 5-inch diameter steel cylinder. The pressurized water was transmitted to the GFRP pipe through a high strength hydraulic line, entering the pipe through an end cap. Pressure was measured by a pressure transducer (rated for 50,000 psi). Thrust on the endcaps was resisted by a load frame holding a second 800-kip actuator, which held the endcaps secure on the pipe.

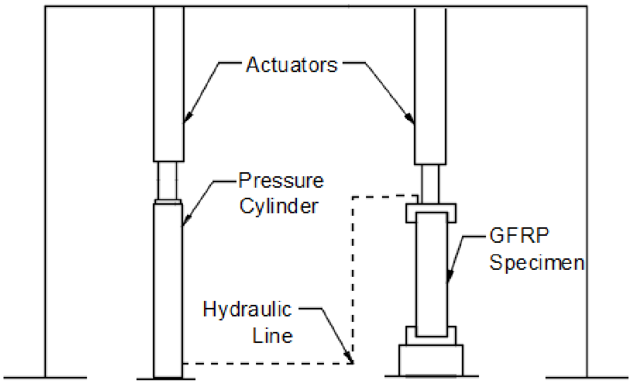

Figure 2-5: *Test frame*

Initial testing took place using existing load frames in the CFC Major Units Laboratory. Due to previous alterations on the existing frames, testing on the 10-inch pipes was limited to a maximum internal pressure of 2,300 psi. Testing was completed on the existing frames for the Creative Pultrusion (CP) samples and the butt joint samples, as they failed well below the frame capacity. Figure 2-6 shows two early iterations of the frame and actuator setup.

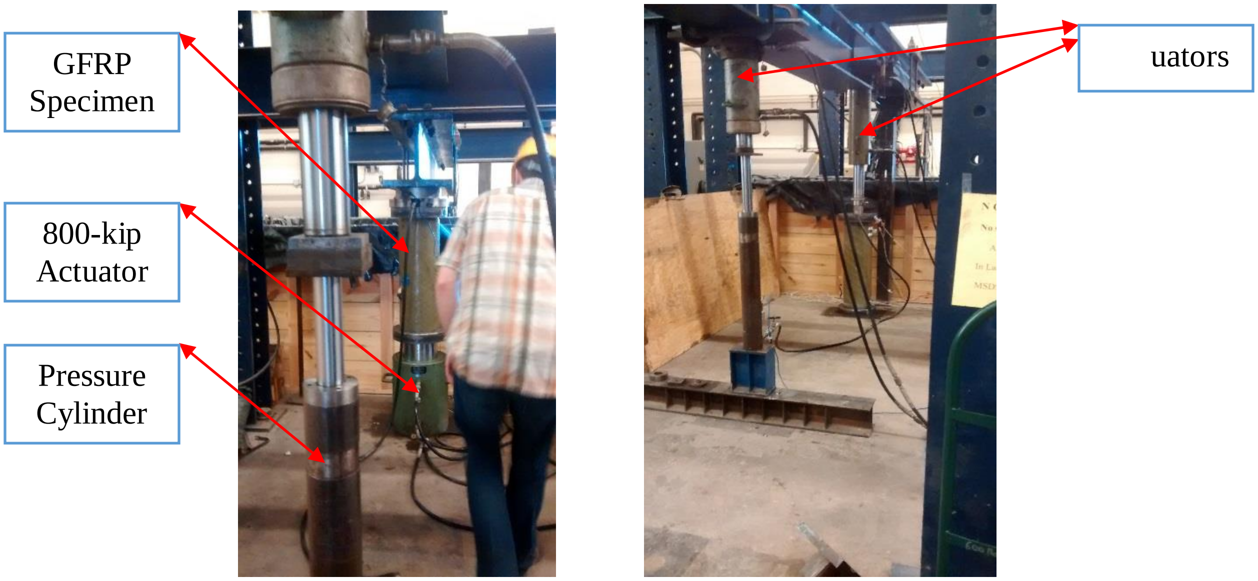

Figure 2-6: *Actuator and frame setup*

Due to the capacity limitations of the existing load frames, a new compression frame (Figure 2-7) was designed. The frame was designed to have minimal deformations under high loads, as the existing frames allowed significant deflection (up to 0.625 inches) under load. This deflection allowed the endcaps to come off the ends of the pipes, eventually resulting in the O-rings coming off the end of the pipe and the water to leak out.

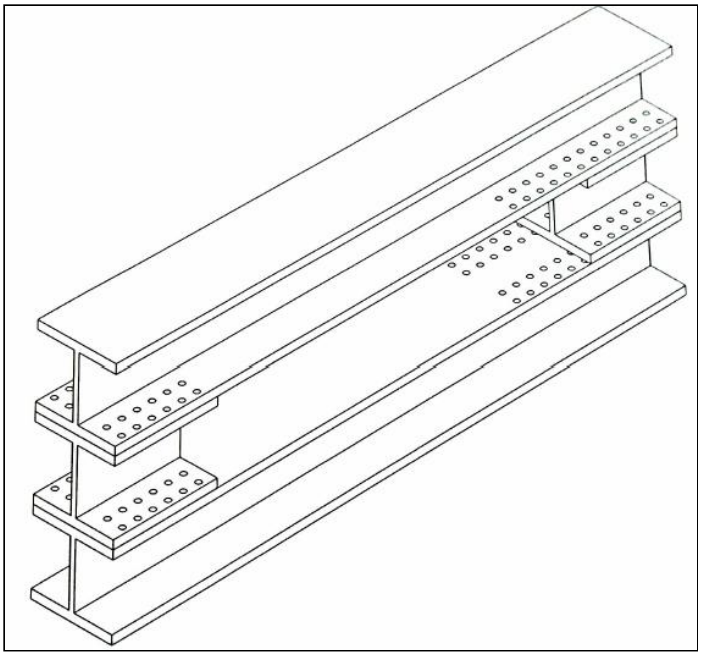

Figure 2-7: *Compression frame isometric view*

The compression frame was fabricated of four, W14 X 233, grade 50 steel beams, fastened together by 1-inch diameter, A490 bolts. Additional bolt holes were provided to allow the frame to be adjusted for lengths of pipe ranging from 30 to 72 inches. The pipe to be tested rests between 2 inch thick steel plates, which bear against a 800-kip actuator and then on the shorter beams. The actuator is used to make fine adjustments to the length of the sample between bolt holes and to push the end caps back onto the sample while it shrinks in length during testing. The actuator and steel plates are seen in **Figure 2-8**.

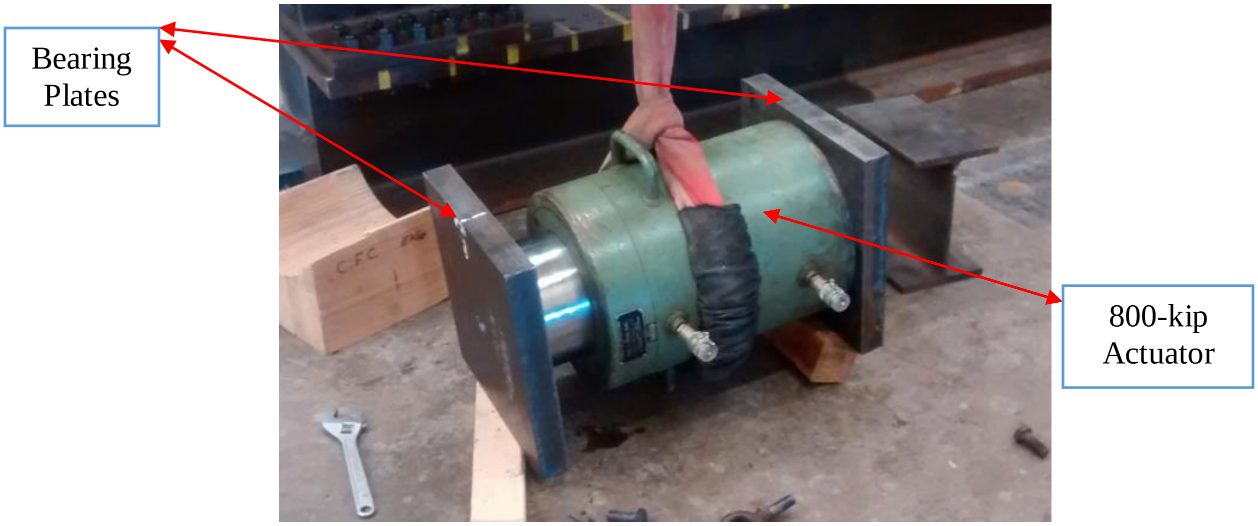

Figure 2-8: *800-kip capacity actuator and steel plates*

The two smaller beams experience compression stresses. Load is transferred to the two larger beams (120 inches long) through bolted connections of 24 bolts per flange. Therefore, the longer beams experience tensile stress and bending stress (due to the eccentricity of the bolted connections). This compression/tension frame provides high resistance to longitudinal deflection and endcap rotation. Details of the frame design and capacity are provided in the appendix. **Figure 2-9** shows the fabricated frame, the hydraulic actuator, and two of the three bearing plates.

Figure 2-9: *Compression load frame*

2.4.2 Samples and Testing

2.4.2.1 Filament Wound Pipes

Two batches (3 specimens each) of 10-inch diameter, filament wound (FW) GFRP pipes were also tested. The dimensions and architectures for these pipes are detailed in Chapter 4. **Figure 2-10** shows a pipe ready for testing; i.e. the end caps have been installed, it has been filled with water and connected to the hydraulic line. The pipe was placed horizontally into a timber cradle to hold the pipe in the frame without it rolling out.

Figure 2-10: *Test preparation*

Four strain gauges were placed on each pipe, near the midpoint along the length; two in the hoop directions, one in the longitudinal direction, and one in the fiber angle direction. The gauges and water pressure were monitored using a Vishay System 7000 Data Acquisition System collected data on all channels at 10 scans per second. The pressure was monitored using a Honeywell Pressure Transducer (Model 060-1108-13ZG-01) with a maximum pressure rating of 50,000 psi and an accuracy of +/- 50 psi.

As load was applied (through the hand pump), strain versus pressure data were collected. During testing, the pipes contracted and were coming out of the endcaps. As has been mentioned, this is because the hoop stress (in the absence of longitudinal stress) produces compression strain in the longitudinal direction (due to Poisson effect and fabric architecture). As the pipe contracted away from the endcaps, the water also caused a longitudinal compression force on the pipe, further causing it to shrink. Therefore, the 800- kip capacity actuator was periodically employed to push the endcaps back onto the pipe, which also served to increase the longitudinal force and internal pressure on the pipe. Therefore, the loading process was often a dynamic process of pumping on both actuators. This process ensured that the O-rings in the endcaps were able to seal to the pipe. Load was applied until leakage was observed in the walls of the pipe. Based on the data, stresses and loads were calculated. **Figure 2-11** shows a pipe in the frame during testing.

Figure 2-11: *Burst pressure testing*

2.5 Experimental Results

The pipe properties and test results, including strain, pressure and time, are presented in the following sections. The time to failure for each of the pipes was between 5 and 35 minutes. While this time exceeds the 60 to 70 seconds of ASTM 1599, creep effects are not believed to have been a significant factor in the results, as the previous testing up to 2300 psi was left for 100 minutes with no signs of failure.

2.5.1 Filament-Wound Pipes- ⅜ Wall Samples

Three thin-walled pipes (referred to henceforth as ⅜ wall) were tested under hydrostatic pressure until failure was observed. The pipes failed at an average pressure of 2,957 psi as evident via water spraying out of the walls (as opposed to weeping). Once water began to leak, rapid pressure loss was observed via the pressure transducer. The results from ⅜ wall pipe hydrostatic testing are provided in **Table 2-1**. It should be noted that hoop strains between the two gauges on a given pipe always measured different, albeit, slightly different. This difference would likely also be seen if additional gauges had been placed in the longitudinal and fiber angle directions. The failure pressures for the three pipes differed by 12 percent, average hoop strains for the three pipes at failure differ by 10 percent, longitudinal strains at failure differ by 31 percent, and fiber angle strains at failure differed by 43 percent. The time to failure for each of the pipes only differ by 8 minutes, suggesting that test time is most likely not responsible for differences in results.

Table 2-1: *Hydrostatic pressure test results- FW thin wall*

Specimen	Burst Pressure (psi)	Hoop A Failure Strain (μϵ)	Hoop B Failure strain (μϵ)	Average Hoop Failure Strain (μϵ)	Longitudinal Failure Strain (μϵ)	Fiber Angle Failure Strain (μϵ)	Time to Failure (min)
1	2,761	15,800	15,179	15,490	-13,425	7,219	12.8
2	2,969	16,622	17,919	17,270	-12,975	4,855	14.0
3	3,142	15,415	17,411	16,278	-19,475	4,085	20.9

The hoop stress equation (for thin walled pipes) was used to determine hoop stresses. Hoop stresses at failure were 28,711, 30,571, and 32,067 psi for pipes 1-3 respectively. **Figure 2-12** shows the stress/strain response until failure. The figure shows consistent hoop stress/strain response up to failure across the three pipes. This fact demonstrates that the test method produces consistent results, for the ⅜ wall specimens.

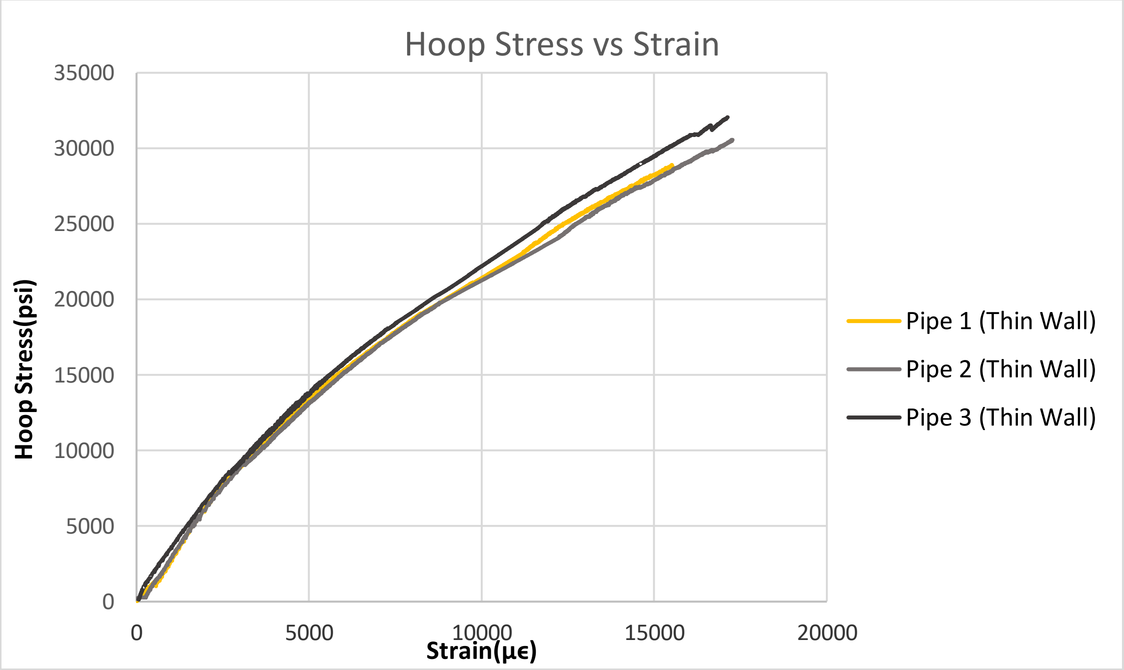

Figure 2-12: *Stress/Strain response of thin pipes*

The failure mode of these pipes was not catastrophic, unlike typical mechanical testing of composite pipes or the catastrophic failure of the 6-inch diameter pultruded pipe. Once a significant amount of pressure was lost, the pipes contracted and the leaks were sealed. **Figure 2-13** shows the pipe immediately after failure. No external damage was apparent, except a few small regions of discoloration, which typically indicates local delamination of layers. In some situations, one or two leaks appeared at the same moment, implying some degree of uniformity in damage progression. The light green region of the pipe in **Figure 2-14** shows the local delamination of the layers in the wall.

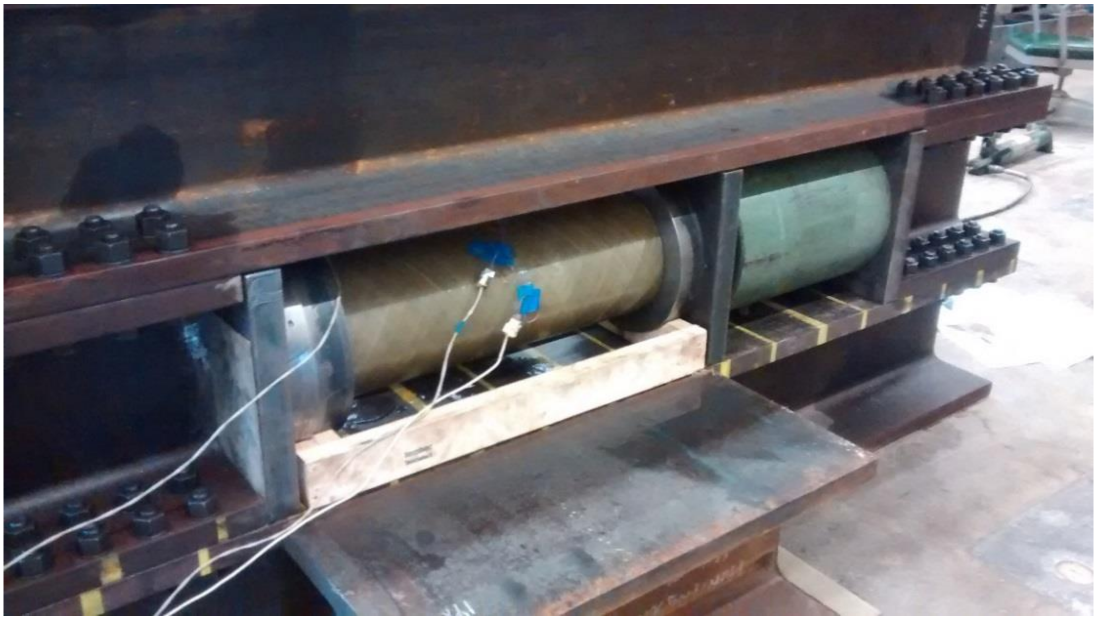

Figure 2-13: Pipe leakage

Figure 2-14: Local delamination

By contrast, the interior corrosion barrier layer (mainly composed of chopped strand mat) displayed significant delamination. The leaks first appeared in areas where the interior laminae had delaminated. Therefore, the failure appears to be primarily related to the resin and shear stresses. While the pattern of internal damage was not always consistent, in a few occasions, the resin appears to have failed in a helical progression. This helical failure is likely due to torsion stresses generated by the unsymmetrical architecture. While this torsion does not appear to have caused fiber failure, the torsion may have been the cause failure for the corrosion barrier. **Figure 2-15** shows the damage of the corrosion barrier layer.

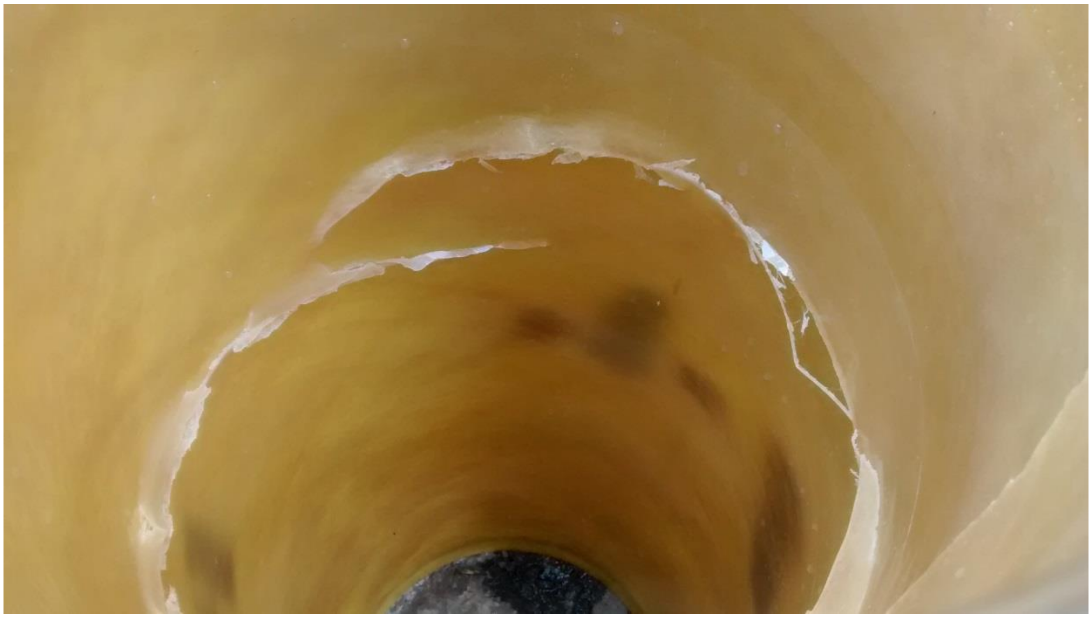

Figure 2-15: Damage to corrosion barrier

2.5.2 Filament Wound Pipes – ¾ Wall Samples

As has been mentioned previously, a second set of pipes was tested to evaluate the effects of increased thickness. The second set of pipes had an average thickness of 0.80 inches, and are referred to herein as ¾ wall as the filament wound thickness is nominal ¾ of an inch. Since these pipes were made with double the wall thickness, the burst pressure was expected to double as well.

As shown in

Table 2-2, specimens 1 and 2 failed at pressures near 5,200 psi (within 75 psi). However, specimen three failed at a much lower pressure of 4,000 psi. Furthermore, significant differences for the three samples in hoop and longitudinal strains at failure were observed (42 percent and 57 percent respectively). Differences in fiber angle strains differed in terms of tension/compression and magnitude. In general, greater variability of failure pressures, stresses at failure, and strains at failure were observed for the ¾ wall specimens than for the ⅜ wall specimens. One explanation for the variation in results could be the differing times to failure of nearly 23 minutes. It is possible that a faster load rate caused quicker failures, while the slower load rate allowed for greater damage progression prior to failure (i.e. higher stresses and strains to failure).

Table 2-2: *Hydrostatic pressure test results-FW thick wall*

Specimen	Burst Pressure (psi)	Hoop A Failure Strain (με)	Hoop B Failure Strain (με)	Average Hoop Failure Strain (με)	Longitudinal Strain at Failure (με)	Fiber Angle Strain at Failure (με)	Time to Failure (min)
1	5,172	26,477	23,045	24,761	-37,543	-467	34
2	5,247	11,927	15,617	13,770	-18,938	1,623	25
3	4,024	14,816	13,889	14,352	-16,274	-1,505	11

As with the ⅜ wall specimens, the hoop stress equation (for thin walled pipes) was used to determine hoop stresses for the ¾ wall specimens. Hoop stresses at failure are 32,758, 33,233 and 25,487 psi for these pipes 1-3 respectively. Stress/strain curves for the three thick wall pipes are provided in **Figure 2-16**. Fairly consistent stress/strain results are observed for the three pipes in the elastic zone (10 to 30 percent of ultimate stress), although specimen 2 does appear to have a slightly higher hoop modulus. However, the three pipes differed in terms of failure progression and failure strains. As failure progressed, differences became apparent. Stress/strain responses of pipes 1 and 3 trend well, except that pipe three failed under a much lower pressure. Pipe 2 and 3 have similar failure pressures and stresses, but differ in stress/strain response and failure strains.

The ¾ wall pipes exhibited similar failure modes as the ⅜ wall pipes. Once a leak developed, pressure was lost and the walls contracted. As with the ⅜ wall specimens, the external fibers did not break. Significant discoloration (typically observed in interlaminar delamination) were observed for specimen 1. Although exterior fiber breakage was not observed, the extent of the delamination (in specimen 1) was uniform (as evidenced by uniform discoloration). However, specimens 2 and 3 displayed only minor exterior discoloration. Delaminations were only observed locally.

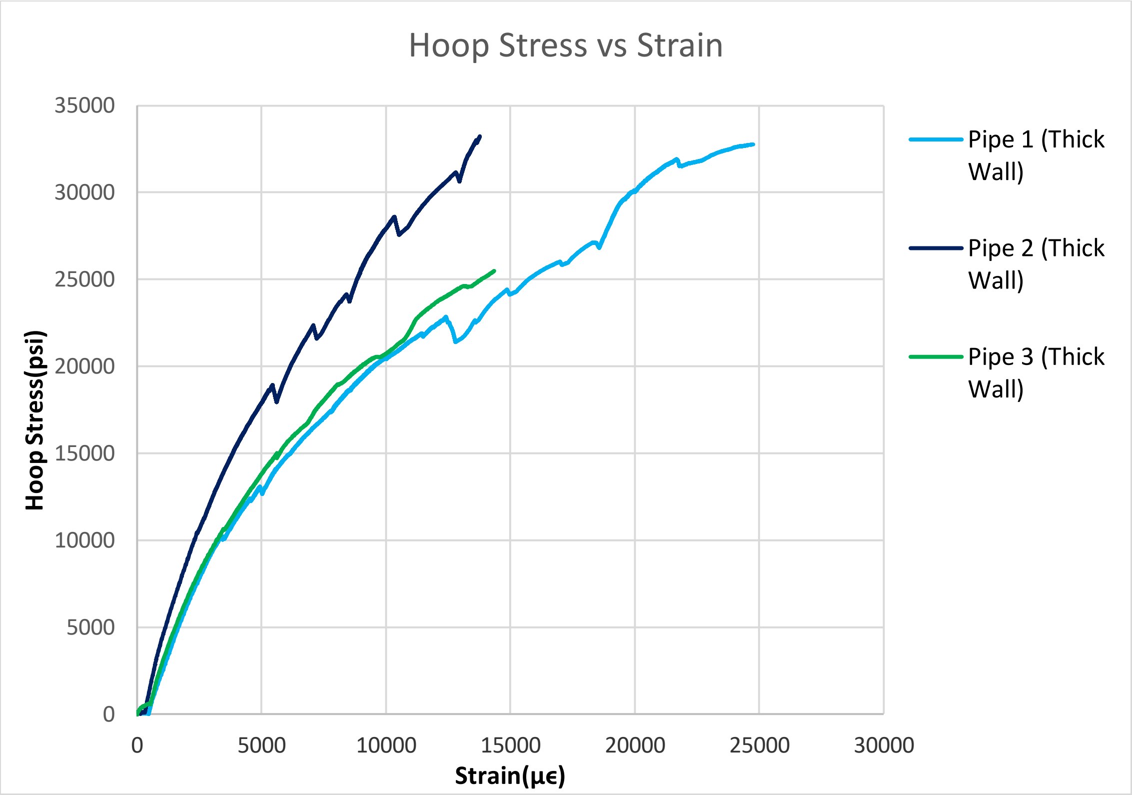

Figure 2-16: *Stress/Strain results of thick pipes*

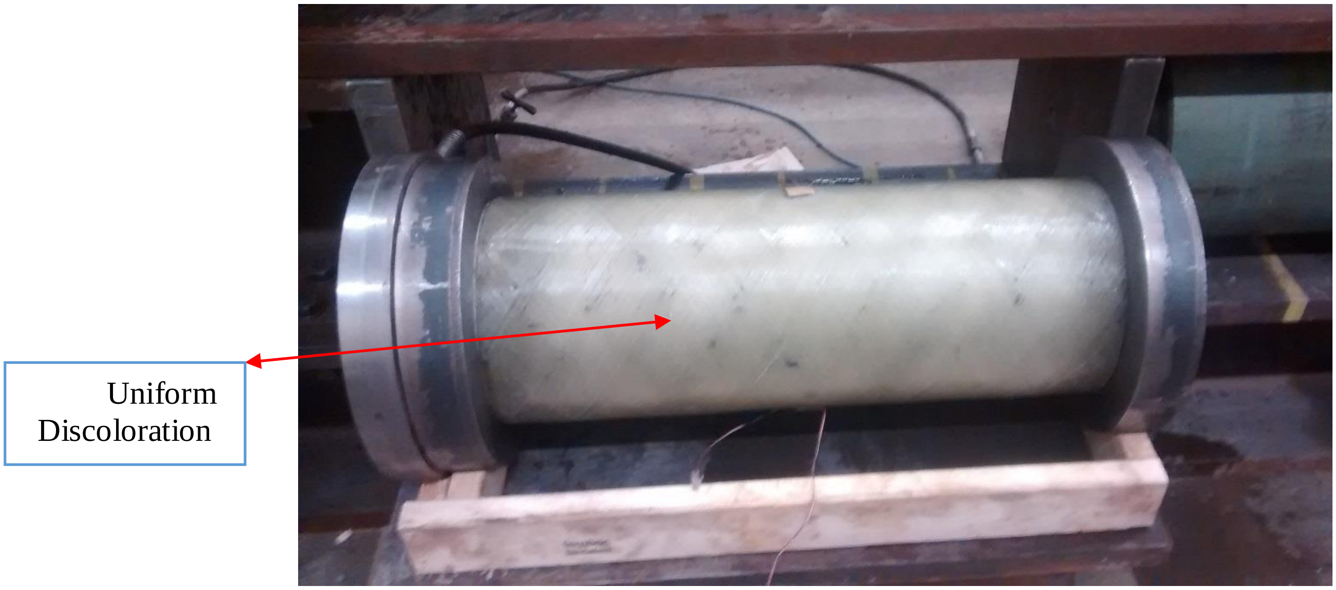

Figure 2-17: *¾ wall specimen 1 discoloration*

Figure 2-18: *Exterior damage of thick walled pipes*

The interior damage was also not consistent. Specimen 1, which exhibited the most exterior discoloration, displayed significant damage to the corrosion barrier layer. Specimen 2 displayed a small amount of interior damage and exterior discoloration. In comparison with specimens 1 and 2, specimen 3 appears to be an outlier. Specimen 3 displayed no interior damage and very little exterior discoloration. Specimen 3 developed only one leak and failed at an internal pressure 1,200 psi below that of specimens 1 and 2. Very likely, this could be due to manufacturing flaw. This is supported by the similar elastic behavior and failure progression to the specimen 1, the only difference between the two failure pressure and failure strains. However, no external flaws were visible prior to testing. Additional testing is required to statistically determine how often these premature failures may occur. Therefore, the failure modes do not appear to be as consistent as the thin wall pipes. Furthermore, failure modes are not consistent with the thin-walled pipes. Torsional failure of the resin rich barrier was not evident in the thick-walled pipes. **Figure 2-19** shows the interior damage of pipe two (left) and pipe one (right). **Figure 2-20** shows the interior damage pipe one (left) and three (right).

Figure 2-19: *Interior Damage of Specimen 1 and 2*

Figure 2-20: *Interior damage of specimen 1 and 3*

2.6 Conclusions

Hydrostatic burst pressure testing was conducted to evaluate elastic behavior, failure progression, and failure strengths of 6-inch diameter and 10-inch diameter filament wound GFRP pipes. The three thin-wall (0.45 inches thick) filament wound pipes failed at an average pressure of 2,957 psi through leakage. Thick-wall filament wound (0.8 inches thick) specimens 1 and 2 failed at an average pressure 5,210 psi through leakage. Thick-wall specimen 3 failed at 4,000 psi through leakage.

3 FRP JOINTS

3.1 Introduction

The pipe joints were subjected to burst pressure testing. The testing methodology and results for these tests are discussed later in the chapter.

3.2 Hydrostatic Pressure Test Methodology

Two GFRP butt joints and two CFRP scarf joints were tested. The GFRP butt joints were tested in an earlier configuration of the load frame. The butt joints were constructed of two thin-walled pipes (thickness 0.45 inches, ID 9.30 inches), butted together and wrapped with several layers of glass composite (0.375 inches thick). The CFRP scarf joints were fabricated from thin-walled pipes, with male/female type fittings, and several layers of carbon composite. The scarf joints were wrapped in carbon with the hope that the increased hoop stiffness, contributed by the carbon fiber, would contain the joint more successfully than the glass and allow for higher burst pressures. In addition to the four strain gauges placed on the pipes, four gauges were placed on the wrapped joint. **Figure 3-1** shows the pressure testing of the GFRP butt joints, in the early iterations of the load frame.

Figure 3-1: *GFRP butt joint pressure testing*

3.3 Experimental Results

Two GFRP wrapped butt joint samples were tested under hydrostatic pressure, and both failed at 1/3rd of the burst pressure due to water leaking between the external wrap and the outside of the pipe. Therefore, the bond of the GFRP wrap resin to the outside of the pipe was the limiting factor in the joint response. **Figure 3-2** shows the failure at the edge of the wrap, as well as discoloration due to delamination. **Figure 3-3** shows the wrap, which has pulled away from the outside surface of the pipe.

Figure 3-2: *Butt joint failure*

Figure 3-3: *Delamination of wrapped butt joint*

Strain gages were installed on the pipe 2 inch from the wrap and on the wrap itself, with the results summarized in **Table 3-1**. The hoop strain in the pipe was greater than the hoop strain in the wrap, indicating that the pipe was expanding into the wrap which should result in a better seal. However, the test results show this mechanical advantage was not enough to prevent leakage. The longitudinal strains were also significantly lower in the wrap, indicating the pipe may be pulling out of the wrap.

Table 3-1: *GFRP wrapped butt joint results*

Specimen	Failure Pressure (psi)	Pipe Hoop Strain at Failure	Pipe Longitudinal Strain at Failure	Wrap Hoop Strain at Failure	Wrap Longitudinal Strain at Failure	Time to failure (min)
Joint 1	1,116	4,769	-3,417	1,989	-567	8.4
Joint 2	1,294	6,048	-4,554	2,412	-1,737	8.3

Although the jointed pipes did not fail, their behavior can be compared to the burst test results. The hoop strain in the pipe for the joint samples was higher at the failure pressure than during the burst samples as the average strain in the burst samples was 4,105 at 1,116 psi and 4,953 at 1,294 psi. Similarly, the Poisson ratio for the joint tests during hydrostatic loading averaged 0.66 vs. 0.98 for the burst tests. Given the limited number of samples, it is not known if these differences are due to natural variability in the samples, test variations, or because of mechanical responses differences between a jointed and non-jointed pipe.

3.4 Scarf Joints

The GFRP scarf joints were fabricated from thick-walled pipes, with male/female type fittings, and several layers of glass composite. The scarf joints were constructed of two thick wall (0.8 inch thick) pipes, wrapped together with several layers of glass composite (Figure 3-4 and Figure 3-5).

Figure 3-4: *GFRP scarf joints*

.

Figure 3-5: *GFRP scarf joint test*

The scarf joint failed under 2,800 psi, internal pressure, in the same failure mode as the butt joints. The increased capacity of the scarf joints reveals an incremental step in the right direction. However, additional joint development is needed to provide a factor of safety for the joints.

3.5 Conclusions

Hydrostatic burst pressure testing was conducted to evaluate elastic behavior, failure progression, and failure strengths 10-inch diameter filament wound GFRP pipe joints. The GFRP joints failed at pressures near 1,000 psi. The filament wound pipe joints all failed at near hoop stresses of 30,000 psi.

4 THEORETICAL CORRELATION

4.1 Introduction

This chapter focuses on the review and development of the mechanics of materials based approach through which composite laminate pipes are evaluated in terms of elastic behavior. The in-plane and out-of-plane stresses and strains are evaluated in the layers of a laminate using the principles of the classical lamination theory (CLT). The secondary purpose is to discuss methods used to predict composite pipe burst pressures using CLT. These predictions are produced through stress/strain analysis, coupled with material failure strengths and failure criteria. Since steel pipes are predominately used in the natural gas industry, composite pipe behavior is developed in relation to steel pipe behavior. Furthermore, many of the mechanics principles employed in steel pipes can be used to approximate mechanics principles in composite pipes.

4.2 Thin Walled Isotropic Cylinders

The majority of pipes used in the natural gas industry have relatively thin walls in comparison to the inner diameter of the pipes. This is done for the sake of economy. The cost and weight of pipe are the two main factors employed in determination of a pipe's wall thickness and operational pressure. That is to say, design engineers must work within a pipeline project budget by determining the minimum required thickness of wall for a given operational pressure, for a specified service life. This steel pipeline design process requires the implementation of mechanics principles, which are well established and simplified in design codes [32]. Unfortunately, mechanical evaluations of pipes are carried out differently for isotropic and orthotropic (composite) materials; the latter (composites) being the more computationally rigorous of the two. While composite pipe analysis differs significantly from steel pipe analysis, many of the distinctions, assumptions, and principles used for steel pipe can be applied to composites pipe. Therefore, the analysis of steel pipe is briefly addressed in the next sections, so that composite mechanics can then be discussed.

4.2.1 Assumptions

A key distinction is that the pipe is thin walled. A thin walled pipe is defined as having a radius to thickness ratio greater than 10 (although the number is disputed and may actually be 20)

[25, 33]. In these circumstances, the relatively thin wall allows engineers to make simplified free body diagrams, which are used to determine the loads and stress that act within a pipe. This distinction of radius to wall thickness allows for the following assumptions.

The first assumption, for thin walled steel pipes, is that stresses and strains in the radial direction are neglected. The magnitude of the radial stress is very small in comparison to the high magnitudes of the longitudinal and circumferential stresses. This assumption is key because it allows designers to treat the state of stresses as plane stress, thus removing the third dimension of analysis (two dimensional stresses and strains).

The second assumption for thin-walled steel pipes is that the longitudinal and circumferential stresses are taken as an average constant across the thickness of the pipe. In reality, the circumferential stresses in isotropic pipes wall vary, with the highest magnitude of stress at the inside edge of the wall (for pipes under internal pressure) [25]. Furthermore, stresses in composite materials vary layer to layer, depending on the orientation of the fiber architecture. **Figure 4-1** provides a visual representation of the actual radial and hoop distributions in the walls of a steel pipe.

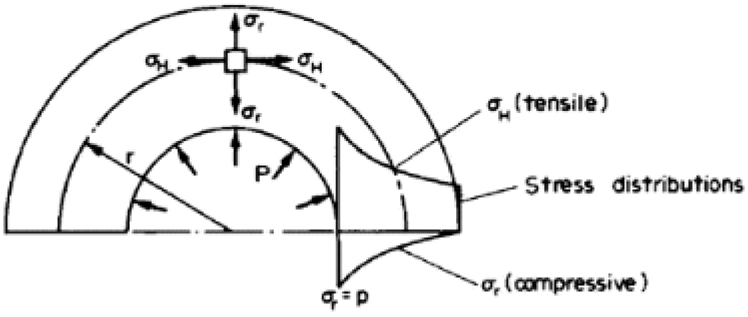

Figure 4-1: Hoop and radial stresses [25]

4.2.2 Determination of Stresses

Based on these assumptions and appropriate free body diagrams, equations for both the longitudinal and hoop stresses can be determined. These equations are the basis of pipe strength evaluations. **Figure 4-2** shows the free body diagram used in the determination of average circumferential (hoop) stresses and longitudinal stresses.

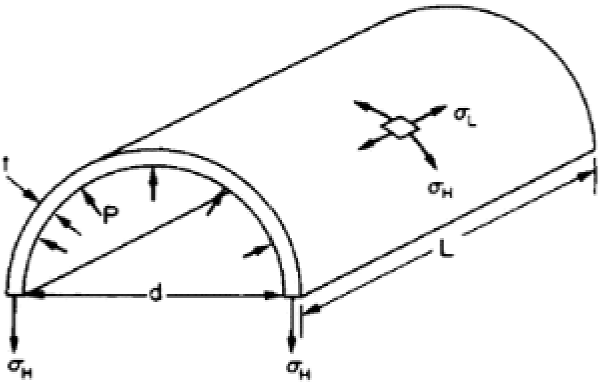

Figure 4-2: *Hoop stress FBD [25]*

Based on the free body diagram, the internal force on half of the pipe is a product of pressure, length, and inner diameter. The area resisting this force a product of thickness, and length. Thus, per laws of force equilibrium, the hoop (circumferential) stress is given by Equation 4-1. P is the internal pressure, r is the radius, and t is the wall thickness of the pipe.

$$\sigma_{Hoop} = \frac{(p * r)}{t} \tag{4-1}$$

The longitudinal stresses are determined in similar fashion. Considering force equilibrium in the longitudinal direction, the longitudinal stress is given by Equation 4-2. Again, p is the internal pressure, r is the radius, and t is the thickness. As can be seen, the longitudinal stresses are half that of the hoop stresses.

$$\sigma_{Longitudinal} = \frac{(p * r)}{2 * t} \tag{4-2}$$

Based on the free body diagram, the principal stresses are then $\sigma_H = \sigma_1, \sigma_L = \sigma_2,\ \sigma_r = 0$. Since these stresses are oriented in the principal directions, no shear stresses exist.

By contrast, general equations for stresses in thick-walled cylinders have also be produced. These equations were produced by Lamé, and can apply to thin-walled cylinders or thick-walled cylinders. In the general solutions, the effects of radial stress are not neglected. Furthermore, hoop stress are not assumed to be uniform. The equations for hoop, longitudinal, and radials stress are given by Equations 4-3 to 4-5, where p is the internal pressure, r_i is the inner radius, r_o is the outer radius, and r is the location of the stress across the wall thickness. r ranges from r_i to r_o.

$$\sigma_{Hoop} = \frac{(p * r_i^2)}{(r_o^2 - r_i^2)} + \frac{(r_i^2 * r_o^2 * (-p))}{(r^2 * (r_o^2 - r_i^2)} \tag{4-3}$$

$$\sigma_{Longitduinal} = \frac{p * r_i^2}{r_o^2 - r_i^2} \tag{4-4}$$

$$\sigma_{Radial} = \frac{(p * r_i^2)}{(r_o^2 - r_i^2)} - \frac{(r_i^2 * r_o^2 * (-p))}{(r^2 * (r_o^2 - r_i^2)} \tag{4-5}$$

Once principal stresses are determined by either the thin wall equations or Lamé's equations, the principles of Hooke's law can be applied to determine strains. From there, failure theories/criterion can be applied to predict failure pressures [25]. Since, isotropic and orthotropic materials differ greatly in elastic behavior and failure behavior; the two materials are henceforth addressed separately. Focus is placed on orthotropic materials.

4.3 Thin Walled Composite Cylinders

As has been discussed above, the mechanics principles, distinctions, and assumptions that apply to isotropic materials can also be applied orthotropic (quasi-isotropic) materials. Based on Equations 4-1 and 4-2, pipes under internal pressure experience a magnitude of hoop stress that is twice that of the longitudinal stress. Therefore, isotropic materials are twice as strong as necessary in the longitudinal direction. By contrast, composite pipes can be manufactured in a way that allows fibers to be wound at an angle (cross ply architecture), satisfying the strength requirements of the hoop and longitudinal stresses and reducing the required material and wall thickness.

Many researchers have sought to determine the optimal winding angle analytical and experimentally. The value has been found to be 54.7 degrees. This is known as the "magic angle." Since filament winding allows for tremendous precision in fiber placement, composite pipes, intended for pressurized applications, are commonly fabricated through this process. These pipes include corrosion barriers (resin rich zones with veils, and quasi-isotropic chopped-strand mats), and layers of unidirectional fibers wound at ± 55 degrees. The winding angle may differ slightly depending on a manufacturer's capabilities [26].

4.4 Elastic Behavior of Orthotropic Materials

4.4.1 Classical Lamination Theory (CLT)

Composite materials are a nonhomogeneous combination of constituent materials and fall into the category of orthotropic materials. In contrast to isotropic materials, orthotropic materials have three planes of symmetry; meaning the material has nine independent elastic constants. The elastic constants are E11, E22, E33, G12, G13, G23, ν12, ν13, and ν23. However, unidirectional fiber composites fall into a category known as special orthotropic/transversely isotropic. For this special case, reinforcing fibers run in either the 0° or 90° directions. In this case, there are only five elastic constants. The constants are E11, E22, ν12, ν21, and G12. Therefore, the endeavor of design engineers is to evaluate laminated composites as a stacked sequence of unidirectional laminae. This analysis process, known as classical lamination theory (CLT), is key to understanding the behavior of composite pipes under pressure. This process is detailed in appendix A. This section discusses the loading vector and the elastic analysis for pipes under internal pressure.

4.4.2 Loading Vector

The classical lamination theory (for plane stress) does not account for strains in the Z direction. The theory can be employed to consider radial effects; however, the process is complex. Therefore, the thin-walled pipe assumption of negligible radial stresses is crucial in this elastic analysis. This assumption allows design engineers to make the critical simplification that the wall of a pipe behaves like a laminated plate under plane stress. Therefore, the hoop stress is related to the force resultant in the Y direction and the longitudinal stress is related to the force resultant in the X direction. These force resultants (force per unit width) are not the same as the longitudinal and hoop stresses (force per area) because the force resultants are taken per unit width. That is to say, stresses are integrated over the area so that the units match. Therefore, the thickness (t) of the wall is neglected in the force resultants. The loading vector for composite pipes under pressure only has two non-zero terms (N_x and N_y), given in equations (4-6) and (4-7) [27].

$$N_X = \frac{P * r}{2} \tag{4-6}$$

$$N_y = p * r \tag{4-7}$$

The relationship between in-plane forces (N_x,N_y, N_{yx}) moments (M_x, M_y, M_{yx}), and mid-plane strains (ϵ_x^0 , ϵ_y^0 , ϵ_{xy}^0) mid-plane curvatures (k_x, k_y, k_{xy}) is given by Equation (4-8). This equation is the key equation employed in the determination of strains within a laminate. Stresses and strains in the fiber directions and global can all be determined from this base equation. Thus, this equation is the basis for elastic analysis for stresses and strains in the walls of thin walled pipes. More details for this theory is provided in appendix A.

$$\begin{bmatrix} \epsilon_x^0 \\ \epsilon_y^0 \\ \epsilon_{xy}^0 \\ k_x \\ k_y \\ k_{xy} \end{bmatrix} = \begin{bmatrix} A_{11} & A_{12} & A_{16} & B_{11} & B_{12} & B_{16} \\ A_{12} & A_{22} & A_{26} & B_{12} & B_{22} & B_{26} \\ A_{16} & A_{26} & A_{66} & B_{16} & B_{26} & B_{66} \\ B_{11} & B_{12} & B_{16} & D_{11} & D_{12} & D_{16} \\ B_{12} & B_{22} & B_{26} & D_{12} & D_{22} & D_{26} \\ B_{16} & B_{26} & B_{66} & D_{16} & D_{26} & D_{66} \end{bmatrix}^{-1} * \begin{bmatrix} N_x \\ N_y \\ N_{xy} \\ M_x \\ M_y \\ M_{xy} \end{bmatrix} \tag{4-8}$$

Equation (4-8) only holds true for elastic zone of composite materials. Once failure progression is initiated, non-linear behavior is initiated, the extent of which is based on a number of factors.

4.5 Failure Behavior of Composite Materials

Failure behavior of composites materials is very challenging to predict. The issue arises from the fact that damage onset does not necessarily coincide with final failure. Laminate failure is a result of progressive failure of the fibers, matrix, and laminae. The usual progression initiates with matrix micro-cracking and then moves to matrix cracking, fiber pull-out, layer delamination, and finally fiber breakages. However, failure does not necessarily include all of these various modes. Some of the factors that complicate the analysis are fabric architecture, fiber volume fraction, voids, manufacturing process, material types and properties, and loading type, and non-homogenous stresses within a laminate [28].

There are many equations, criteria, and analysis methods for the prediction of laminate failure. These methods rely on mechanics principles, empirical equations, and experimental data. In the literature, several different methods have been proposed for the failure predictions of composite pipes under internal pressure. Two specific methods were explored in this research. The first is known as the ply-discount failure progression. Researchers have applied this process to predict failure pressures of composites pipes with varying degrees of success. The second method evaluated is known as the strain energy density failure theory. This theory was proposed by Vadlamani and GangaRao. This theory has shown reliability in predicting failure of coupons of varying fabric architecture under tension and bending up to 90 percent of ultimate stress. However, this theory has not yet been evaluated for reliability in predicting burst pressures of GFRP pipes.

4.5.1 General Comments on Failure Progression

Failure prediction methods involve two major processes, in addition to the process of classical lamination theory. The first process employed in failure prediction is the process through which stress distributions, failure modes, and failure strengths are evaluated. This can be done through the study of micromechanics, in which the individual constituents within a lamina are evaluated for stress distribution and failure modes. However, most researchers simplify the analysis by viewing each ply as a homogenous material. Therefore, the details of damage initiation and propagation are captured by the overall failure strengths of the laminae. In this simplified method, failure stresses are then viewed as the ultimate stresses of the individual laminae (Barbero, 1998).

The second process employed in failure progression analysis is a stiffness degradation method. Stiffness degradation refers to process through which the properties of a failed lamina are accounted for in terms of the effect on the other laminae. Therefore, the degradation rules determine the redistribution of stresses in a laminate once a lamina has failed. There are currently two popular degradation methods, the continuum discount method and the ply discount method [34].

4.5.2 Failure Progression through Ply Discount Methods

As has been discussed previously, classical lamination theory is employed to determine stresses and strains within the layers of a laminate within the elastic loading zone. This theory does not apply once failure is initiated. Therefore, the first step in failure prediction to determine the load (internal pressure within pipes) at which the first lamina fails. This point is known as first ply failure (FPF). Since most laminates have complex fabric architectures (usually of unidirectional fabrics oriented at various angles), failure criteria and strength properties of unidirectional laminae are employed in this task [31].

4.5.2.1 Unidirectional Strength Properties

Since the onset and progression of damage for the constituent materials is accounted for in the failure strength of a homogenous (assumed) lamina, failure strengths for various failure modes must be determined for a given lamina. Failure criteria for plane stress conditions require five strength values to be determined. The five values are mentioned below (Kassapoglou, 2010).

1. Longitudinal Tensile Strength (Xt)
2. Transverse Tensile Strength (Yt)
3. Longitudinal Compressive Strength (Xc)
4. Transverse Compressive Strength (Yc)
5. In-Plane Shear Strength(S)

These strength properties are determined through ASTM coupon tests of unidirectional laminates. The primary standards for these tests are D3039, D3410, and D5379. Since empirical relationships are not reliably accurate, these test methods are the most accurate way to determine failure strengths of these unidirectional laminates.

4.5.2.2 Failure Criteria

Many failure criteria for plane stress conditions have been proposed for orthotropic materials. Failure criteria are empirical equations with parameters that are fitted to experimental data. The criteria are applied to determine whether individual laminae have failed. These criteria are used because it is very challenging to produce accurate models for the complex failure modes of micro-cracking, cracking, and delamination. These criteria do not capture the actual failure modes. A few of the most commonly used criteria are mentioned below [28].

1. Maximum Stress Criterion

2. Maximum Strain Criterion
3. Tsai-Hill Criterion
4. Tsai-Wu Criterion

The maximum stress and strain criteria differentiate between fiber failure modes and matrix failure modes. However, neither considers the interaction of the various stress components. The methods evaluate stresses and strains for failure examination one at a time. Since there is no interaction of stress or strain components, the two methods are not conservative if several components of stress are near the failure strengths in those directions.

To account for this issue, quadratic failure criteria were developed. These criteria provide failure envelopes for failure evaluation. The Tsai-Hill and the Tsai-Wu theories fall into this category. A general 2-D representation of the quadratic criterion is provided in Equation (4-9).

$$F_{11} * \sigma_1^2 + F_{22} * \sigma_2^2 + F_{66} * \tau_{12}^2 + F_1 * \sigma_1 + F_2 * \sigma_2 + 2 * F_{12} * \sigma_1 * \sigma_2 \tag{4-9}$$

The Tsai-Hill theory works well for situations where the tensile and compressive strengths are the same, but provides poor results when the values differ from one another. The Tsai-Wu criteria was developed to overcome this insufficiency. Furthermore, the Tsai-Wu failure criteria has been proven to result in relatively accurate burst pressure failure predictions. For these reasons, the Tsai-Wu was the primary failure criteria investigated in this research. The major shortcoming of the Tsai-Hill and Tsai-Wu criteria is that no differentiation of fiber failure and matrix failure is made [28]. It has yet to be seen whether this shortcoming significantly effects burst pressure predictions for composite pipes.

4.5.2.3 Tsai-Wu Failure Criteria

Substitution of specific terms for the Tsai-Wu criteria, the general quadratic criterion becomes Equation (4-10).

$$\left(\frac{1}{X_t * X_C}\right) * \sigma_1^2 + \left(\frac{1}{Y_t * Y_C}\right) * \sigma_2^2 + \frac{1}{S^2} * \tau_{12}^2 + \left(\frac{1}{X_t} - \frac{1}{X_c}\right) * \sigma_1 + \left(\frac{1}{Y_t} - \frac{1}{Y_c}\right) * \sigma_2 + \frac{(\sigma_1 * \sigma_2)}{2 * \sqrt{(X_t * X_C) * (Y_t * Y_C)}} = 1 \tag{4-10}$$

Where:

σ_1=Stress in the fiber direction

σ_2=Stress Transverse to the fiber direction

τ_{12}=In plane shear stress

Therefore, when the left side of the equation is equal to one, the lamina has failed. The positive root of the quadratic equation is known as the strength ratio(R). The strength ratio is a measure of the remaining strength in a lamina under stress; meaning that the strength ratio is similar to a factor of safety. When R=1 the lamina has failed. Therefore, the failure load of a lamina is a product of the applied load and the strength ratio. The quadratic equation with R substituted is given by Equation (4-12) and the strength ratio is given by Equation (4-13) [29].

$$\mathrm{R} = -\left(\frac{\mathrm{b}}{2 * \mathrm{a}}\right) + \sqrt{\left(\frac{\mathrm{b}}{2 * \mathrm{a}}\right)^2 + \left(\frac{1}{\mathrm{a}}\right)} \tag{4-11}$$

$$a * R^2 + b * R - 1 = 0 \tag{4-12}$$

$$R = -\left(\frac{b}{2 * a}\right) + \sqrt{\left(\frac{b}{2 * a}\right)^2 + \left(\frac{1}{a}\right)} \tag{4-13}$$

Where:

a= $\left(\frac{1}{X_t * X_C}\right) * \sigma_1^2 + \left(\frac{1}{Y_t * Y_C}\right) * \sigma_2^2 + \frac{(\sigma_1 * \sigma_2)}{2 * \sqrt{(X_t * X_C) * (Y_t * Y_C)}} + \frac{1}{S^2} * \tau_{12}^2$

b=$\left(\frac{1}{\mathrm{X_t}} - \frac{1}{\mathrm{X_c}}\right) * \sigma_1 + \left(\frac{1}{\mathrm{Y_t}} - \frac{1}{\mathrm{Y_c}}\right) * \sigma_2$

4.5.2.4 Ply Degradation

Once first ply failure has occurred, the stiffness properties of the failed ply must be reduced, and the analysis must be iterated a second time. This must be done because stresses redistribute to other plies, causing further failure. When the strength ratio of the last ply equals one, catastrophic failure of the laminate occurs. The final failure of a pipe under internal pressure occurs at the last ply failure. Thus, the progression of damage is simulated by the progressive reduction of the stiffness of each of the laminae until all the laminae have reached failure stresses [30].

Ply degradation methodology is still an active area of research. Several different authors have proposed methods to reduce specific elements of the transformed stiffness matrices. The challenge is to reduce the stiffness matrices in a way that matches the actual failure mode. Since the Tsai-Wu criteria does not differentiate between failure modes, it is challenging to identify an accurate method of degradation.

4.5.2.5 Failure Progression Steps

In conclusion, failure prediction is an analytical process involving several steps. The process involves several strength properties, empirical equations, and mechanics principles. The process is outlined by the following steps [31].

1. Apply lamination theory to determine strains and stresses within each of the laminae
2. Determine strength properties of unidirectional composite coupons
3. Apply a failure criterion to determine strength factors and the load at first ply failure
4. Apply rules of degradation to failed plies
5. Iterated lamination theory to determine stress redistribution and further ply failure
6. Iterate until last ply failure (burst Pressure prediction) is reached.

4.5.3 Strain Energy Density Failure Theory

It is apparent that failure prediction through lamination theory and failure criteria involves rigorous manufacturing, testing, and computation. Therefore, a second theory, known as the Strain Energy density theory was investigated. This theory was proposed by Vadlamani, Skehar, and GangaRao in 2007 [17]. The theory applies to vinyl ester/glass coupons of varying fiber architectures, loaded under tension or bending. The purpose of this investigation was to determine if the strain energy density failure model could be applied to predict elastic behavior and failure predictions for pipes under internal pressure.

4.5.3.1 *Strain Energy Density Model*

The strain energy density is a common principle discussed in structural mechanics. The strain energy density is defined as the stored energy in a material that has deformed under load. Strain energy density is indicative of material behavior because it is stored energy per unit volume. Thus, strain energy density is not related to specimen dimensions. Strain energy density is taken as the area under the stress strain curve. Therefore, strain energy density can be determined from mechanical testing of coupons, where E, the points of slope change (K_1 and K_2), and the slope ratio can be determined. **Figure 4-3** shows a bi-linear strain energy density diagram (Vadlamani, 2007).

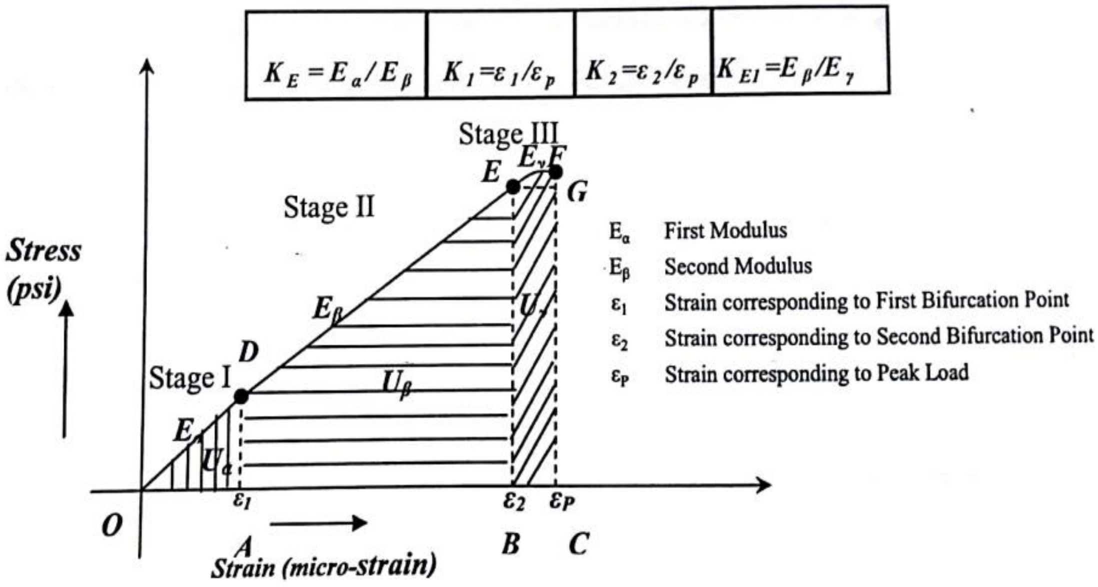

Figure 4-3: *Strain energy density diagram [17]*

Based on the stress/strain curve, the axial for a member under tension strain energy is given by Equation (4-14). However, as can be seen, the model must be slightly altered to account for changes in modulus as load increases. Therefore, the strain energy density of a composite coupon is considered the be the sum of U_α, U_β, U_γ, the three areas shown in **Figure 4-3**.

$$U_T = \frac{P^2 * L}{2 * A * E} \tag{4-14}$$

Where:

P=Applied Load

L=length

A=Area of the specimen

E=Elastic Modulus in the direction of loading.

The research conducted by Vadlamani [17] evaluated five different symmetric laminates (unidirectional, bidirectional, tri-directional with CSM, quadri-directional with CSM, and quadri-directional without CSM), manufactured using compression molding, tested under tension and bending. The results of the study showed the laminates to exhibit bi-linear stress strain response, up to 90 percent of the ultimate stress. The points of slope change (K_1 and K_2) were found to be .34 and .87. The slope ratio (K_{E1}) between the two linear portions of the stress strain curve was found to be 1.2 [17].

Therefore, investigation during this research project sought to determine whether the stress strain curve of a composite pipe, under internal pressure would fit this model. This evaluation was based on the principle that the hoop stress in the wall of the pipe exhibits similar to that of a coupon under tensile loading. This evaluation was done through an evaluation known as split ring testing. The testing methodology, results, and comparisons are presented in the next chapters.

4.6 Elastic Analysis of Kenway Pipes

Once the properties and fiber architectures were determined, the pipes were modelled through the classical lamination theory. The purpose of the analysis was to determine both the modulus of elasticity in the hoop and the longitudinal directions, and to provide the base from which failure progression and failure predictions could be produced.

4.6.1 Elastic Analysis- ⅜ Wall Samples

Based on the known constituents and fiber volume fraction, structural properties of the fibers and resin were determined (commonly available in the literature). The five independent elastic constants for orthotropic material laminae were then determined, as well as the stiffness and transformed stiffness matrices. Finally, the ABD matrix, and stress/strain relationships were established. Units throughout this section are considered in inches, and lbf.

For the analysis, excel files and mat lab programs were used, The excel file was generic, but demonstrated good agreement with the mat lab file, which was built specifically for the 11 layer Kenway pipes (nine FW layers and two CSM layers). The small 0.75 oz/ft^2 mat in the structural layer was neglected. The resin rich zone was modelled as two 0.05-inch thick layers of CSM. The structural layer was modelled at nine 0.039-inch layers of ±57 filament winding. The total laminate thickness of the model was 0.45 inches. Therefore, the layup of the batch one pipes is given by **Figure 4-4**, where layer one is the outer surface and layer 11 is the inner surface of the pipe. The Z values are provided to the left of the figure. It should be noted that the layup is not symmetric, nor does the neutral axis of the laminate run through the center of a ply.

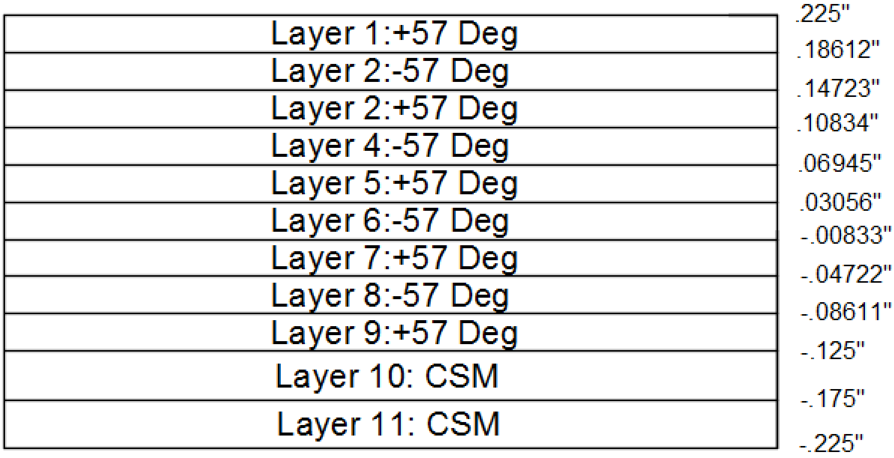

Figure 4-4: *Thin wall pipe layup*

4.6.1.1 Constituent Properties

Table 4-1 and **Table 4-2** provide the structural properties for the constituent materials that were used. These properties vary slightly in the literature. Therefore, there is a possibility that a small degree of error exists between these values on those of the actual materials used. Values were rounded for ease of computation.

Table 4-1: *E-glass structural properties*

E-Glass Property	Calculated Value	Rounded Value
Tensile Modulus	10,500,000 psi	10,500,000 psi
Poisson Ratio	.21	.21
Shear Modulus	4,338,843 psi	4,339,000
FVF	.478	.48
Density	2.5 g/cm^3	2.5 g/cm^3

Table 4-2: *Vinyl Ester structural properties*

Vinyl Ester Property	Calculated Value	Rounded Value
Tensile Modulus	500,000 psi	500,000 psi
Poisson Ratio	.38	.38
Shear Modulus	181,159 psi	181,000 psi
FVF	.525	.52
Density	1.3 g/cm^3	1.3 g/cm^3

4.6.1.2 Lamina Properties

The independent elastic constants for the unidirectional were determined based on Equations (A-1) thru (A-5).

Table 4-3: *Lamina elastic constants*

Unidirectional Lamina Stiffness Terms	Calculated Value	Rounded Value
Longitudinal Modulus(E_{11})	5,280,000 psi	5,280,000 psi
Transverse Modulus(E_{22})	1,567,946 psi	1,568,000
Major Poisson Ratio(ν_{12})	.2987	.30
Minor Poisson Ratio(ν_{21})	.0887	.09
Shear Modulus(G_{12})	451,945 psi	452,000 psi

4.6.1.3 Stiffness Matrices

Based on these elastic constants, the stiffness matrix of the mat, and transformed stiffness matrices of the 57 degree filament winding and -57 degree filament wound layers are provided in

Equations (4-16) and (4-17). These equations provide stiffness properties in terms of the global coordinate system. While unidirectional fibers offer greater longitudinal stiffness than a mat, the mat provides greater stiffness when compared against fiber wound at a cross ply angle. Therefore, CSM plays an important role in laminate strength. Equation (4-15) provides the stiffness matrix of a CSM. These equations are explained more thoroughly in appendix A.

$$Q_{CSM} = \begin{bmatrix} 1/E & -\nu/E & 0 \\ -\nu/E & 1/E & 0 \\ 0 & 0 & 1/G \end{bmatrix} = \begin{bmatrix} 3{,}546{,}486 & 1{,}443{,}004 & 0 \\ 1{,}443{,}004 & 3{,}546{,}486 & 0 \\ 0 & 0 & 2{,}103{,}482 \end{bmatrix} \tag{4-15}$$

$$\overline{Q_{57}} = \begin{bmatrix} \bar{Q}_{11} & \bar{Q}_{12} & \bar{Q}_{16} \\ \bar{Q}_{12} & \bar{Q}_{22} & \bar{Q}_{26} \\ \bar{Q}_{16} & \bar{Q}_{26} & \bar{Q}_{66} \end{bmatrix} = \begin{bmatrix} 1{,}862{,}658 & 1{,}359{,}157 & 480{,}030 \\ 1{,}359{,}157 & 3{,}413{,}973 & 1{,}262{,}125 \\ 480{,}030 & 1{,}262{,}125 & 1{,}343{,}780 \end{bmatrix} \tag{4-16}$$

$$\overline{Q_{-57}} = \begin{bmatrix} \bar{Q}_{11} & \bar{Q}_{12} & \bar{Q}_{16} \\ \bar{Q}_{12} & \bar{Q}_{22} & \bar{Q}_{26} \\ \bar{Q}_{16} & \bar{Q}_{26} & \bar{Q}_{66} \end{bmatrix} = \begin{bmatrix} 1{,}862{,}658 & 1{,}359{,}157 & -480{,}030 \\ 1{,}359{,}157 & 3{,}413{,}973 & -1{,}262{,}125 \\ -480{,}030 & -1{,}262{,}125 & 1{,}343{,}780 \end{bmatrix} \tag{4-17}$$

4.6.1.4 ABD Stiffness Matrix

The ABD global stiffness was then compiled based on the stiffness matrices of the layers (Equations (4-15 to (4-17)) and the laminate layup of **Figure 4-4**. Two different versions of this matrix were produced. One version was produced for a symmetric 9 layer FW laminate. In this laminate the B coupling matrix (lower left and upper right) included only zero terms. The second model produced (Equation (4-18)) includes contribution of mats and lack of symmetry. The B matrix is full of significant, non-zero, terms. As will be discussed in the next chapters, this second model was found to be more accurate.

$$Q_{ABD} = \begin{bmatrix} 1{,}006{,}579 & 620{,}005 & 18{,}664 & -29{,}467 & -1467 & 932 \\ 620{,}005 & 1{,}549{,}539 & 49{,}071 & -1{,}467 & -2{,}319 & 2{,}452 \\ 18{,}664 & 49{,}071 & 680{,}671 & 932 & 2{,}452 & -13{,}295 \\ -29{,}467 & -1467 & 932 & 19{,}442 & 10{,}585 & 613 \\ -1{,}467 & -2{,}319 & 2{,}452 & 10{,}585 & 26{,}342 & 1{,}613 \\ 932 & 2{,}452 & -13{,}295 & 613 & 1{,}613 & 12{,}594 \end{bmatrix} \tag{4-18}$$

4.6.1.5 *Elastic Analysis*

The loading vector is the key in an accurate stress/strain prediction. As was noted early in this chapter, the loading vector contains only two non-zero terms (N_x and N_y) for pressure vessels and pipes under longitudinal and hoop stress. However, it is conceivable that the longitudinal stresses (N_x) may not always be present, or that Nx may be a compression stress. Therefore, models were produced including, and excluding the longitudinal stress resultant. The global stress/strain equations for the three loading conditions are then given by Equations (4-19) to ((4-21). Equation (4-19) considers the effect of longitudinal tensile and hoop tensile stresses and simulates the plane stress effects of a free-end closure testing system (referred to as CLT-PST in figures). Equation (4-20) considers the effects of hoop tensile stress only and simulates the theoretical restrained-end closure (referred to as CLT-NPS). In reality, the restrained-end closure testing system actually exerts hoop tensile stress and longitudinal compression stress. This is simulated by Equation (4-21) (referred to as CLT-PSC in figures and tables).

$$\begin{bmatrix} \epsilon_x^0 \\ \epsilon_y^0 \\ \epsilon_{xy}^0 \\ k_x \\ k_y \\ k_{xy} \end{bmatrix} = \begin{bmatrix} 1{,}006{,}579 & 620{,}005 & 18{,}664 & -29{,}467 & -1467 & 932 \\ 620{,}005 & 1{,}549{,}539 & 49{,}071 & -1{,}467 & -2{,}319 & 2{,}452 \\ 18{,}664 & 49{,}071 & 680{,}671 & 932 & 2{,}452 & -13{,}295 \\ -29{,}467 & -1467 & 932 & 19{,}442 & 10{,}585 & 613 \\ -1{,}467 & -2{,}319 & 2{,}452 & 10{,}585 & 26{,}342 & 1{,}613 \\ 932 & 2{,}452 & -13{,}295 & 613 & 1{,}613 & 12{,}594 \end{bmatrix}^{-1} * \begin{bmatrix} \frac{p*r}{2} \\ p*r \\ 0 \\ 0 \\ 0 \\ 0 \end{bmatrix} \tag{4-19}$$

$$\begin{bmatrix} \epsilon_x^0 \\ \epsilon_y^0 \\ \epsilon_{xy}^0 \\ k_x \\ k_y \\ k_{xy} \end{bmatrix} = \begin{bmatrix} 1{,}006{,}579 & 620{,}005 & 18{,}664 & -29{,}467 & -1467 & 932 \\ 620{,}005 & 1{,}549{,}539 & 49{,}071 & -1{,}467 & -2{,}319 & 2{,}452 \\ 18{,}664 & 49{,}071 & 680{,}671 & 932 & 2{,}452 & -13{,}295 \\ -29{,}467 & -1467 & 932 & 19{,}442 & 10{,}585 & 613 \\ -1{,}467 & -2{,}319 & 2{,}452 & 10{,}585 & 26{,}342 & 1{,}613 \\ 932 & 2{,}452 & -13{,}295 & 613 & 1{,}613 & 12{,}594 \end{bmatrix}^{-1} * \begin{bmatrix} 0 \\ p*r \\ 0 \\ 0 \\ 0 \\ 0 \end{bmatrix} \tag{4-20}$$

$$\begin{bmatrix} \epsilon_x^0 \\ \epsilon_y^0 \\ \epsilon_{xy}^0 \\ k_x \\ k_y \\ k_{xy} \end{bmatrix} = \begin{bmatrix} 1{,}006{,}579 & 620{,}005 & 18{,}664 & -29{,}467 & -1467 & 932 \\ 620{,}005 & 1{,}549{,}539 & 49{,}071 & -1{,}467 & -2{,}319 & 2{,}452 \\ 18{,}664 & 49{,}071 & 680{,}671 & 932 & 2{,}452 & -13{,}295 \\ -29{,}467 & -1467 & 932 & 19{,}442 & 10{,}585 & 613 \\ -1{,}467 & -2{,}319 & 2{,}452 & 10{,}585 & 26{,}342 & 1{,}613 \\ 932 & 2{,}452 & -13{,}295 & 613 & 1{,}613 & 12{,}594 \end{bmatrix}^{-1} * \begin{bmatrix} -t*p \\ p*r \\ 0 \\ 0 \\ 0 \\ 0 \end{bmatrix} \tag{4-21}$$

Since the above equations for stress and strain are valid for a particular pressure p, MatLab was employed to iterate strain analysis for pressures between 0 and 1500 psi. 1500 psi was chosen because this pressure marks the high end of operational pressures for transmission lines. Additionally the stress/strain curves were generated. Based on the predicted curves, moduli of elasticity were determined for both the hoop and longitudinal directions. Additional details are provided in appendix A.

A. Hoop Strain Comparison

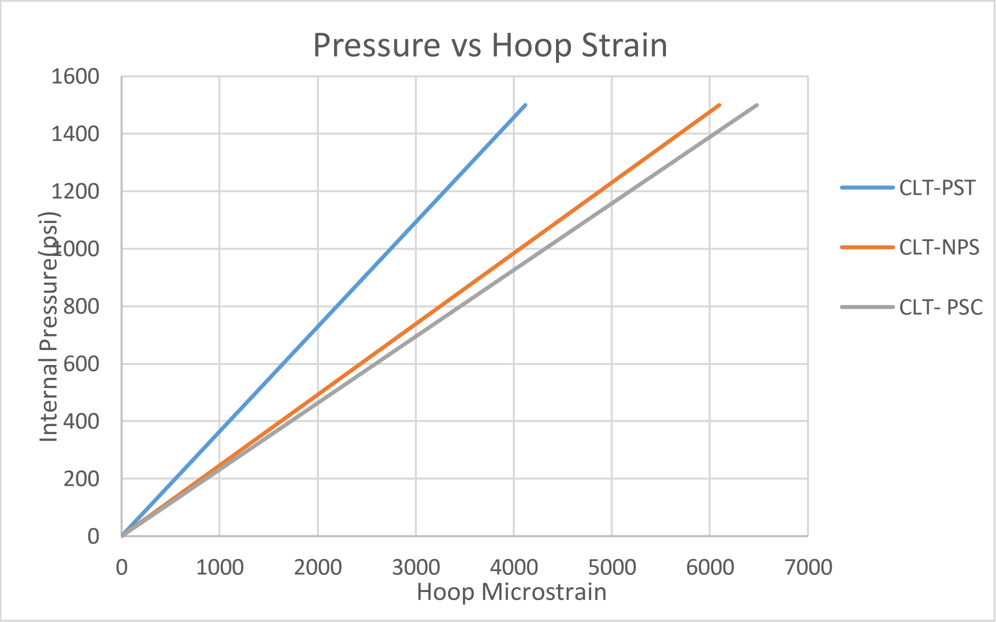

Figure 4-5: *Thin wall CLT hoop strain*

B. Longitudinal Strain Comparison

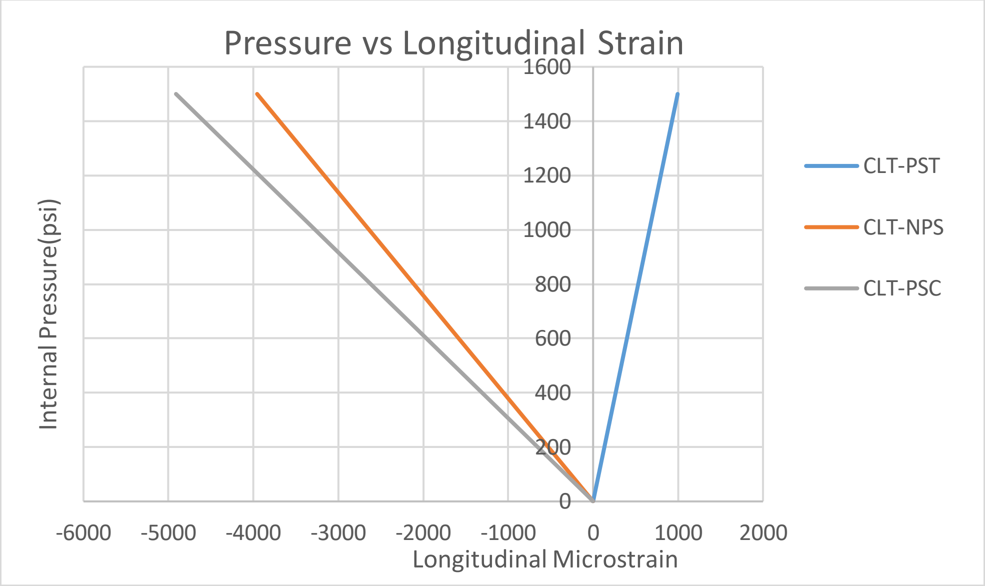

Figure 4-6: Thin wall CLT longitudinal strain

C. Hoop Modulus Comparison

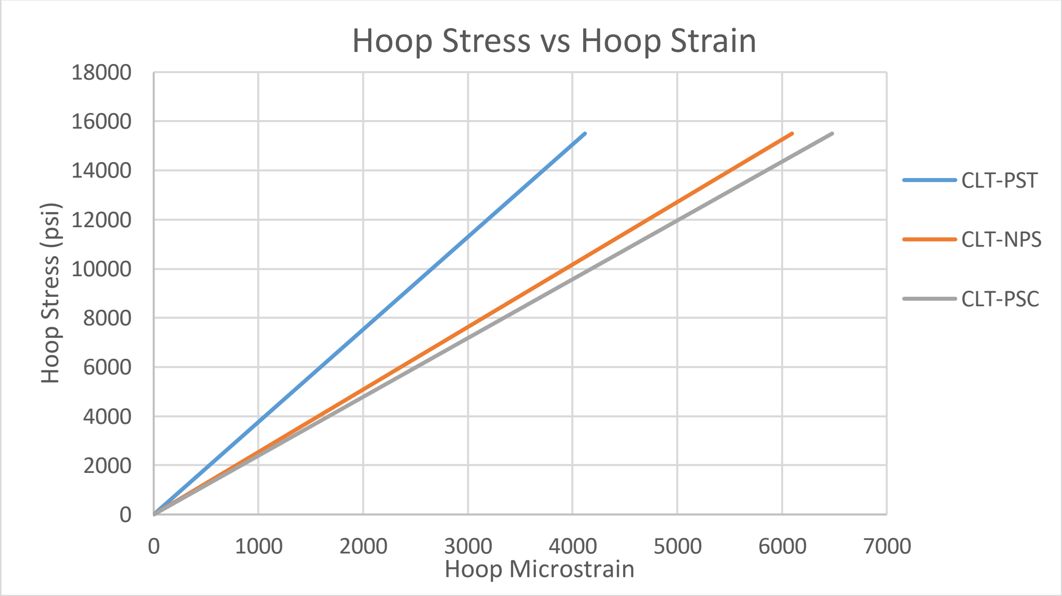

Figure 4-7: Thin wall CLT hoop modulus

4.6.2 Commentary on Elastic Properties

The elastic properties were determined based on the data for predictions above. The hoop modulus of the CLT-PST prediction was found to be 3.76 Msi, the hoop modulus of the CLT-NPS was found to be 2.54 Msi, and the hoop modulus of the CLT-PSC prediction was found to be 2.39 Msi. In reality, the moduli do not change. However, the differing states of stresses produce different strains in the hope directions, giving the appearance of differing hoop modulus. Therefore, the predicted modulus is more of an apparent modulus.

Figure 4-5 to **4-7** to offer comparisons between the different types of loading. CLT-PST models behavior under both hoop and longitudinal tensile stress. This would be the case in situations where resultant forces on the endcaps produce longitudinal stresses in the walls of the pipe. CLT only models the effects of hoop stress. This would be the case in situations where the endcaps do not exert longitudinal stress. CLT-PSC models effects of hoop tension and longitudinal compression.

The three figures demonstrate a key principle for pipes under internal pressure, the effects of fabric architecture and Poison's ratio. In CLT-PST, longitudinal stresses produced axial tension, causing the pipe to elongate and "neck down" in diameter. This means that longitudinal stress counteracts the effect of hoop stress. In CLT-NPS prediction, longitudinal stresses do not exist (i.e. there is no plane stress, abbreviated NPS). Therefore, the effects of hoop stress, the pipe architecture, and Poisson's ratio produce compression strains. As the hoop stress causes the pipe to bulge in dimeter, the length is forced to contract. It can be seen that the two models result in hoop strains differing by nearly 2000 micro strain and the result in longitudinal strains differing by 5,000 psi. In the case of the CLT-PSC, the effects of longitudinal compression stress are observed to increase hoop strains.

4.6.2.1 Observations

- It is critical to model fabric architecture as accurately as possible if meaningful CLT stress strain curves are to be produced. Initially, contribution of chopped strand mat was neglected. However, the contribution of CSM can increase hoop and elastic stiffness. Additionally, small variations in winding angle and fiber volume fraction can affect the results.
- An accurate loading vector is critical. The predicted hoop moduli differ by 37 percent. It was not possible to determine difference in longitudinal moduli since CLT-NPS assumes no longitudinal load exists, except load due to Poisson effect. However, the longitudinal

strain vs pressure results reveal that CLT-PST produces axial tension, while CLT-NPS produces axial compression. Strains predicted by CLT-PSC are even larger in terms of tension and compression. Thus, strains in the fiber directions differ significantly, for the two types of loading.

- Lack of symmetry in the laminate layup results in a non-zero bending matrix(B), but makes little difference in stresses because the curvatures remain small. Therefore, strains within each layer vary little from layer to layer.
- The effect of different loadings ultimately results in differing stresses within the fibers. In situations where both the hoop and longitudinal forces are in tension, fiber stresses are much higher than in situations where longitudinal stresses are in compression and hoop stresses are in tension. Therefore, comparison with experimental results and accurate failure predictions are contingent upon a theoretical loading that matches real world situations.
- Comparisons are based on the CLT-PSC prediction. This is because CLT-PSC most accurately models the loading of the hydrostatic burst pressure test.

4.6.3 Elastic Analysis- ¾ Wall Samples

The elastic analysis of the ¾ wall samples was addressed differently than the first set. Since this set of pipes has an inner diameter of 9.625 inches and a thickness of 0.8 inches (D/t=12.03), this batch falls into the thick-walled pipes category. Therefore, radial stresses cannot be neglected. Furthermore, the magnitudes of the longitudinal and hoop stresses are impacted by the radial stress component. Several equations have been developed to address this behavior in isotropic (Lame’s equations) and orthotropic materials. In the end, the stress resultants differ by around 10 percent. For the sake of simplicity, the thin walled approximation and CLT theory were employed in the analysis.

The major difference between the two batches is the fabric architecture. **Figure 4-8** below shows structural layer 1 (layers 1-9), structural layer 2 (layers 10-18), and the corrosion resistance layers (layers 19 and 20). The z values of each surface in a layer are provided to the left of the figure. The elastic constants for orthotropic materials, stiffness, and transformed stiffness matrices remained the same. Therefore, the major change between the two sets of pipes is addressed in the ABD stiffness matrix.

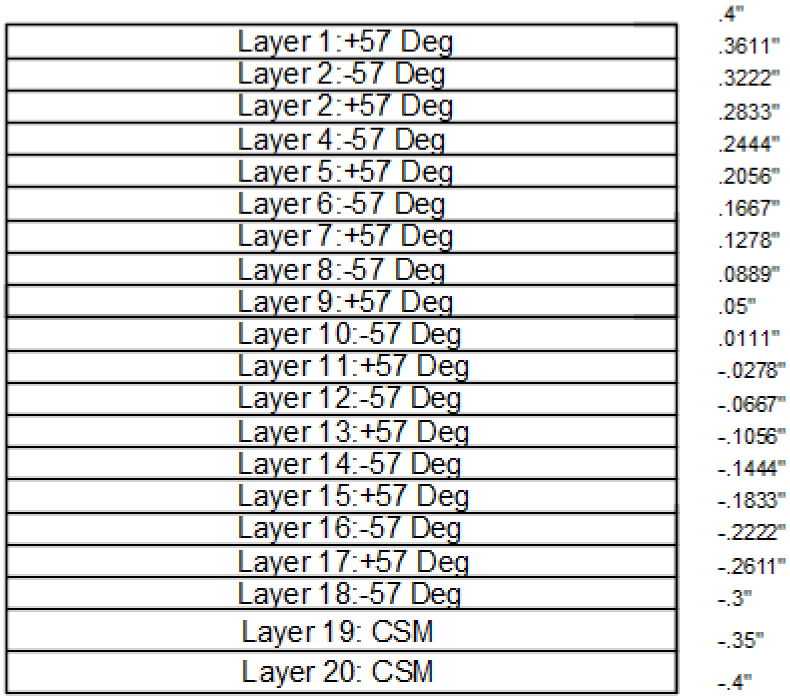

Figure 4-8: *Thick wall pipe layup*

4.6.3.1 Elastic Analysis

As would be expected, the ABD matrix of batch two was found to be much stiffer in terms of load per unit thickness. Loading vectors were kept the same for the CLT-PST, CLT-NPS, and CLT-PSC predictions.

$$\begin{bmatrix} \epsilon_x^0 \\ \epsilon_y^0 \\ \epsilon_{xy}^0 \\ k_x \\ k_y \\ k_{xy} \end{bmatrix} = \begin{bmatrix} 1{,}658{,}509 & 1{,}095{,}711 & -28 & -58{,}934 & -2{,}935 & 6{,}524 \\ 1{,}095{,}711 & 2{,}744{,}430 & -73 & -2{,}935 & -4{,}638 & 17{,}155 \\ -28 & -73 & 1{,}150{,}995 & 6{,}524 & 17{,}155 & -26{,}590 \\ -58{,}934 & -2{,}935 & 6{,}524 & 100{,}241 & 59{,}025 & 651 \\ -2{,}935 & -4{,}638 & 17{,}155 & 59{,}025 & 147{,}297 & 1{,}712 \\ 6{,}524 & 17{,}155 & -26{,}590 & 651 & 1{,}712 & 66{,}704 \end{bmatrix}^{-1} * \begin{bmatrix} \frac{p*r}{2} \\ p*r \\ 0 \\ 0 \\ 0 \\ 0 \end{bmatrix} \tag{4-22}$$

$$\begin{bmatrix} \epsilon_x^0 \\ \epsilon_y^0 \\ \epsilon_{xy}^0 \\ k_x \\ k_y \\ k_{xy} \end{bmatrix} = \begin{bmatrix} 1{,}658{,}509 & 1{,}095{,}711 & -28 & -58{,}934 & -2{,}935 & 6{,}524 \\ 1{,}095{,}711 & 2{,}744{,}430 & -73 & -2{,}935 & -4{,}638 & 17{,}155 \\ -28 & -73 & 1{,}150{,}995 & 6{,}524 & 17{,}155 & -26{,}590 \\ -58{,}934 & -2{,}935 & 6{,}524 & 100{,}241 & 59{,}025 & 651 \\ -2{,}935 & -4{,}638 & 17{,}155 & 59{,}025 & 147{,}297 & 1{,}712 \\ 6{,}524 & 17{,}155 & -26{,}590 & 651 & 1{,}712 & 66{,}704 \end{bmatrix}^{-1} * \begin{bmatrix} 0 \\ p * r \\ 0 \\ 0 \\ 0 \\ 0 \end{bmatrix} \tag{4-23}$$

$$\begin{bmatrix} \epsilon_x^0 \\ \epsilon_y^0 \\ \epsilon_{xy}^0 \\ k_x \\ k_y \\ k_{xy} \end{bmatrix} = \begin{bmatrix} 1{,}658{,}509 & 1{,}095{,}711 & -28 & -58{,}934 & -2{,}935 & 6{,}524 \\ 1{,}095{,}711 & 2{,}744{,}430 & -73 & -2{,}935 & -4{,}638 & 17{,}155 \\ -28 & -73 & 1{,}150{,}995 & 6{,}524 & 17{,}155 & -26{,}590 \\ -58{,}934 & -2{,}935 & 6{,}524 & 100{,}241 & 59{,}025 & 651 \\ -2{,}935 & -4{,}638 & 17{,}155 & 59{,}025 & 147{,}297 & 1{,}712 \\ 6{,}524 & 17{,}155 & -26{,}590 & 651 & 1{,}712 & 66{,}704 \end{bmatrix}^{-1} * \begin{bmatrix} -t * p \\ p * r \\ 0 \\ 0 \\ 0 \\ 0 \end{bmatrix} \tag{4-24}$$

Again, stress/strain analysis was iterated between 1 and 1500 psi. Strain vs Pressure and approximate stress/strain curves very produced.

A. Hoop Strain Comparison

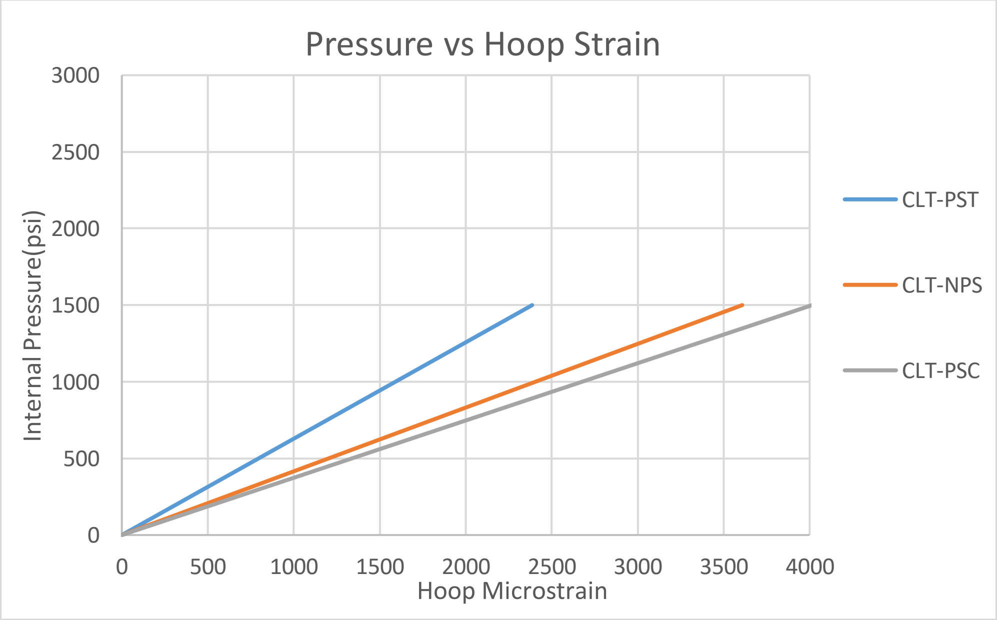

Figure 4-9: *Thick wall CLT hoop strain*

B. Axial Strain Comparison

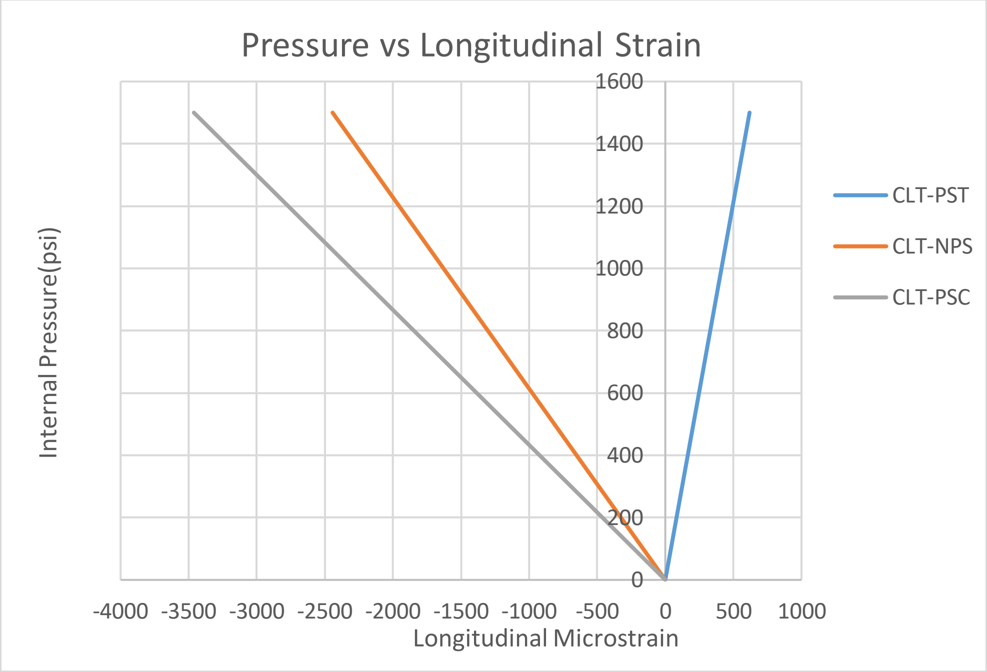

Figure 4-10: Thick wall CLT longitudinal strain

C. Hoop Modulus Comparison

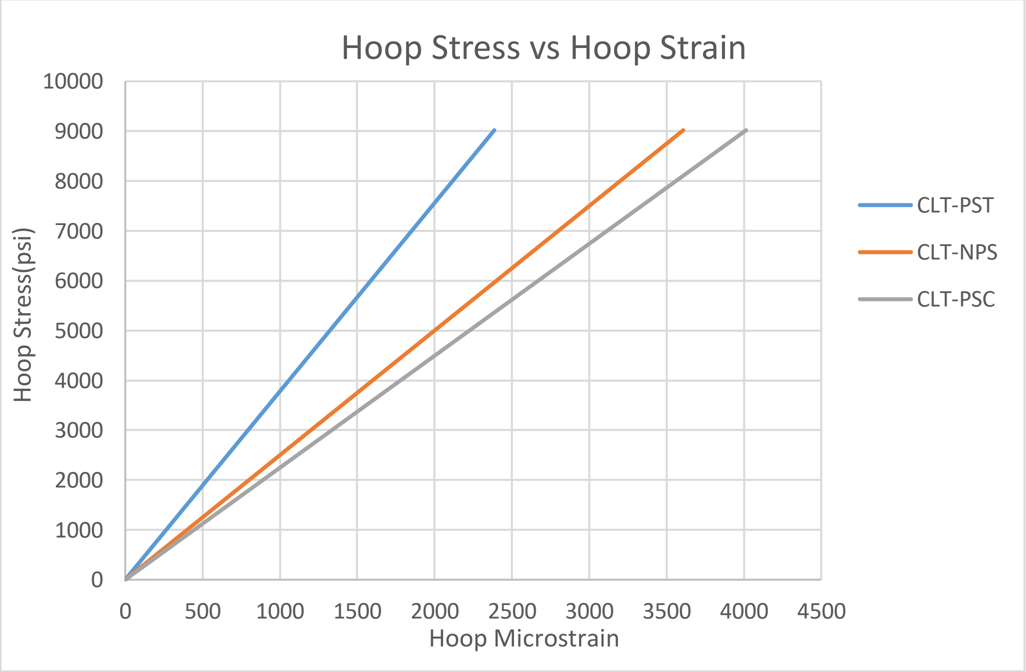

Figure 4-11: Thick wall CLT hoop modulus

4.6.4 Commentary on Elastic Properties

The elastic properties were determined based on the data for **Figure 4-9** to **4-11**. The hoop modulus of the CLT-PST prediction was found to be 3.78 Msi, the hoop modulus of the CLT-NPS was found to be 2.50 Msi, and the hoop modulus of the CLT-PSC prediction was found to be 2.24 Msi. The graphs above and subsequent elastic moduli are only approximate, since the pipes do not truly follow thin-wall mechanics relationship. However, the elastic moduli of the two batches of pipes are very similar. Furthermore, the Poisson effect and loading produce similar differences in mechanical behavior. Therefore, it is crucial to accurately represent the state of plane stresses, or lack thereof.

4.6.4.1 Observations

- Modelling of multilayered laminates is tedious and time consuming. Mistakes are difficult to catch and can significantly alter results
- To a small degree, it is possible to reduce the mathematical computation for a model by reducing the number of layers and increasing layer thickness, so that the laminate thickness remains constant.
- The method of loading alters hoop strain by 40 percent at 1500 psi.
- The method of loading alters approximated hoop moduli by 41 percent
- The two batches provided good agreement on the effect of axial stress on the overall mechanical behavior
- Again, the CLT-PSC prediction is used for comparison with experimental methods.

4.7 Failure Analysis of Kenway Pipes

Failure analysis through classical lamination theory and failure criteria is only possible if an accurate elastic model exists. As will be discussed in the next chapter, this model seems to perform reasonably well for both the thin walled pipes and thick-walled pipes. The challenge arises at the onset of failure in the resin or fibers. The failure initiation and propagation result in lower hoop and longitudinal moduli, and increased strains. In this situation, the ABD stiffness matrix must be adjusted and the analysis rerun. Thus, failure analysis models nonlinear behavior through a series of small linear segments of degreasing stiffness. The result is in an approximated nonlinear curve.

During evaluations, it was not possible to model this failure because accurate unidirectional lamina strength values could not be determined. It was not possible to produce tensile coupons and conduct tests in the available time. Furthermore, it remains to be seen if the filament winding process can produce a unidirectional coupon similar in strength to the pipe specimens. Additionally, mechanics based and empirical equations do not provide accurate predictions of lamina failure strengths. Therefore, failure prediction using the Tsai-Wu failure criteria and ply degradation models remains a topic for future work. However, the methods proposed in Chapters 3 and 4 indicate that such research could yield fruitful results.

4.8 Analytical Prediction vs Hydrostatic Burst Pressure Results

4.8.1 Caveats Regarding Testing and Analysis

Accurate interpretation of results under hydrostatic testing and comparison of data with analytical models depends on a few key facets. Various simplifications of test effects and lack of material knowledge affect the test results and need to be addressed before addressing the analysis.

The hoop stress is typically calculated using thin-walled stress behavior (i.e. $\sigma=Pr/t$) due to the computational simplicity. However, greater accuracy can be obtained by using Lame's equations for hoop stress as these equations incorporate changes in stress through the wall thickness. Since both sets of pipes have an R/t ratio near 10, Lame's equations could be used for both sets of pipes (although the 3/8 pipes are considered thin wall). Using Lame's equations, the hoop stress inside the pipe is greater than the stress outside pipe as shown in , with the difference equal to the internal pressure. For the ⅜ wall pipes, the difference in predicted stresses is around 5%, but the error increases with the ¾ wall pipes by ≈ 8.5%. As the strain gauges were applied to the outer surface, more accurate stress/strain results should be based on Lame's equations, particularly for the ¾ wall pipes. Therefore, the predicted hoop moduli for the pressure tests are not as conservative as possible, but are well within reason. **Table 4-4** provides the comparison of stresses.

***Table 4-4**: Thin wall vs Lame's hoop stresses*

Sample Name	Lame's Outer Hoop Stress (psi)	Lame's Inner Hoop Stress (psi)	Thin Wall Hoop Stress (psi)	Lame’s Outer vs Thin Wall Difference	Lame’s Inner vs Thin Wall Difference
3/4 Sample 1	30362	35534	32759	-7.3%	8.5%
3/4 Sample 2	30802	36049	33234	-7.3%	8.5%
3/4 Sample 3	23623	27647	25488	-7.3%	8.5%
3/8 Sample 1	27573	30352	28899	-4.6%	5.0%
3/8 Sample 2	29156	32125	30571	-4.6%	5.1%
3/8 Sample 3	30569	33711	32067	-4.7%	5.1%

Secondly, the hydrostatic test methodology may have also influenced stress/strain results. A hand pump was used to apply the load so that cracking and/or leaks in the pipe walls could be easily heard, as opposed to using an electrical pump. The pump produced a non-uniform loading rate as the pump handle has to be retracted after each load, although this effect has been averaged out. Furthermore, the pump operated under two modes, high and low. In high mode, pressure was applied rapidly (0 to around 1,000 psi internal pressure in about two minutes). Beyond 1,000 psi the pump would kick over into low mode and the rate of loading was decreased (continued for 9 to 30 minutes). When analyzing the stress-strain curves, this change in load rate produced a change in slope, which is to be avoided when calculating the modulus. To account for the high/low pump speed and to more accurately match the ASME standard, the moduli were calculated only during the initial high load rate, which varied between 20 and 94 seconds. For the ⅜ wall pipes, the moduli were computed when the stress was between 2 and 8 ksi, which corresponds to a stress range of 6% to 28% of ultimate stress. Similarly, the modulus was computed for the ¾ wall pipes when the stress was between 5 and 10 ksi, which corresponds to 15% to 30% of ultimate for the first 2 samples and 20% to 39% for the final sample that had a significantly lower ultimate load attributed to a local flaw.

Thirdly, it is unclear whether data used for the CLT predictions are reliable. The theory is based on constituent properties, fiber volume contents, and fabric architectures. While this data was obtained through available literature and manufacture reports, more accurate information could have been obtained, had in-house manufacturing and materials testing been possible. If the properties of the constituent materials were incorrectly modelled, the method may reflect much more poorly than is true. Although many researchers have verified CLT as an accurate predictor of elastic behavior of composite materials, the model used in this research may require fine-tuning.

Fourthly, the CLT-PSC prediction most certainly does not truly capture the effect of the restrained-end closures. At times during testing, endcaps were flush with the end of the pipe (i.e. no longitudinal compression stress). As the pipes expanded radially, the length contracted and the end of the pipes pulled away from the caps (i.e. longitudinal compression exists due to internal pressure compression stress). Theoretically, the true behavior is somewhere between the two CLT-PSC predictions and the CLT-NPS prediction. Therefore, CLT-NPS assumes only hoop stress and the CLT-PSC assumes hoop tension and longitudinal compression due to end restraints. Again, CLT-PST assumes hoop tension and longitudinal tension, but only applies to systems with free-end closures.

Finally, discussion in this section seeks to isolate analysis of longitudinal and hoop behavior. In reality, the fiber angle and Poisson effect interconnect the two. Therefore, reported moduli should be thought of as “apparent” moduli. The true modulus of the pipes in the principle directions and fiber directions do not change. However, the various loading vectors (CLT-PSC, CLT-NPS, and CLT-PST) have effects on both the longitudinal and hoop strains, meaning that the data in this section creates the appearance of differing moduli. In reality, it is difficult to isolate properties of a material subjected to plane stress.

4.8.2 Elastic Prediction

4.8.2.1 3/8 wall pipes under hydrostatic loads

This section compares stress/strain results of CLT and stress/strain results of the hydrostatic burst pressure test. The results are provided in **Table 4-5**. The hoop moduli were evaluated from 2 to 8 ksi. In this range, the stress/strain curve is almost perfectly linear (R^2=.996 to .999). The average modulus is 3.21 Msi, with a coefficient of variation of 4.8%, indicating rather consistent results. However, errors in the CLT predicted values always lean on the conservative side.

In this case, it appears that the CLT prediction may need to be adjusted. This could be done by more accurately determining structural properties of the materials. Further resin content testing and strength testing could be conducted to more accurately predict properties of a laminae.

Table 4-5: *Thin wall hoop modulus comparison*

Specimen	Average Hoop Modulus (Msi)	CLT –PSC Prediction (Msi)	Percent Error (%)
1	3.36	2.39	28.9
2	3.20	2.39	25.3
3	3.06	2.39	21.9

Table 4-5 shows the stress/strain response (up to failure) of the burst-pressure specimens, compared with the stress/strain prediction of the CLT-PSC (up to 1500 psi, 50 percent of burst pressure). This prediction is for a restrained-end test frame (i.e. longitudinal compression stress equal to internal pressure). Therefore, the restrained-end system was assumed to produce hoop stress and longitudinal compression stress.

The **Figure 4-12** shows good agreement between the prediction and the experimental results up to a hoop stress of 8,500 to 10,000 psi (1,000-psi, internal pressure). Around this point, failure initiation is suspected. The hoop modulus of the pipe is reduced (due to suspected damage progression), and the CLT prediction ceases to be conservative. Beyond this range, the average hoop modulus (30 percent to 90 percent ultimate stress) is 1.62 Msi (R^2= .992). The CLT prediction was produced for stresses up to 50 percent of ultimate stress. This was done so that the non-conservative prediction (beyond 30 percent ultimate stress) could be observed. The data seems to show good agreement with the prediction at a hoop stress of 15,000 psi; however, this is misleading. In reality, the hoop modulus of the pipe has been degraded (E=1.62 Msi). Therefore, the CLT-PSC prediction is only considered valid up around 1,000 psi internal pressure, around 30 percent of the ultimate pressure. However, the pipes are expected to only be exposed to pressures 1/5th of burst pressure, thus the CLT prediction matches well with expected operating conditions. However, this observation should be considered lightly, as the slope change may also have been influenced by the load rate. While there does appear to be a small change in slope around 8,500 to 10,000 psi, the change in slope may have been caused by the test method. Around the same stress, the hydraulic would kick over in high mode and the load rate would change. Therefore, the change in slope is believed to be a result of failure initiation, as well as the change in pump mode.

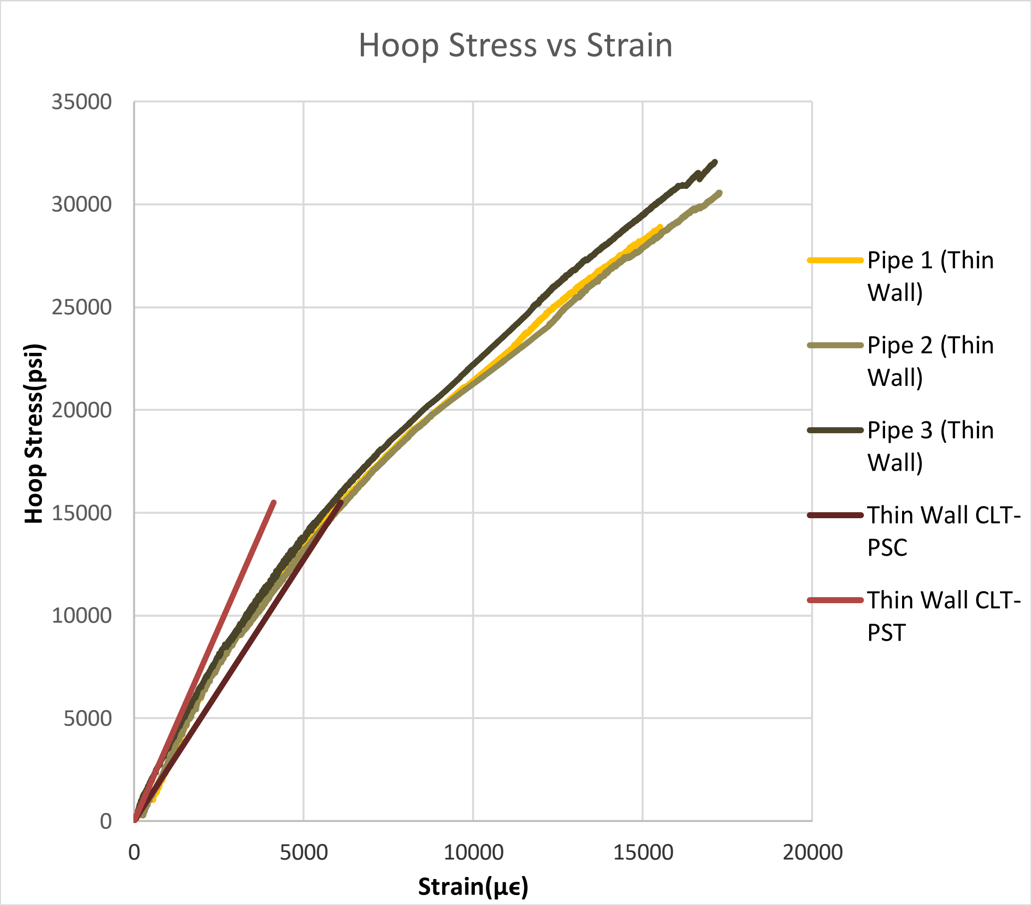

Figure 4-12: *Thin walled stress/strain comparison*

In addition, to the restrained-end prediction (Thin Wall CLT-PSC), a free-end prediction (Thin wall CLT-PST) was also provided. This prediction considers the effects of longitudinal tensile stress (due to attached endcaps) and hoop stress. Although unverified experimentally, this prediction is thought to be a good indication of pipe behavior in service (longitudinal tension and hoop tension). It can clearly be seen that the hoop modulus is higher for free-end systems. This additional stiffness is due to the effects of fabric architecture and Poisson’s ratio. That is to say, the longitudinal tensile stress imposed by attached endcaps counteracts the hoop strain. In short, longitudinal stress causes the pipe to elongate axially and contract circumferentially. Conversely, hoop tensile stress causes circumferential elongation and axial contraction. However, it should not be assumed that fiber stresses are lower. While the longitudinal stresses limit the hoop strains, the longitudinal stresses also add tensile stress to the fibers. Therefore, a free- end test frame will yield a higher hoop modulus and a lower burst pressure. The above scenario may have to be revised when resin and shear stresses control; such as in situations where the ID/thickness ratio is smaller (i.e. thick walled pipes).

Comparison between predicted longitudinal moduli from the pressure test and CLT-PSC prediction was not conducted as easily because it was difficult to accurately determine longitudinal stresses. Therefore, pressure/strain relationships were compared. Strains of the pressure test and CLT-PSC were compared at 1,000 psi. As is seen in **Table 4-6**, the hoop and longitudinal prediction are both very conservative. Errors seems to vary (17-36 percent) for the hoop and longitudinal predictions, suggesting that error may exist in the accuracy of the chosen material properties, fiber volume fractions, approximated fiber angles, and architectures, or in the measured longitudinal strain. Furthermore, error may have been introduced by manufacturing variances such as percent cure, percent void, and fiber tension during wrapping.

Table 4-6: *Thin wall longitudinal strain comparison*

Specimen	Longitudinal strain @ 1,000 psi (μϵ)	Longitudinal Strain CLT-PSC Prediction(μϵ)	Percent Error %
1	-2,385	-3276	27.19
2	-2,096	-3276	36.0
3	-2,710	-3276	17.3

4.8.2.2 3/4 wall Pipes under Hydrostatic Load

This section compares stress/strain results of CLT and stress/strain results of the hydrostatic burst pressure test, for the ¾ wall pipes (**Table 4-7**). The hoop moduli were evaluated from 5 to 10 ksi hoop stress, equal to 15-30% of ultimate stress for the first 2 samples. This range of the stress/strain curve is fairly linear (R=.995 to .999). The third sample failed at a lower ultimate stress, likely due to a flaw, but the same stress range was used. The flaw is evidenced by the fact that the stress/strain curves of samples 1 and 3 match perfectly. The only difference in the two is that sample 3 failed at a much lower pressure and that specimen 3 displayed little interior or external damage. The primary influence on accuracy of results is from the assumptions based on the thin-walled analysis/theory. The stress equations used in the experiment are only estimates (in the case of thick wall specimens) and differ from actual stresses by as much as 8.5 % (**Table 4-4**).

Errors between 24 percent and 47 percent were observed between hoop modulus for the pressure test using thin walled equations and the CLT-PSC prediction. However, for samples 1 and 3 using Lame's outer surface stress, the modulus differs by 2 and 9% respectively. This suggests that thick-walled equations should be used for these samples as they produce more accurate results. From both stress calculations (thin and thick wall), Sample 2 had a significantly higher modulus values than any other sample tested. Computing the hoop strains for each of the two gages also results in moduli that are significantly higher than the other samples, so gage error is ruled out. It is not clear why the modulus is so much greater for this sample.

Table 4-7: *Thick-walled hoop modulus comparison*

Specimen	Average Hoop Modulus (Msi)	CLT-PSC Prediction (Msi)	Percent Error (%)	Lame's Outer Surface Hoop Modulus (Msi)	CLT-PSC Prediction (Msi)	Percent Error (%)
1	3.07	2.25	26.7	2.30	2.25	2.2
2	4.26	2.25	47.2	3.74	2.25	39.8
3	2.96	2.25	24.0	2.49	2.25	9.6

Figure 4-13 shows the thin-wall stress/strain response (up to failure) of the burst-pressure specimens, compared with the stress/strain prediction of the CLT-PSC (up to 2500 psi, 50 percent of burst pressure). This prediction is for a restrained-end test frame (i.e. longitudinal compression stress p).The figure shows decent agreement(17 percent error in strains) between the CLT-PSC prediction and the experimental results up to between 8,500 and 10,000 psi hoop stress (1,665-psi, internal pressure). Again, the slope in this range appears to change, although it is hard to discern the precise location. Around this point (8,000 to 10,000 psi hoop stress), failure begins to initiate. The hoop modulus of the pipe is reduced (due to damage progression), and the CLT-PSC prediction becomes less conservative. Beyond this range, the hoop modulus (30 to 90 percent ultimate stress) is 1.56 Msi (R=.987).

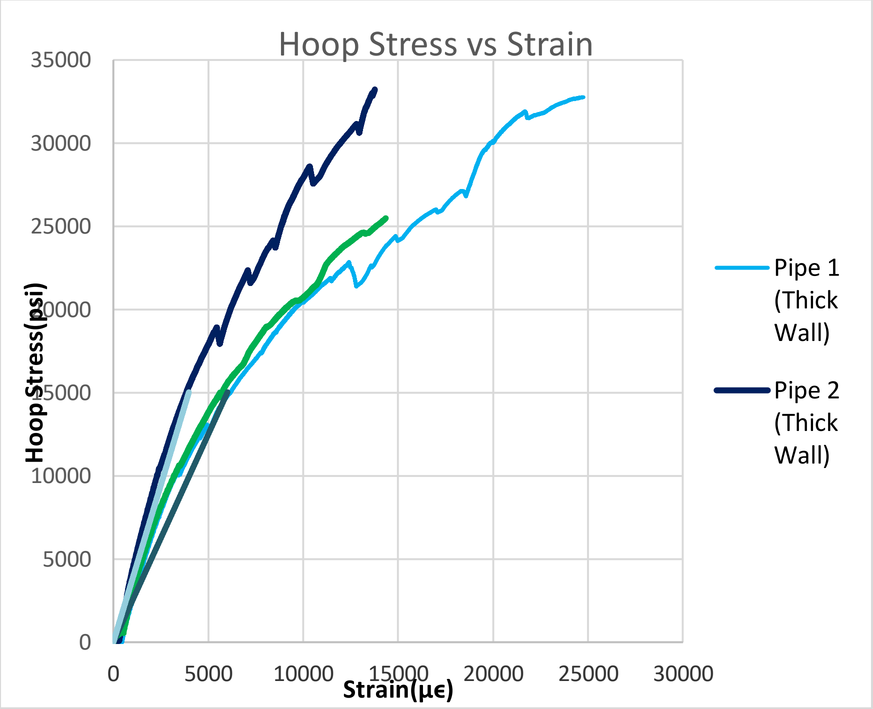

Figure 4-13: *Thick wall stress/strain comparison*

Again, a free-end prediction for plane stress was provided (CLT-PST), in addition to the restrained-end prediction (CLT-PSC). This free-end prediction considers effects of longitudinal tensile stress and hoop tensile stress. As with the thin-walled pipes, the free-end hoop modulus is higher than the restrained-end hoop modulus. Again, the CLT-PST model has been provided as a hypothesis of hoop stress/strain response of a pipe under longitudinal tension and hoop tension (i.e., this models the behavior of a pipe in service). This hypothesis should be tested in future research, through the development of a free-end test fixture.

Evaluating the pressure/longitudinal strain relationship, the analysis looks very different. In this case, specimen 1 appears to be the outlier. The prediction differs from the test data by at least 2 percent and as much as 30 percent. The 30 percent error is likely due to the model, since errors are about the same for the other hoop and longitudinal data. However, the incredible accuracy of the prediction for sample 1 is hard to explain. It is possible that pre-compression longitudinal stress (stress due to actuator load, discussed in section 3.2) may have played a factor, but this is hard to quantify and is unlikely. The hoop strain to longitudinal strain data ratio indicated that effects of pre-compression are not significant at the 1,665-psi pressure. The longitudinal strain comparison (taken at 1,665-psi internal pressure) are presented in **Table 4-8**.

***Table 4-8:** Thick wall longitudinal strain comparison*

Specimen	Longitudinal strain @ 1,665 psi (με)	Longitudinal Strain CLT-PSC Prediction(με)	Percent Error %
1	-3778	-3,842	1.7
2	-2716	-3,842	29.3
3	-3001	-3,842	21.9

As a general observation, the ¾ wall specimens do not offer consistent results (errors between 2 and 20 percent). Specimens 1 and 2 are very similar in burst pressure, but differ in hoop stress/strain response and pressure/ longitudinal strain response. Specimens 1 and 3 are very similar in hoop stress/strain response, but differ in pressure/longitudinal strain response and burst pressure. Further testing is needed to determine the reliability of these results.

4.8.3 Failure Prediction

A proposed progressive failure analysis has been proposed in earlier in this chapter. Due to lack of unidirectional lamina strength properties, this evaluation has not yet been conducted for any of the pipes. While many other researchers have performed these sort of analyses with good success, the accuracy of this method has not yet been verified for the filament wound pipes evaluated during this project. Therefore, classical lamination theory was used only to predict elastic behavior (0 to 30 percent of failure stress).

4.9 Conclusions

This chapter has discussed the methods through which steel and composite pipes can be evaluated. These models are used to predict stresses, strains, and failure pressures for pipes under internal pressure. The purpose in discussing these models was to provide a framework through which pipe properties can be determined outside of the laboratory. This chapter has discussed the specific analysis of filament wound glass/vinyl ester pipes under internal pressure. These pipes were tested in the lab under internal pressure, and were evaluated through the theories presented in this chapter.

5 GPR DETECTION OF BURIED PIPES

5.1 Introduction

Detection of buried non-metallic pipelines by conventional methods that are used in locating metallic pipes and other utilities is a major challenge. While Fiber Reinforced Polymer (FRP) materials such as GFRP have great mechanical properties that make them suitable for oil and gas applications, the inability to locate these materials when buried can limit their adoption in construction of high pressure pipelines. In a previous study [35], the detectability of buried 12", 6", and 3" diameter PVC, GFRP, and CFRP pipes with different external surface finishes and buried at different depths (up to 4 ft. of soil cover) was investigated using Ground Penetrating Radar (GPR). This chapter continues the work done in the previous study, which is focused on making buried non-metallic pipelines detectable using GPR. Findings of the previous study have been reported to PHMSA in a 2017 report entitled, *Advancement in the Area of Intrinsically Locatable Plastic Materials”* [35].

In the current study, six pipe sections were evaluated - four GFRP pipes, one PVC, and one steel pipe which served as a control. These pipes were buried with 2 ft. of soil overlay and tested using GPR.

5.2 GPR Equipment

The GPR system used in this study was the SIR-20 model manufactured by Geophysical Survey Systems, Inc (GSSI). A 200 MHz antenna with a specified penetration depth of up to 30 ft. (in dry sand) and a 400 MHz antenna with a specified penetration depth of up to 12 ft. (in dry sand) were evaluated with this system. The quoted penetration depths depend on the complex dielectric permittivity of the soil medium, and therefore can be significantly lower in soils with high moisture and high clay contents. The GPR system and antennae used in this study are shown in Figure 5-1. The 200 MHz antenna has dimensions of 24"L x 24"W x 12"D and weighs 45 lb. The 400 MHz antenna is smaller with dimensions of 12"L x 12"W x 6.5"D and weighs 11 lb.

The GPR system has survey wheels with optical encoder for tracking horizontal distance along the ground surface. A survey wheel attached to the GPR cart is used to track horizontal distance when the 400 MHz antenna is used, while the 200 MHz antenna has a survey wheel attached to the antenna for horizontal distance measurement as shown in Figure 5-2.

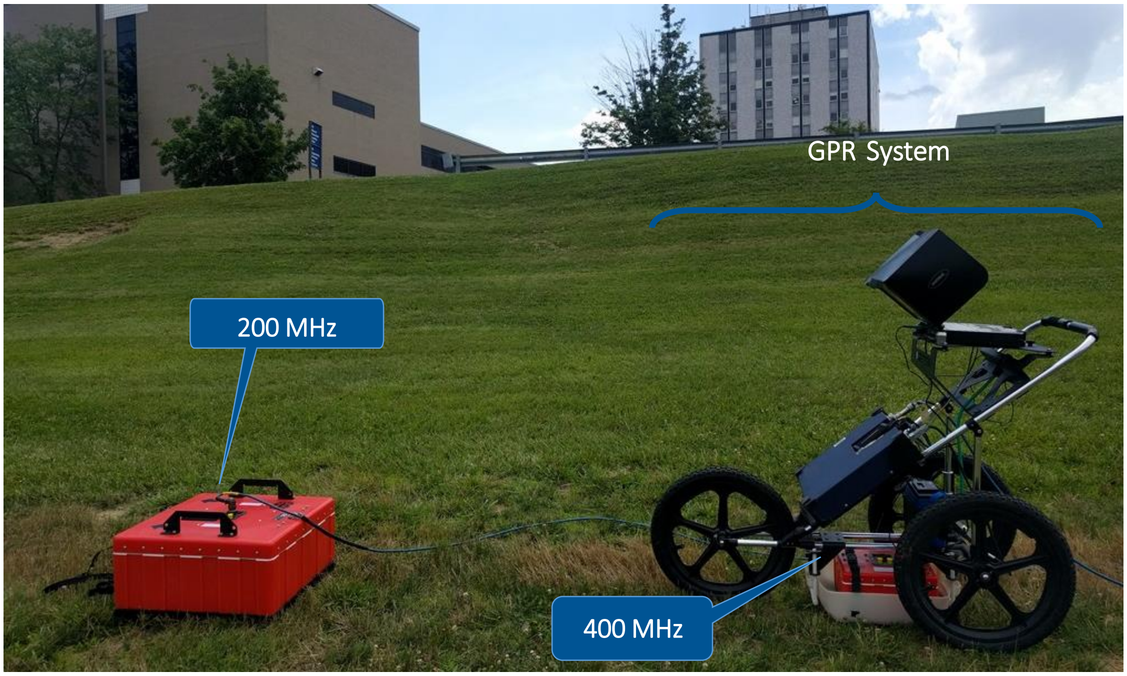

Figure 5-1: *SIR-20 GPR system and antennae used for testing*

Figure 5-2: *200 MHz GPR antenna with survey wheel*

5.3 Sample Preparation and Test Setup

This research involved investigating the detectability of buried 12" diameter GFRP and PVC pipes with different external surface finishes, as well as 10" diameter GFRP and 12" diameter steel pipe control specimen using GPR. All the pipe specimens were 5 ft. long, and capped at both ends to prevent ground water from filling them after burying since the objective was to establish the pipe detectability without the help of GPR reflections from any water inside the pipes.

5.3.1 Material Properties

The 12" diameter GFRP pipes used in this study were supplied by the manufacturer in 5 ft. long segments, while the 10" diameter GFRP pipe was supplied in 4 ft. long segments. The 10" diameter GFRP pipe was one of the pipes being used for high pressure testing as discussed in Chapters 2 and 4. Details of the GFRP pipe are shown in Table 5-1. The 12" diameter PVC pipe for testing was obtained by cutting 5 ft. long segment from a 14 ft. long SDR-35 pipe. Finally, the 12" diameter steel pipe was formed by rolling a carbon steel plate with a wall thickness of 1/8".

Table 5-1: *Material and section properties of CFRP and GFRP pipes/fabrics used*

Pipe Section	Wall Thickness (in)	Fiber Material	Fiber Mat	Fiber Weight (oz. /sq. yd.)	Matrix Material
12" GFRP	3/8	E-Glass	$45^{o}/90^{o}/-45^{o}$	-	Polyurethane
10" GFRP	3/8	E-Glass	Filament wound	-	Vinyl Ester
CFRP Strip	*	Carbon	$0^{o}/90^{o}/\pm 45^{o}$	28	Vinyl Ester

* One layer of fabric was used.

5.3.2 Using carbon fabric, nanoparticle, and aluminum foil to make non-metallic pipes detectable

Non-metallic pipe materials (such as PVC and GFRP) buried underground are generally not detectable using GPR in most soil conditions. This is because PVC and GFRP pipe materials have similar dielectric constant as most soils. In order to make these pipe materials detectable after burying using GPR, we have to create a contrast between the dielectric constants of the pipes and the surrounding soil. Three different approaches were adopted to create dielectric contrast between the pipe materials and the sounding soil - using CFRP strips, using aluminum strips, and using carbon nanoparticle overlay.

Carbon fiber and aluminum tape, like steel, are electrical conductors and as such do not allow transmission of radio waves like GPR signal through them. GPR signal incident on carbon fiber/aluminum material is reflected back to a receiver (unlike the surrounding soil, which absorbs and/or allows the signal to travel through), thereby making the material detectable underground. Carbon nanoparticles are also electrical conductors, hence interconnection between the particles in an overlay is expected to perform like a continuous conductor and therefore make the underlying pipe detectable.

One of the 12" diameter GFRP pipes was wrapped with carbon fabric strip, one was coated with carbon nanoparticles mixed with vinyl ester resin, and the last one was not wrapped and used as a control specimen. Properties of the carbon fabric strip are shown in Table 5-1. The 12" diameter PVC pipe was wrapped with aluminum foil strip, while the 10" diameter GFRP and 12" diameter steel pipes were not wrapped and used as controls. The carbon fabric and aluminum strips covered top half of the pipe circumference and stretched the full length of the pipes (excluding the pipe caps). The carbon nanoparticles overlay also covered a third of the pipe circumference and stretched the full length of the pipe (excluding the pipe caps). A total of six 5 ft. long pipe samples were tested in this study. Some of the pipe samples are shown in Figure 5-3.

(a) (b) (c) (d)

Figure 5-3: *Pipe configurations: (a) 12" diameter GFRP with carbon fabric strip, (b) 12" diameter GFRP with carbon nanoparticle overlay, (c) 12" diameter PVC with aluminum strip, and (d) 12" diameter steel control*

While the pipe caps shown in Figure 5-3 (with CFRP or Aluminum strips, or steel pipe) had metal straps around them, non-metallic straps were used for the pipe caps in case of the GFRP control pipes (12" and 10" diameter) just to ensure that these control pipes did not have any metallic content. It should be noted that the metal straps have very small width (~ 0.5") and are not expected to interfere with GPR signals at 2 ft of burial depth.

5.4 Test Setup and Pipe Burying

The pipe samples were buried in a 36 ft. long trench with 1 ft. spacing between each subsequent pipe (and 2 ft. spacing between the two middle pipes), with 2 ft. of soil cover over the pipes as shown in Figures 5-4 and 5-5(a). The layout of the pipes, including the pipe material, diameter, pipe surface configuration and depth of burial are shown in Figure 5-4.

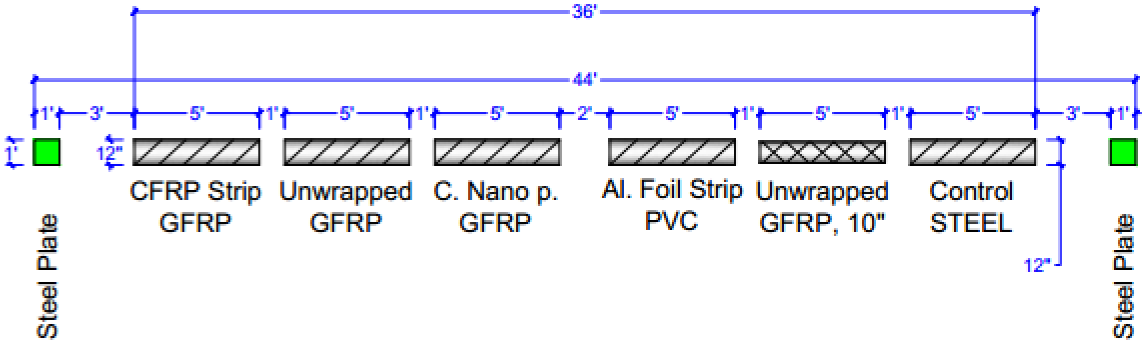

🟩 Steel plates buried at a depth of 3"

▨ 12" diameter pipes buried at a depth of 24" (Total trench depth of 36")

☒ 10" diameter pipes buried at a depth of 24" (Total trench depth of 34")

***Figure 5-4:** Pipe layout for GPR testing*

Additionally, five GS3 soil sensors manufactured by Decagon Devices (Figure 5-5b) were buried at the site at different depths to measure soil properties throughout the testing period. Two of the sensors were buried at 4 ft. depth, two were buried at 2 ft. depth and one was used to measure soil properties at various locations on the ground surface. These sensors enabled quantitative determination of volumetric water content, electrical conductivity, temperature, and dielectric constant of the soil during the testing period. Figure 5-6 shows the pipes being buried. The trenches were backfilled and compacted, the ground surface was levelled and then seeded with grass after pipe burying to restore the initial field condition before GPR testing.

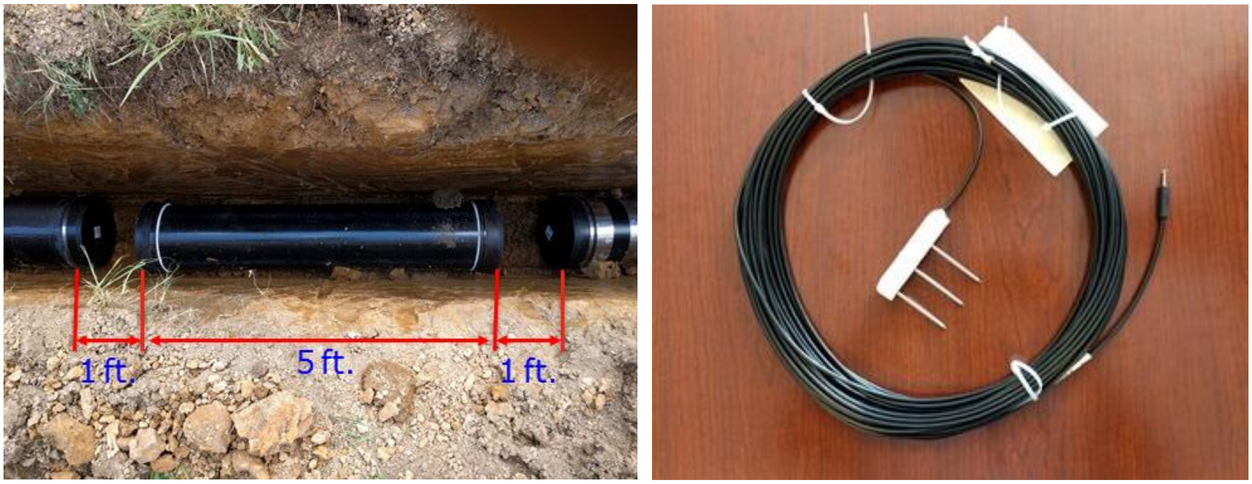

(a) *(b)*

Figure 5-5: *(a) Arrangement of pipes in the trench, (b) soil moisture and resistivity sensor*

Figure 5-6: *The pipe specimens being buried*

5.5 GPR Test Results

GPR tesing of the burried pipe samples commenced after the grass over the trench had grown to its original condition. GPR tests were conducted under different soil moisture conditions (indicated by the changing soil dielectric constant for each test), using both the 200 MHz and 400 MHz frequency antennae. Scans were carried out in both the longitudinal direction along the trench, and transverse direction across the trench/each pipe. The results of these tests are presented in this section. Some of the scan data from a relatively dry soil in the summer months, with average volumetric water content up to 2 ft. depth of 0.290 m^3/m^3 (Dataset I), and relatively wet soil in the winter months, with average volumetric water content up to 2 ft. depth of 0.473 m^3/m^3 (Dataset II) are presented in Figures 5-7 through 5-26. Soil properties for the dataset are given in Table 5-2.

Table 5-2: *Average soil dielectric properties during data collection*

Soil Property	Dataset I	Dataset II
Volumetric Water Content, θ (m^3/m^3)	0.290	0.473
Dielectric Constant, ε	13.42	26.77

As shown in Figure 5-7(a) for Dataset I, all the pipes (with 2 ft. of soil cover) are detectable with varying levels of clarity when scanned with the 200 MHz radar antenna. Particularly, the GFRP pipe with CFRP strip at the top and the PVC pipe with aluminum foil strip at the top are prominently visible. Returned signal from the 12 inch diameter GFRP pipe with no external wrap is also very good, however, reflection from top of the pipe is very short (only signal reflection from the bottom of the pipe is continuous through the length of the pipe).

The GFRP pipe with carbon nanoparticle overlay produced a good but very short reflection from the top of the pipe. The 10 inch diameter GFRP and the steel produced weak reflections, with the steel pipe being a bit more visible in the GPR B-Scan shown in Figure 5-7(a). Figure 5-7(b) shows the GPR data in Figure 5-7(a) processed using ‘Peak Extraction’ technique, which makes it easier to see the buried pipes. Figures 5-8 through 5-13 show details of each pipe, including the B-Scan to the left and A-Scan to the right of each figure. The depth of soil cover over the pipes was also accurately estimated from the GPR data as shown in Figures 5-8 and 5-9, where the measured depth of 24.60" and 25.00" corresponds well with the actual depth of 2 ft. On some of the pipes, reflections from the bottom of the pipes make it possible to estimate the diameter of the pipe as shown in Figures 5-8 and 5-9. However, since the diameter of the pipe is estimated from the electromagnetic wave velocity, which is based on the average soil dielectric constant, there is the possibility for the estimated diameter to be significantly less than the actual diameter. This is because, the dielectric constant of the overlying soil medium is significantly more than the dielectric constant of air in the pipe. The above statements apply even more to Dataset II (presented later) where the dielectric constant of the soil is much higher than that of air (26.77 for the soil and 1 for air). In addition, the pulse width of the radar signal for this test is larger than the actual pipe

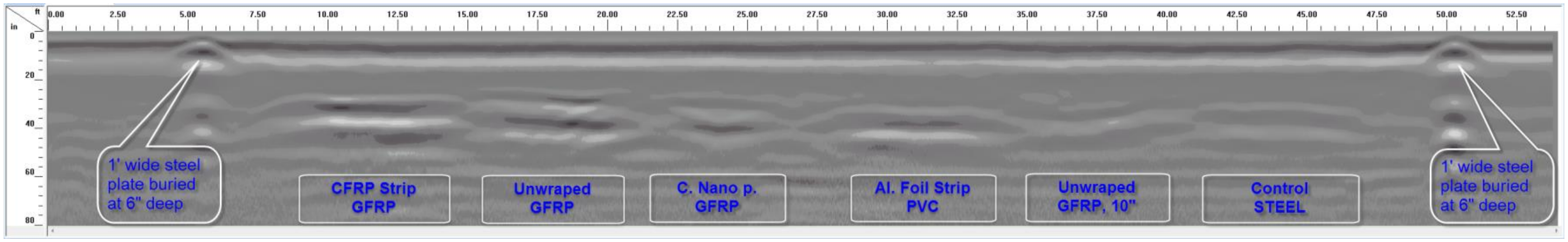

(a) Longitudinal scan along the full length of the pipe trench using 200 MHz GPR antenna

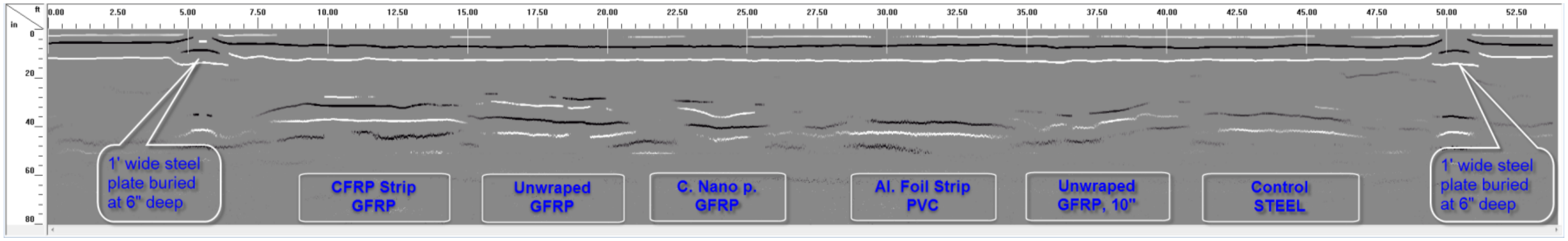

(b) Peak extraction processing used to make buried pipes in scan (a) more visible

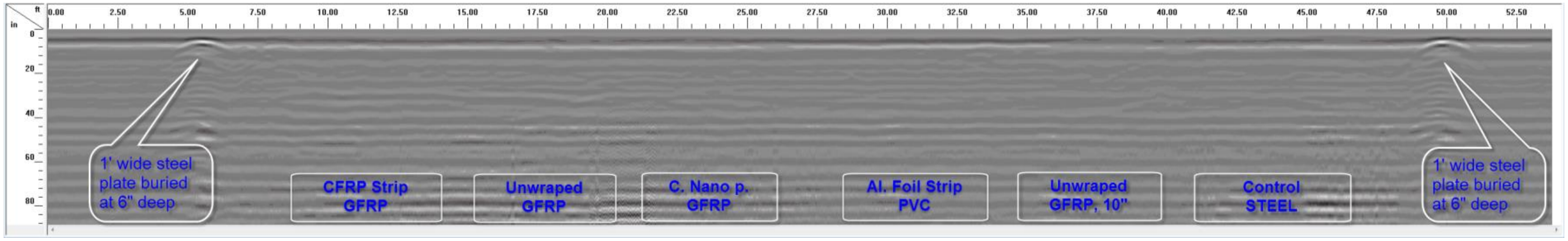

(c) Longitudinal scan along the full length of the pipe trench using 400 MHz GPR antenna

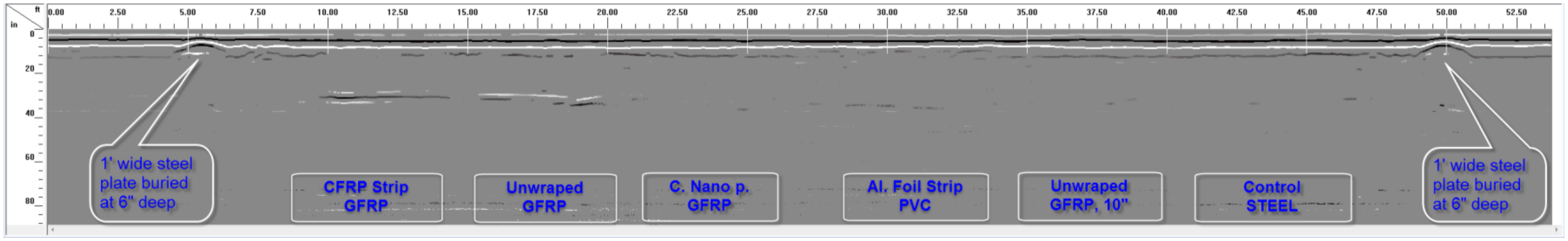

(d) Peak extraction processing used to make buried pipes in scan (c) visible

Figure 5-7: *Longitudinal scans over the pipe trench for Dataset I*

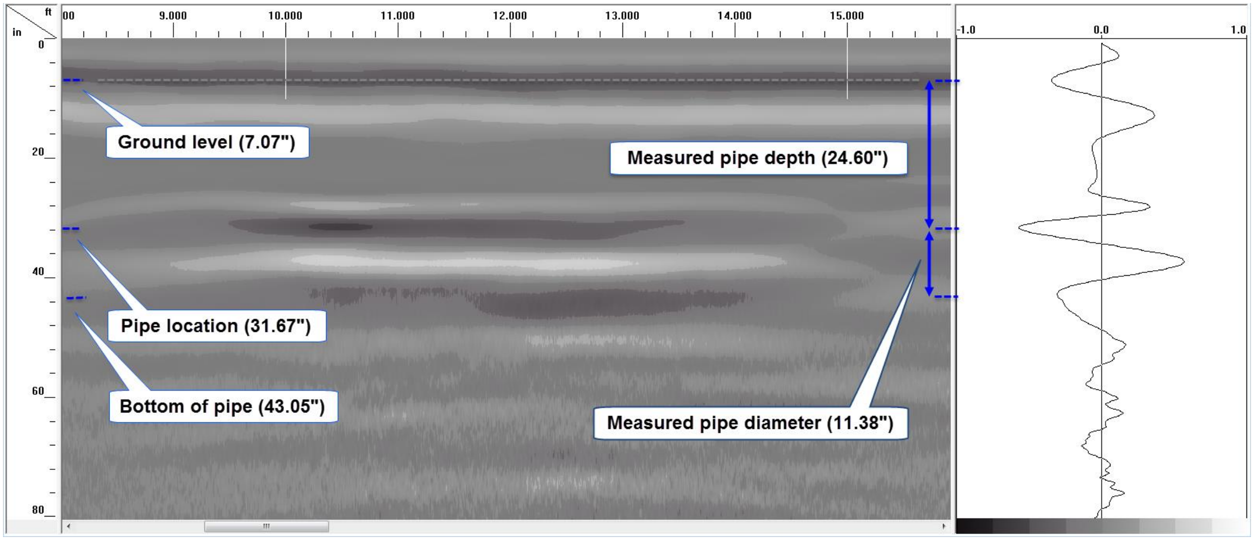

Figure 5-8: *Longitudinal GPR scan (left) and A-Scan (right) over 12" CFRP Strip GFRP pipe*

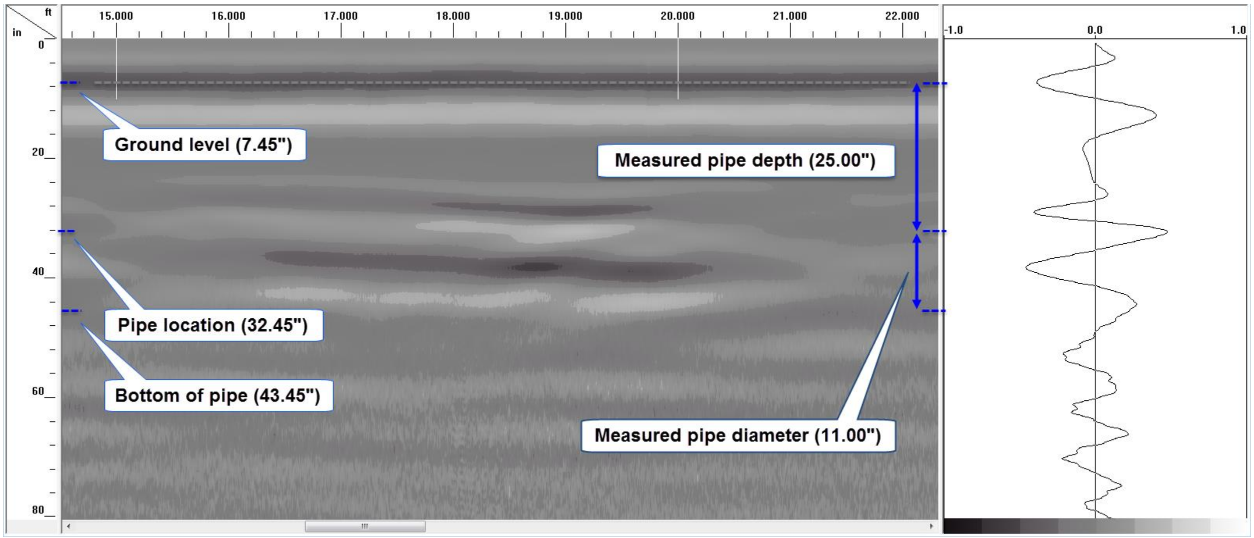

Figure 5-9: *Longitudinal GPR scan (left) and A-Scan (right) over Unwrapped 12" GFRP pipe*

diameter, hence the top and bottom reflections overlap, further contributing to the error in estimating the pipe diameter.

Figure 5-8 shows the GFRP pipe with CFRP strip at the top; the pipe is detected with clean reflected signal from the top and bottom of the pipe. Good reflection from the top of the pipe will make it possible to locate the pipe with GPR irrespective of the content of the pipe. It was also possible to estimate the pipe diameter because of prominent reflections from both the top and bottom of the pipe. This method of estimating pipe diameter will however be less reliable when the soil dielectric constant is significantly more than that of the pipe content as explained earlier. This will be more evident when we look at Dataset II.

Figure 5-9 shows the GFRP pipe without any surface wrap; the pipe is detected with short and weaker signal from the top (compared to the pipe bottom reflection) and continuous, stronger reflection from the bottom. Though the pipe is detected using the combination of top and bottom reflections in this case, it will be difficult to locate the pipe if its content absorbs the radar signal and makes it impossible to obtain reflections from the bottom of the pipe. It was also possible to estimate the pipe diameter from the recorded GPR signal reflections for this pipe.

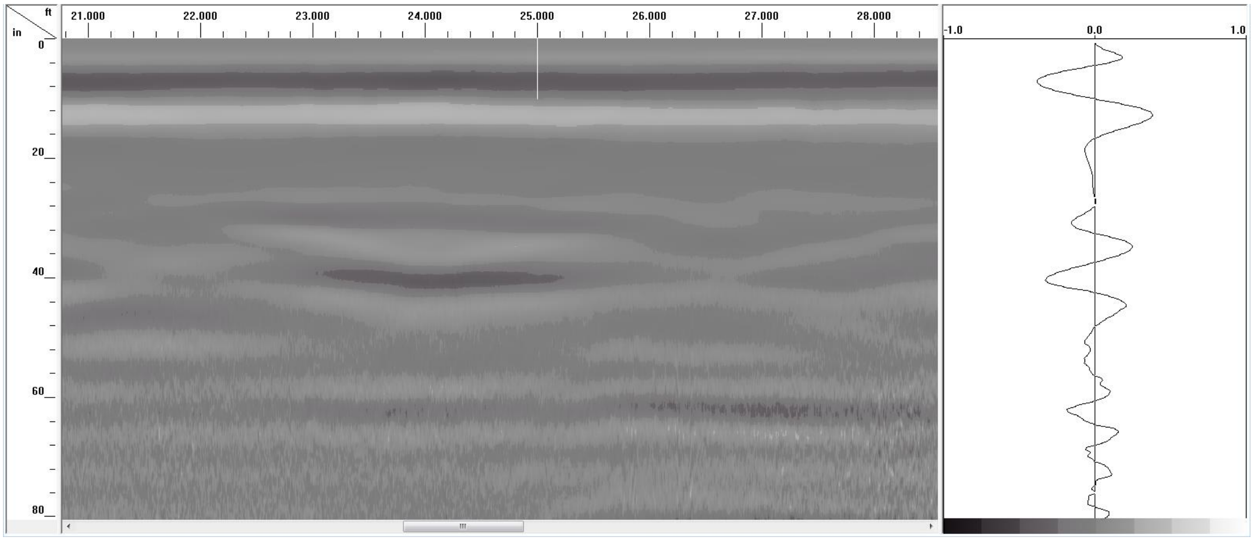

***Figure 5-10:** Longitudinal GPR scan (left) and A-Scan (right) over C. Nano p. 12" GFRP pipe*

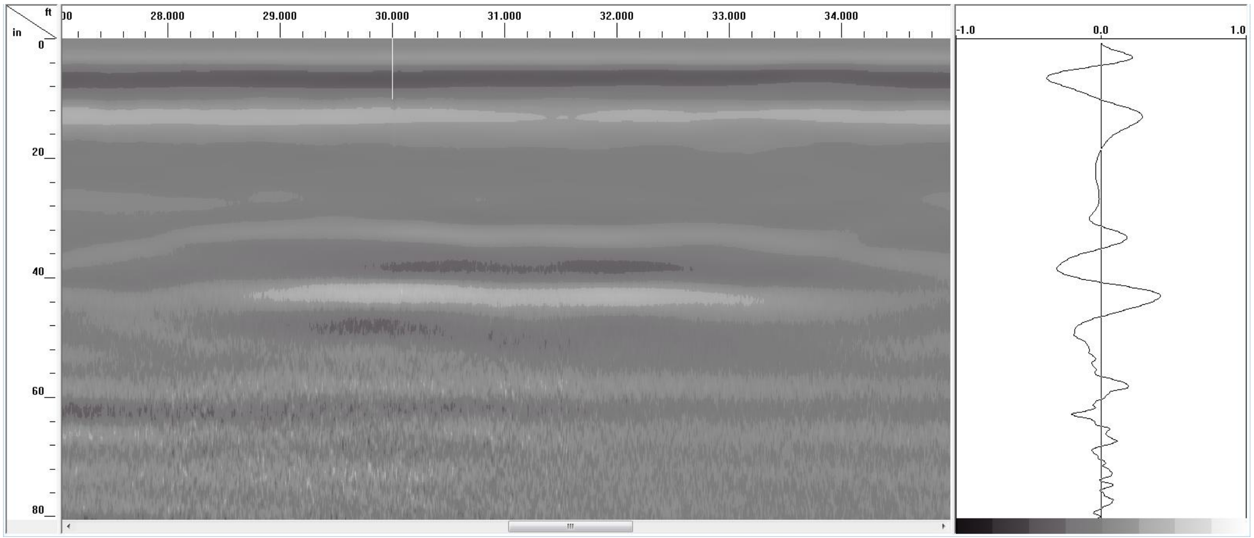

***Figure 5-11:** Longitudinal GPR scan (left) and A-Scan (right) over Al. Foil Strip 12" PVC pipe*

Figure 5-10 shows the GFRP pipe with carbon nanoparticle overlay; this pipe produced a good but very short reflection from the top of the pipe. This signal is weaker than the one produced by the GFRP pipe without any surface wrap in Figure 5-9. Thus, the carbon nanoparticle overlay did not improve the detectability of the buried pipe. This is because the carbon particles lacked connectivity as they were simply dispersed in the resin and did not constitute a conductive layer.

Figure 5-11 shows the PVC pipe with aluminum foil strip at the top; this pipe produced a very good reflection from the top of the pipe and making it possible to locate the pipe. The good reflection from the top of this pipe will also make it possible to locate the pipe with GPR irrespective of the content of the pipe.

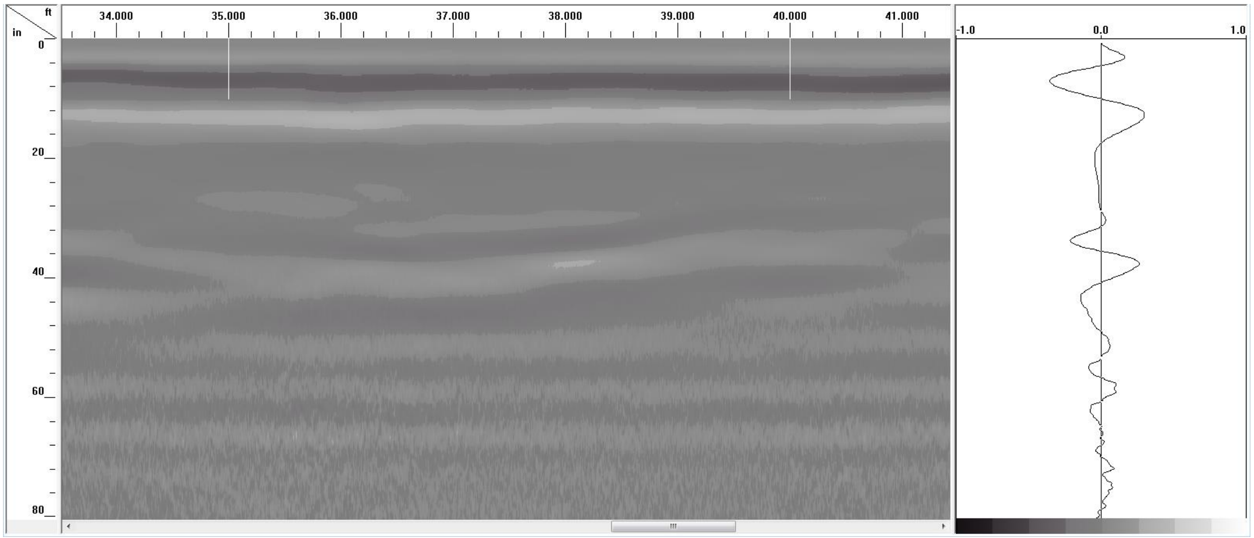

Figure 5-12: *Longitudinal GPR scan (left) and A-Scan (right) over Unwrapped 10" GFRP pipe*

Figure 5-12 shows the 10" GFRP pipe with no external surface wrap; this pipe produced a weak but continues reflection from the top of the pipe. This made it possible to locate the pipe in the test.

Figure 5-13 shows the steel pipe used as control specimen; this also produced a weak but continues reflection from the top of the pipe, and hence made it possible to locate the pipe in the test. Reflections from the steel pipe are more defined compared to the 10 inch diameter GFRP pipe, with the ends of the steel pipe clearly visible in the GPR B-Scan (left side of Figure 5-13).

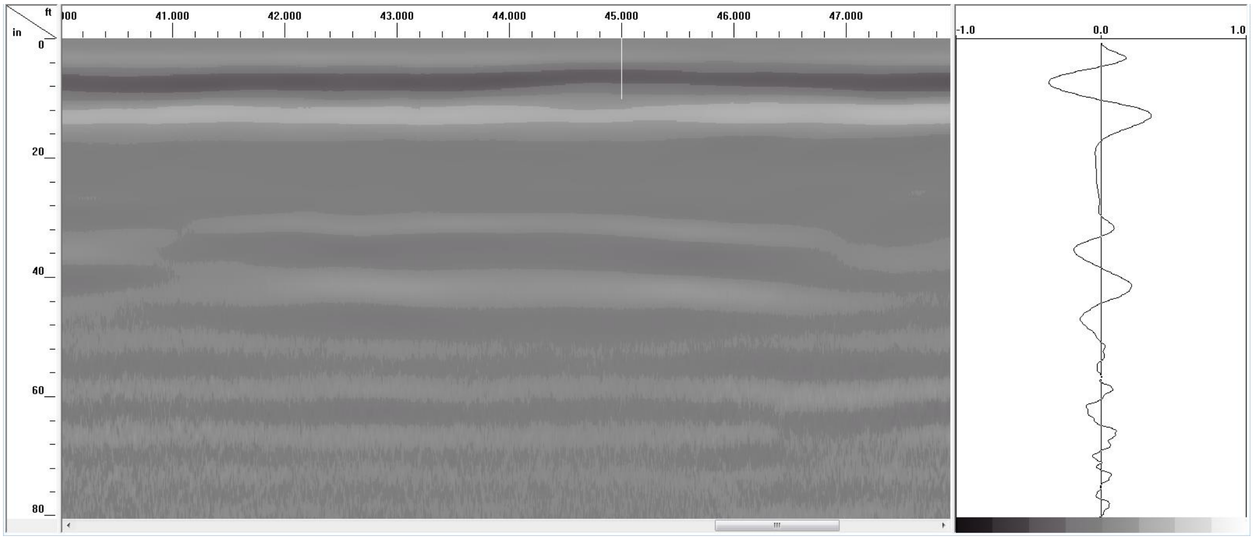

Figure 5-13: *Longitudinal GPR scan (left) and A-Scan (right) over 12" Steel pipe*

For most GPR applications in locating buried utility lines, scans are performed perpendicular to the expected direction of the utility line. Thus, scans were also performed perpendicular to the direction of the pipes for comparison. Figure 5-14 shows scans over some of the buried pipes. Scans from pipes with CFRP strip or aluminum foil strip produced the strongest reflections from the top of the pipe, as shown in Figures 5-14(a) and 5-14 (d). The 12" GFRP pipe with no wrap also produced a good reflection (Figure 5-14b), while the remaining pipes in Figures 5-14(c) and 5-14(e) produced very weak reflections. Thus, CFRP/carbon fabric strip and aluminum foil strips improve buried pipe detection, while carbon nanoparticle overlay does not offer any noticeable benefit in terms of pipe detection using GPR.

Figure 5-7(c) shows the raw GPR scan from all the pipes scanned using the 400 MHz antenna (for Dataset I), and Figure 5-7(d) shows the data in Figure 5-4(c) processed usign peak extraction to make it easier to identify the buried pipes in the GPR scan. It is difficult to identify any pipe in Figure 5-7(c), but extracting the reflected signal peaks makes it possible to see the GFRP pipe wrapped with CFRP strip and the GFRP pipe with no external surface wrap. The PVC pipe with aluminum foil strip at the top is also faintly visible in processed data in Figure 5-7(d). Thus, the 400 MHz antenna is less effective in locating the buried pipes at 2 ft. depth.

Figures 5-15 through 5-17 show details of the three pipes identified in the Figure 5-7(d). this includes the raw data, data with background noise removed, and the data with signal peaks extracted restpectively in each figure.

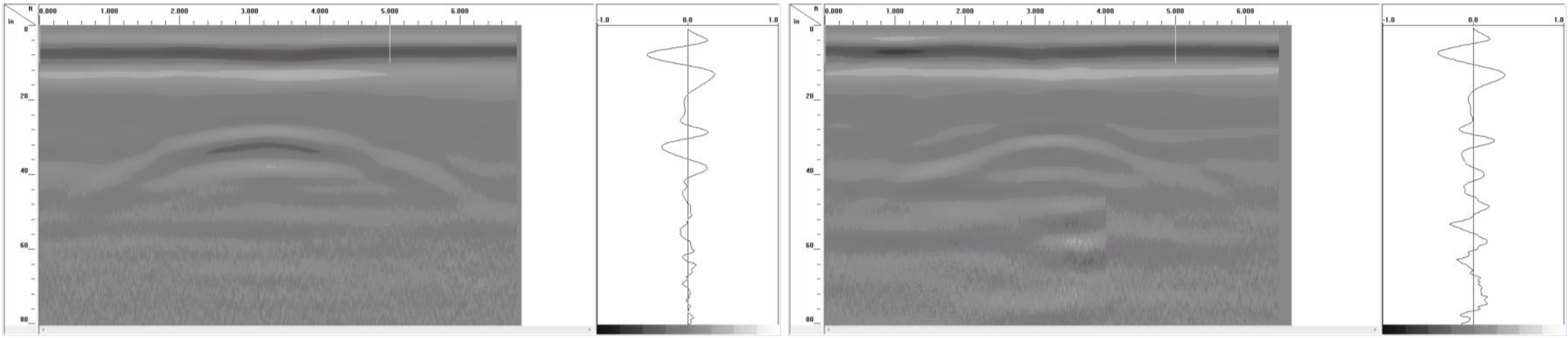

(a) GFRP pipe wrapped CFRP fabric

(b) Unwrapped GFRP pipe

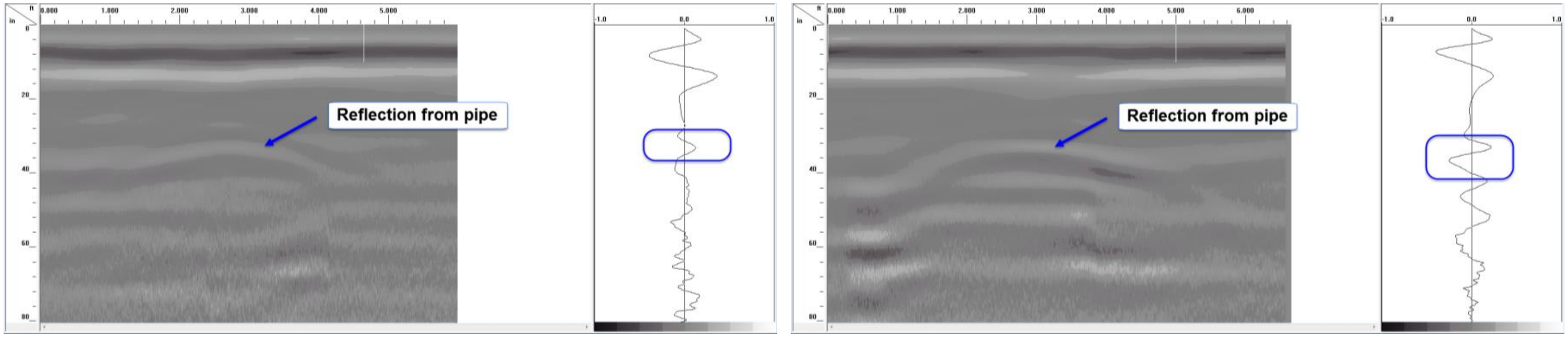

(c) GFRP pipe with carbon nanoparticle overlay

(d) PVC pipe wrapped with Aluminum foil strip

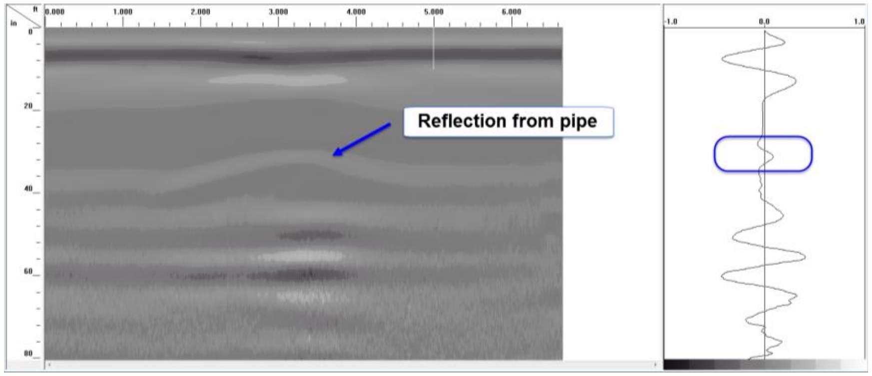

(e) Unwrapped GFRP pipe (10" diameter)

Figure 5-14: *Transverse scan over some of the pipes using 200 MHz GPR antenna for Dataset I*

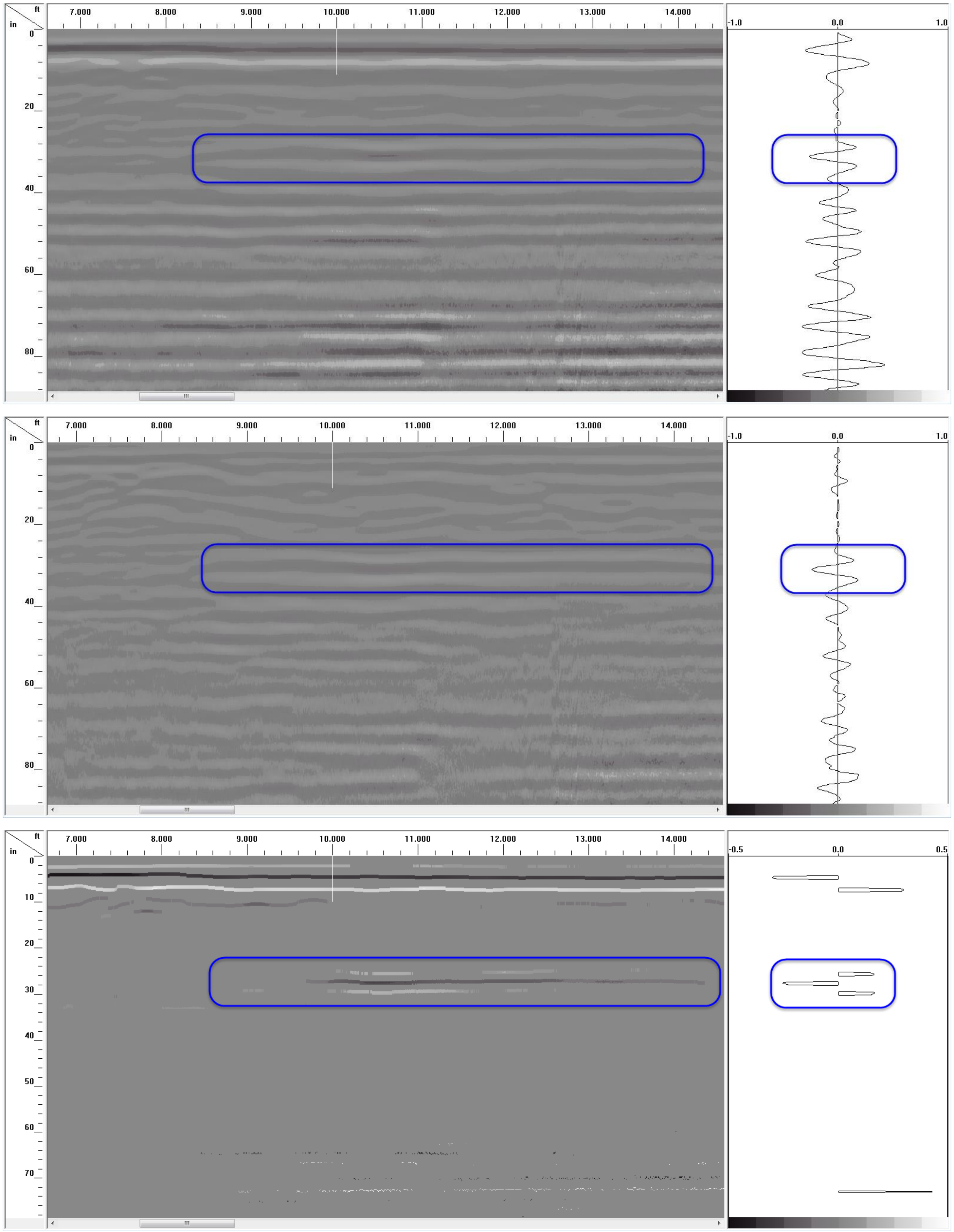

Figure 5-15: *Longitudinal scan over 12" CFRP Strip GFRP pipe using 400 MHz antennae: raw data (top), data with background noise removed (middle), and reflection peaks extracted from the data (bottom)*

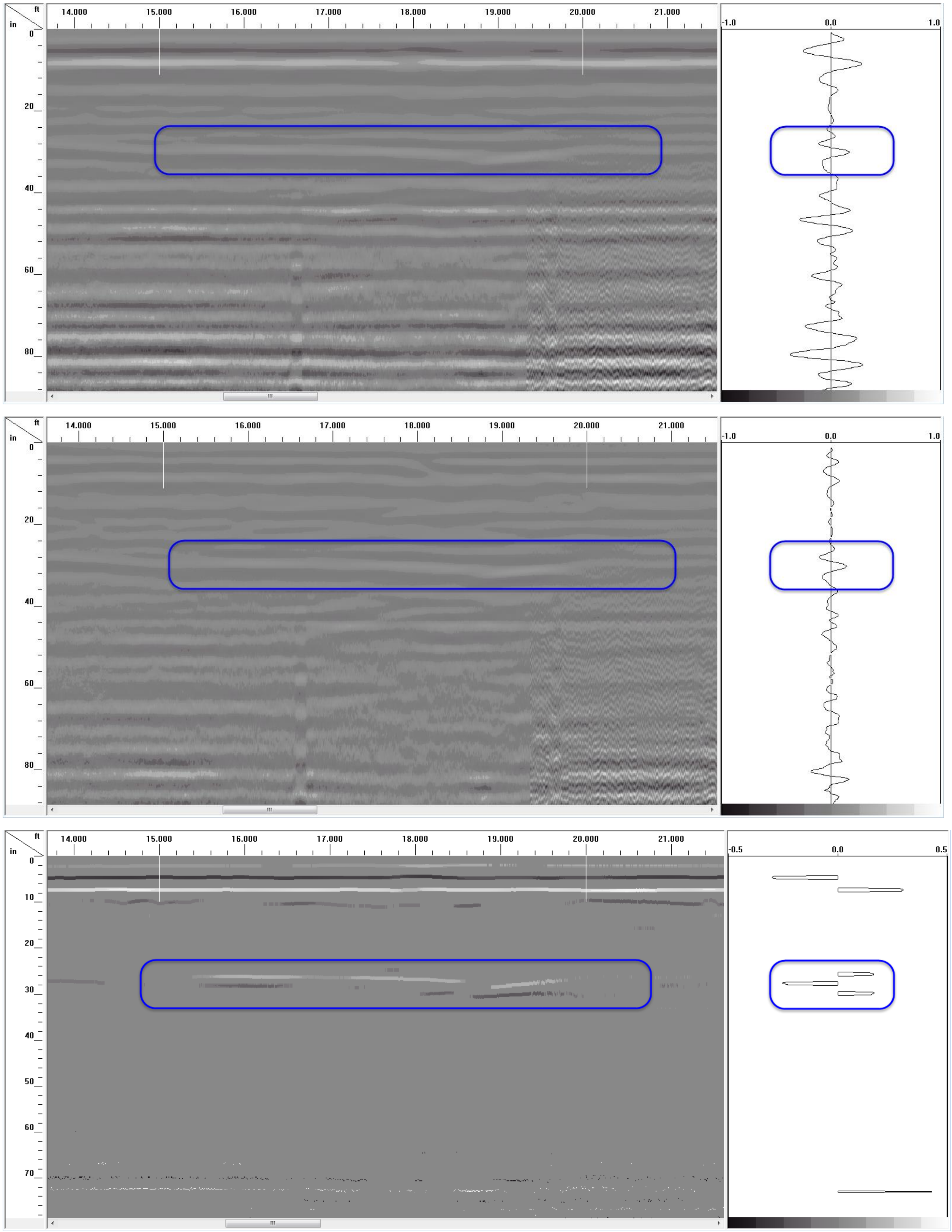

***Figure 5-16:** Longitudinal scan over 12" Unwrapped GFRP pipe using 400 MHz antennae: raw data (top), data with background noise removed (middle), and reflection peaks extracted from the data (bottom)*

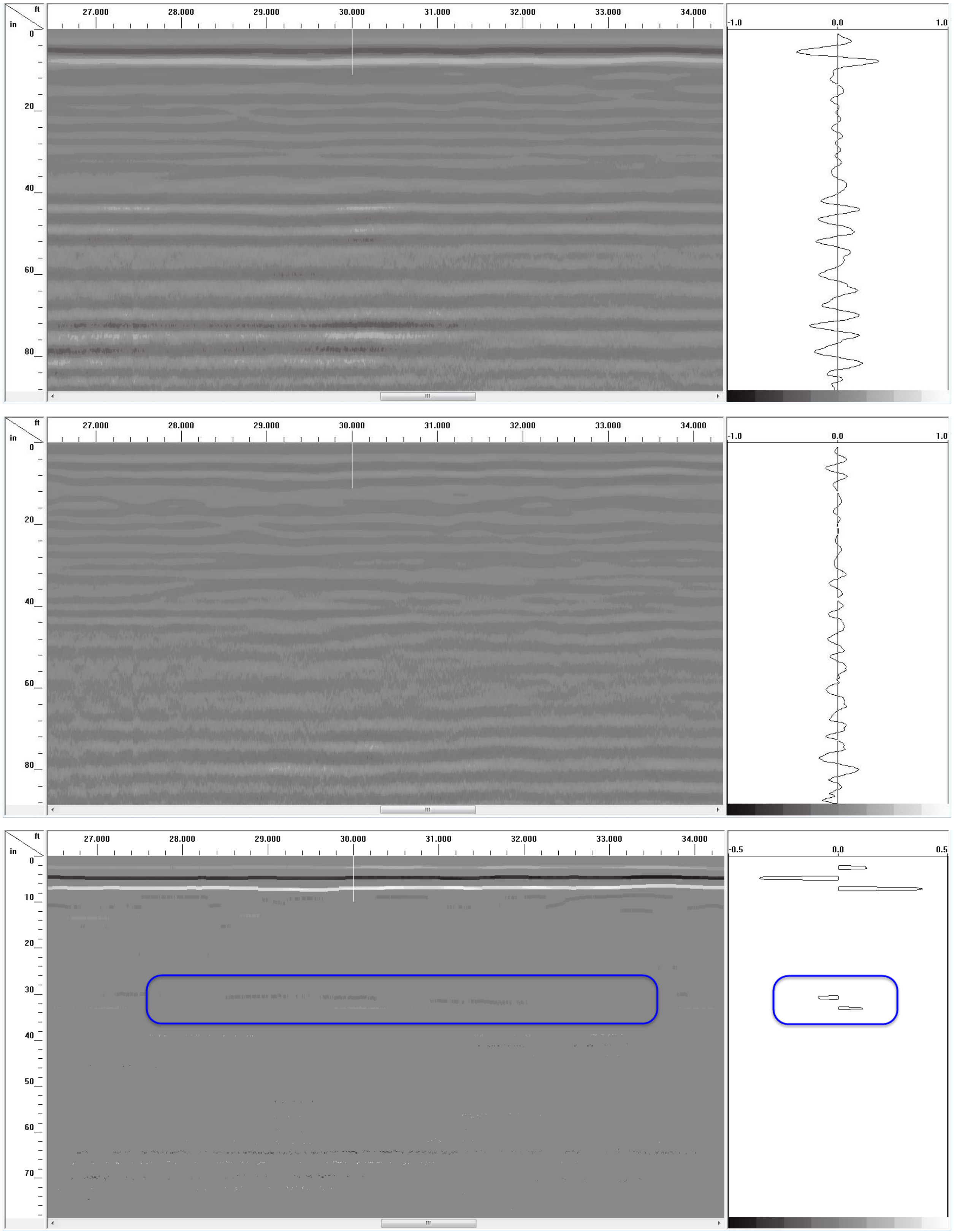

Figure 5-17: *Longitudinal scan over 12" Al. Foil Strip PVC pipe using 400 MHz antennae: raw data (top), data with background noise removed (middle), and reflection peaks extracted from the data (bottom)*

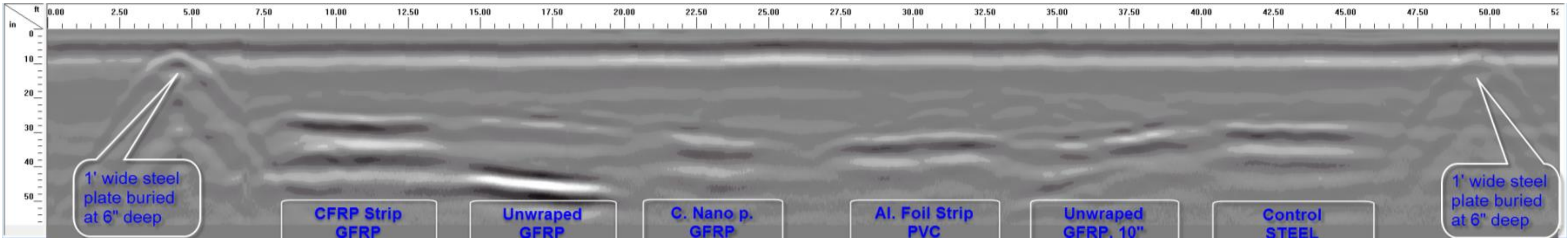

(a) Longitudinal scan along the full length of the pipe trench using 200 MHz GPR antenna

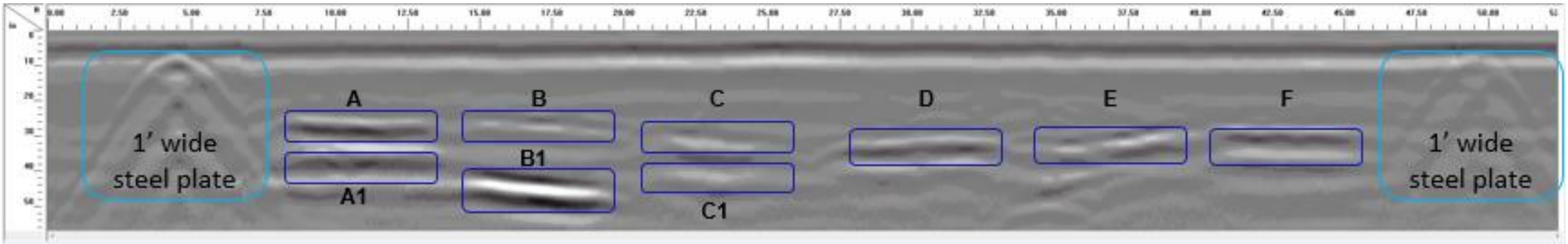

(b) Reflection details marked in the longitudinal scan from (a)

Figure 5-18: *Longitudinal scans over the pipe trench using 200 MHz antenna for Dataset II*

Table 5-3: *Description of features marked in Figure 5-18(b)*

Feature/ Label	**Object/Pipe Type**	**Result Description**
Steel plates	1 ft. wide steel plates	Appear prominently in the GPR scans
A	GFRP pipe with CFRP strip	Produced very strong reflection from both the top (A) and bottom (A1) of the pipe, pipe was clearly detected
A1	Reflection from bottom of pipe	
B	GFRP pipe with no wrap (12" diameter)	The pipe produced very weak reflection over sections of the pipe (B). Very strong reflection recorded from the bottom of the trench (B1)
B1	Reflection from bottom of trench	
C	GFRP pipe with carbon nanoparticle coating	Produced weaker reflection than D (over short section of pipe), from both the top (C) and bottom (C1) of the pipe. Portion of pipe detected
C1	Reflection from bottom of pipe	
D	PVC pipe with aluminum strip	Produced strong, continuous reflection, pipe was detected
E	GFRP pipe with no wrap (10" diameter)	Produced strong reflection over sections of the pipe, pipe was detected
F	Steel pipe	Produced strong continuous reflection, pipe was detected

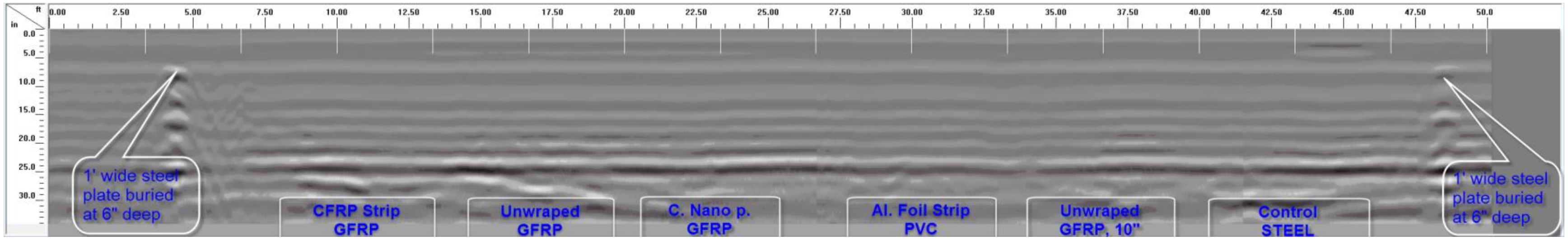

(a) Longitudinal scan along the full length of the pipe trench using 400 MHz GPR antenna

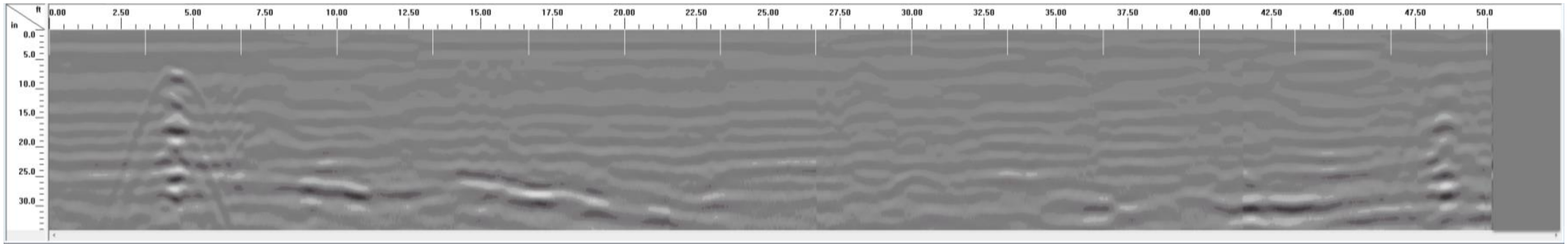

(b) Background noise removed from figure in (a)

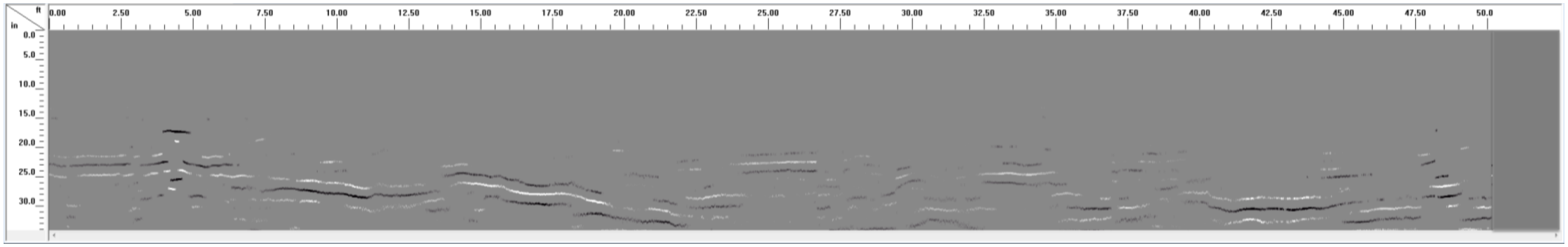

(c) Signal reflection peaks extracted from (b)

Figure 5-19: *Longitudinal scans over the pipe trench using 400 MHz antenna for Dataset II*

Figure 5-18 through 5-26 shows GPR scan for Dataset II. GPR survey for Dataset II was conducted in the winter when the ground surface was covered with snow, up to a depth of 3.75 inches. Soil volumetric water content and dielectric cosntants were higher for Datatset II as already shown in Table 5-2.

As shown in Figure 5-18, all the buried pipes wre detected with varying levels of clarity when the 200 MHz antenna was used. Details of the pipes and other features identified in this scan are marked in Figure 5-18(b) and summerized in Table 5-3. The GPR result presented in Figure 5-18 indicates that snow cover on the ground surface does not hinder the detection of buried pipes using GPR. Figure 5-19 shows that the 400 MHz antenna did not perform very well.

GPR data for each pipe in Figure 5-18 (200 MHz antenna) is further explored in Figures 5-20 through 5-25, showing the B-Scan to the left and A-Scan to the right of each figure. The depth of soil cover over the pipes was also estimated from the GPR data as shown in Figures 5-20 and 5-22, where the measured depth of 23.72" and 26.12" corresponds well with the actual depth of 2 ft. Similar to Dataset I, reflections from the bottom of some of the pipes make it possible to estimate the diameter of the pipe as shown in Figures 5-20 and 5-22. As explained earlier for Dataset I, the diameter of the pipe is estimated from the electromagnetic wave velocity, which is based on the average soil dielectric constant. This method of estimating pipe diameter is however less reliable when the soil dielectric constant is significantly higher/lower than that of the pipe content as explained earlier. Soil dielectric constant for this dataset was 26.77 compared to 1 for air. This explains why the estimated pipe diameters are 10.09" and 10.37" instead of 12". The estimated diameter will be accurate if the pipe content and the overlaying soil has similar dielectric constants, and the pulse width of the radar wave is less than the actual pipe diameter.

Figure 5-20 shows the GFRP pipe with CFRP strip at the top; the pipe is detected with clean reflected signal from the top and bottom of the pipe. Good reflection from the top of the pipe will make it possible to locate the pipe with GPR irrespective of the content of the pipe. It was also possible to estimate the pipe diameter because of prominent reflections from both the top and bottom of the pipe.

Figure 5-21 shows the GFRP pipe without any surface wrap; the pipe is detected with weak and discontinuous signal from the top, and continuous, very strong reflection from the bottom of the trench.

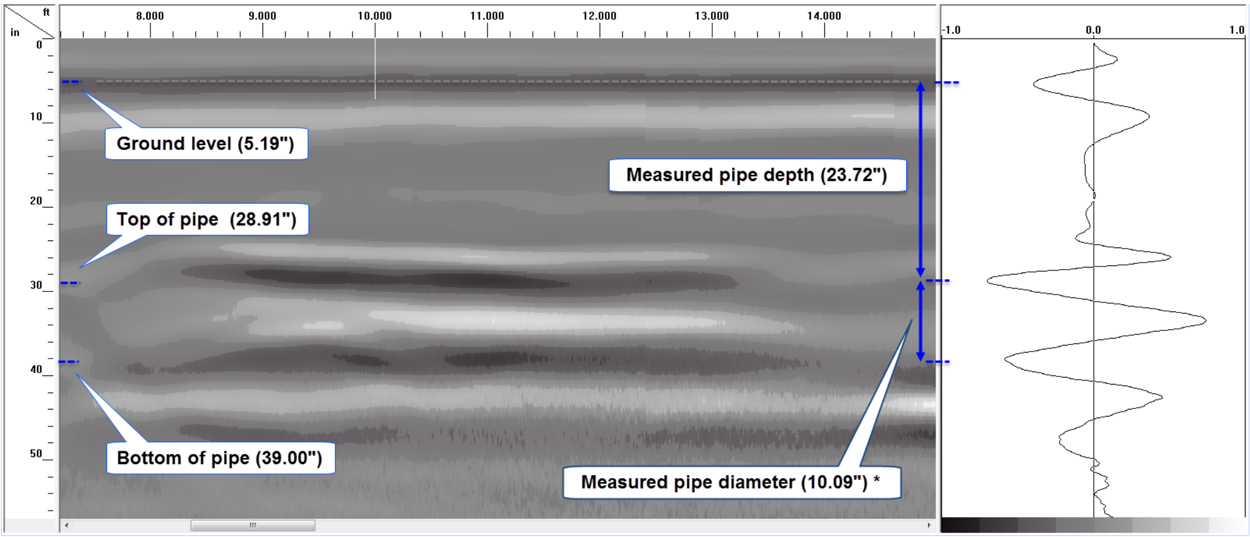

Figure 5-20: *Longitudinal GPR scan (left) and A-Scan (right) over 12" CFRP Strip GFRP pipe*

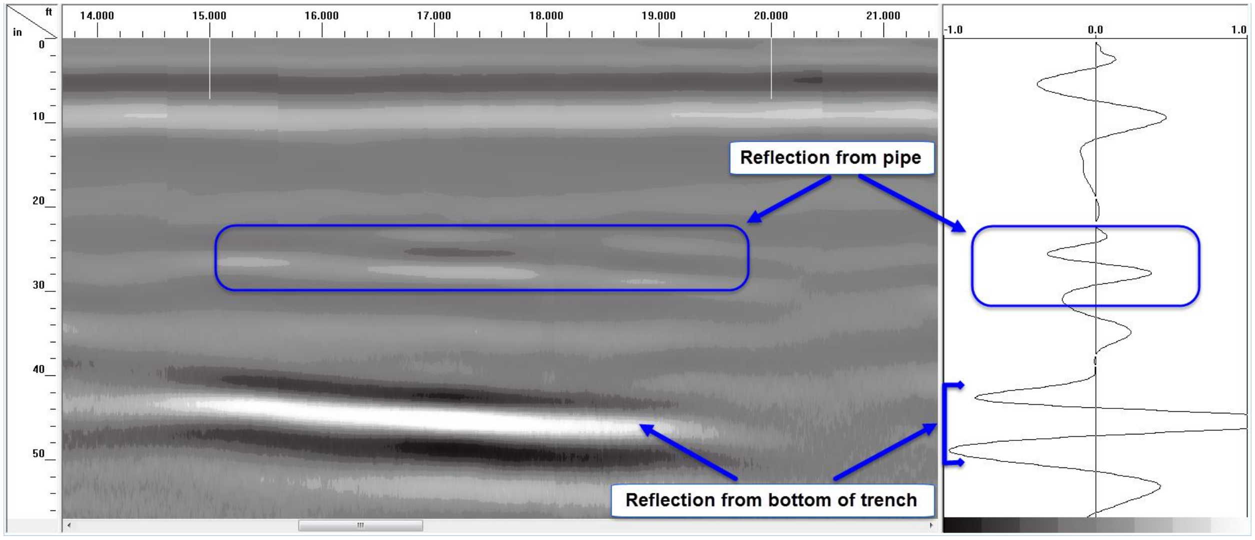

Figure 5-21: *Longitudinal GPR scan (left) and A-Scan (right) over Unwrapped 12" GFRP pipe*

Figure 5-22 shows the GFRP pipe with carbon nanoparticle overlay; this pipe produced a weak and very short reflection from both the top and bottom of the pipe. This signal is stronger than the one produced by the unwrapped 12" diameter GFRP pipe in Figure 5-21 but weaker than the one produced by the 10" GFRP pipe without any surface wrap in Figure 5-24.

Figure 5-23 shows the PVC pipe with aluminum foil strip at the top; this pipe produced a strong reflection from the top of the pipe thus making it possible to locate the pipe. The prominent reflection from the top of this pipe will also make it possible to locate the pipe with GPR irrespective of the content of the pipe.

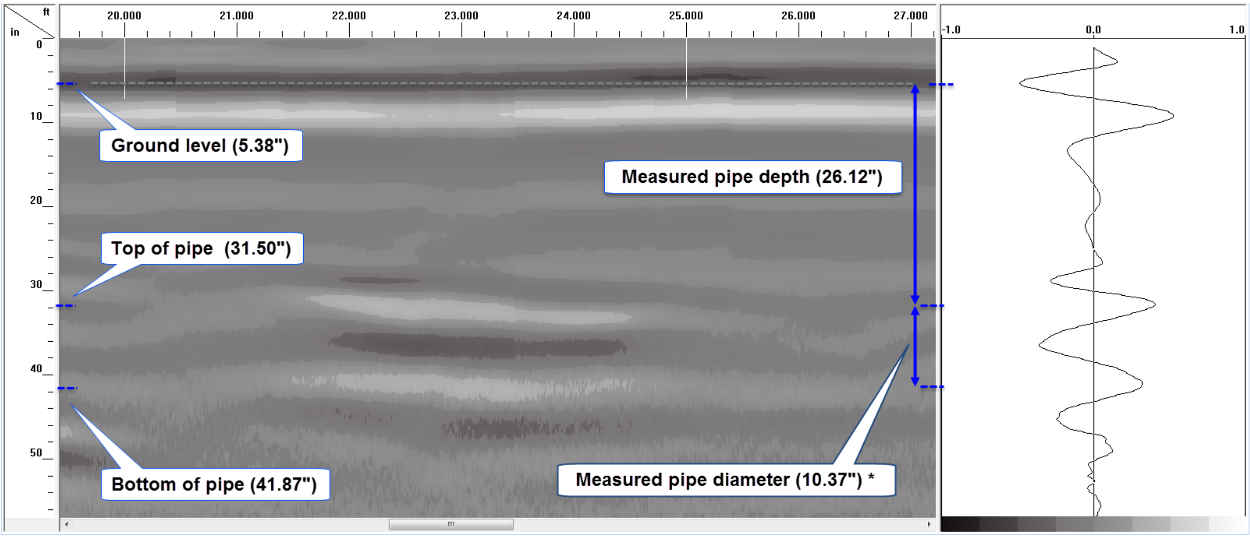

Figure 5-22: *Longitudinal GPR scan (left) and A-Scan (right) over C. Nano p. 12" GFRP pipe*

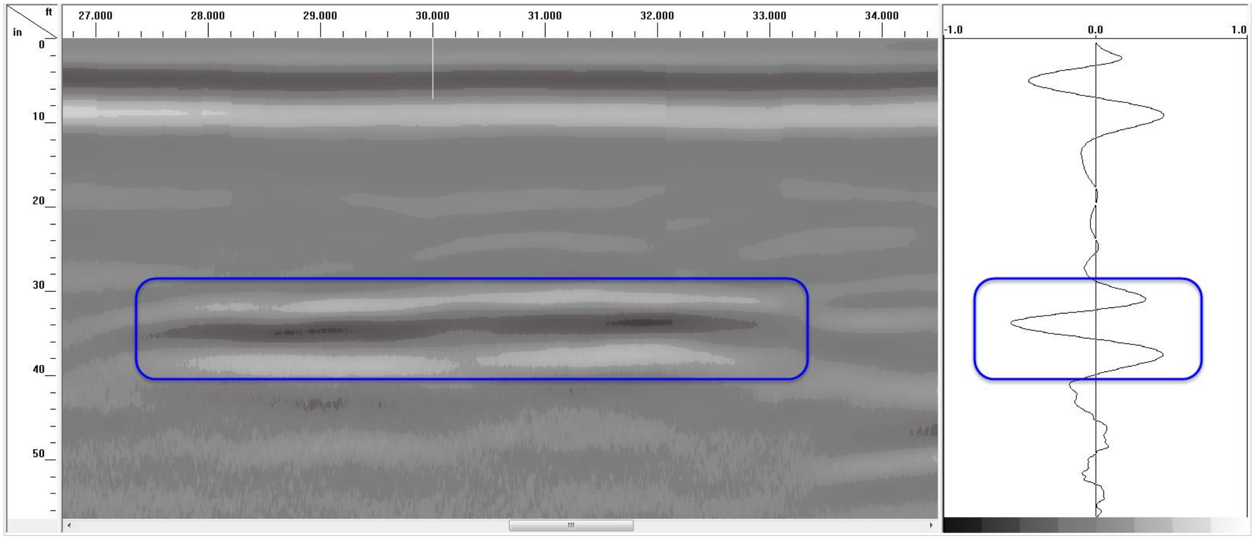

Figure 5-23: *Longitudinal GPR scan (left) and A-Scan (right) over Al. Foil Strip 12" PVC pipe*

Figure 5-24 shows the 10" GFRP pipe with no external surface wrap; this pipe produced a strong but discontinuous reflection from the top of the pipe. The strong reflection made it possible to locate the pipe in the test.

Figure 5-25 shows the steel pipe used as control specimen; this pipe produced a strong and continuous reflection from the top of the pipe, and hence made it possible to locate the pipe in the test. Reflections from the steel pipe and PVC pipe with aluminum foil strip in Figure 5-23 are more defined compared to the 10" diameter GFRP pipe (Figure 5-24), which makes it easier to locate the steel and PVC with aluminum strip pipes in the respective GPR B-Scans.

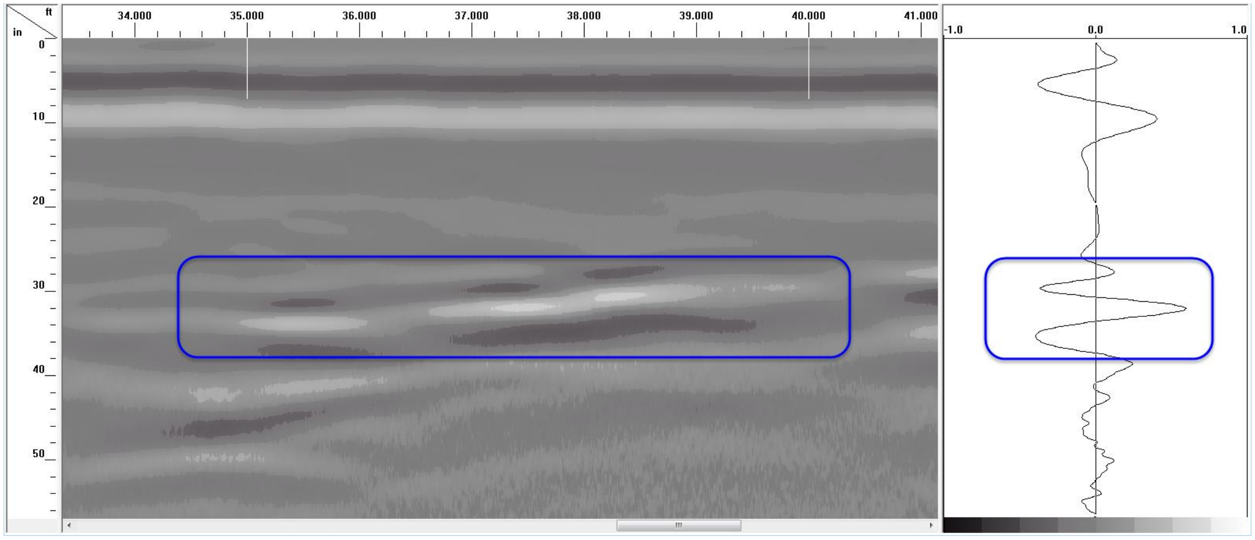

__Figure 5-24:__ Longitudinal GPR scan (left) and A-Scan (right) over Unwrapped 10" GFRP pipe

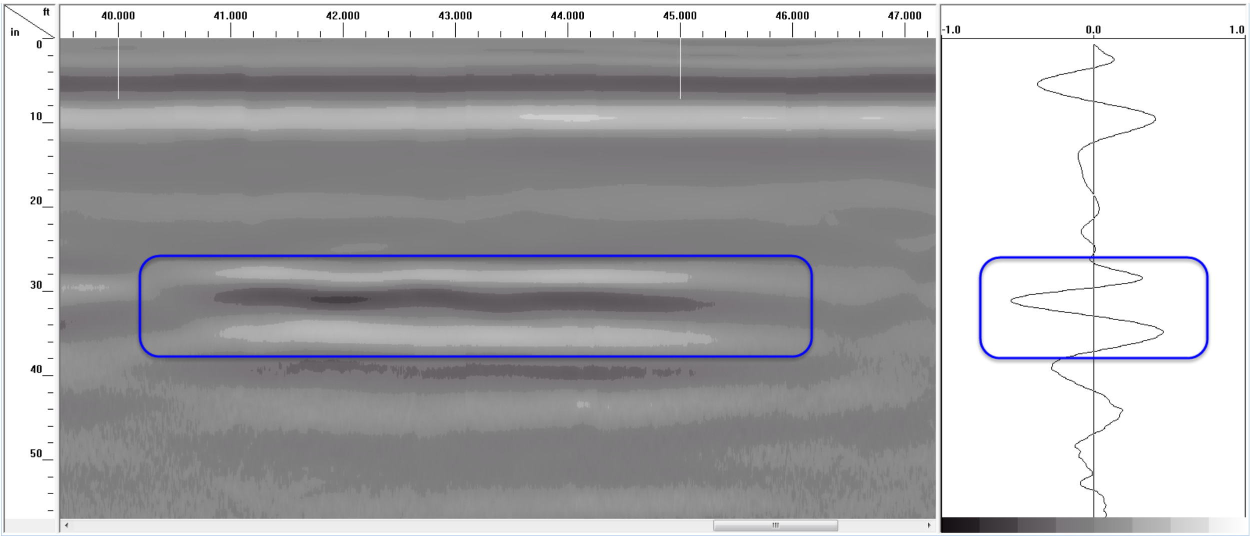

__Figure 5-25:__ Longitudinal GPR scan (left) and A-Scan (right) over 12" Steel pipe

It is interesting to note that the signal from the steel pipe in Figure 5-25 (soil-to-steel) has a reverse polarity compared to the signal from the unwrapped GFRP pipe (soil-to-GFRP) since GFRP has a lower dielectric constant compared to that of moist soil.

Figure 5-26 shows transverse scans over some of the buried pipes in Dataset II using the 200 MHz antenna. Scans from pipes with CFRP strip or aluminum foil strip produced the strongest reflections from the top of the pipe, as shown in Figure 5-26(c). The seel pipe also produced a strong reflection (Figure 5-14e), while the remaining pipes produced weak reflections.

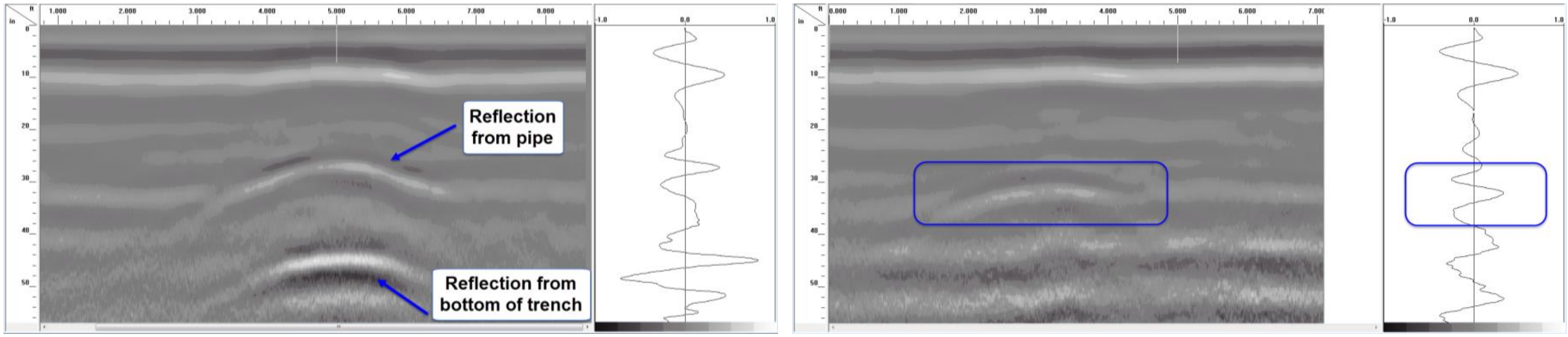

(a) Unwrapped GFRP pipe

(b) GFRP pipe with carbon nanoparticle overlay

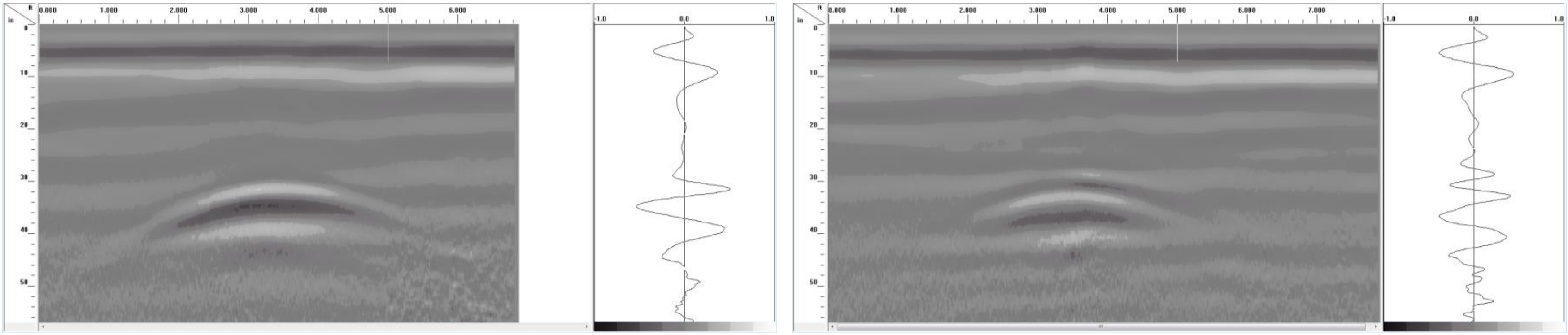

(c) PVC pipe wrapped with Aluminum foil strip

(d) Unwrapped GFRP pipe (10″ diameter)

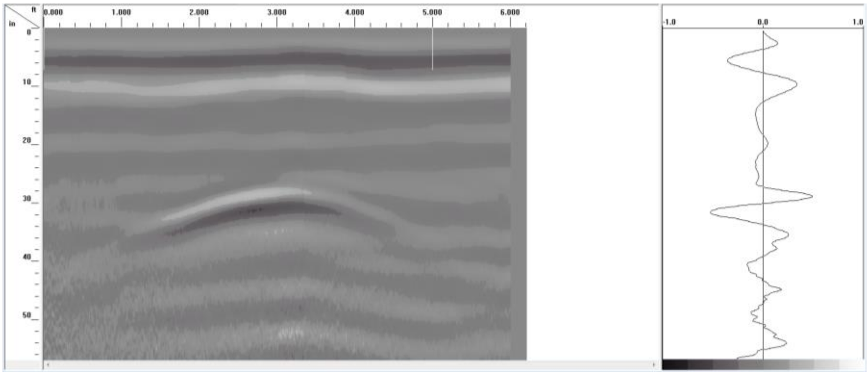

(e) Steel pipe

Figure 5-26: *Transverse scan over some of the pipes using 200 MHz GPR antenna for Dataset II*

Figure 5-19 shows the buried pipes scanned using the 400 MHz antenna for Dataset II. Figures 5-19(a), 5-19(b), and 5-19(c) show the raw GPR scan, data with background noise removal applied, and data with background noise removal and peaks extraction applied respectivly. As can be seen in Figure 5-19(b), only three of the pipes could be identified after background noise removal; the GFRP with CFRP strip, 12" diameter unwrapped GFRP, and the steel pipe. Extracting reflected signal peaks (Figure 5-19c) made it a bit easier to identify the individual pipes in the scan. This result reinforces the fact that, the 400 MHz antenna is less effective in locating the buried pipes at 2 ft. depth. On the other hand, the 200 MHz antenna performed very well as shown in Figures 5-20 to 5-26.

5.6 Conclusions

This study investigated the detectability of non-metallic pipes buried at 2 ft. depth using GPR. From the data presented in this chapter, it can be concluded that, it is possible (but difficult) to detect buried non-metallic pipes without any surface modification, up to 2 ft. depth using GPR provided the right antenna frequency is used. It can also be concluded that, the use of CFRP and aluminum foil overlays (in the form of strips) significantly improves the detectability of buried non-metallic pipe sections such as GFRP and PVC. In cases where the buried Unwrapped GFRP pipes are detectable (with weaker reflected signals), the addition of carbon or aluminum foil overlays significantly increases the strength of the GPR signal and makes it easier to identify the pipe sections. This is because CFRP and aluminum are electrical conductors, hence they reflect the incident radar waves much better than non-conductors. It is observed from this study that, the carbon fabric strip/overlay produced stronger signal reflections compared to aluminum foil strip/overlay.

An earlier study entitled *“Advancement in the Area of Intrinsically Locatable Plastic Materials”* [35] found that, buried non-metallic pipes (GFRP and PVC) are difficult to detect using GPR beyond 2 ft. depth; however, the addition of CFRP and aluminum foil overlays made it possible to detect these pipes beyond 2 ft. depth in the earlier study. The previous study also concluded that, the production of stronger and easier to interpret GPR signal reflections from buried non-metallic pipes with carbon fabric or aluminum foil overlays implies that, the depth at which pipes are buried could be increased beyond the maximum 4 ft. depth that was used in the study and still be detected.

It is observed from this study that the carbon nanoparticle coating/overlay did not provide any noticeable benefit in terms of improving the detectability of the buried pipe. The explanation for this is that, there is no interconnection between the individual nanoparticles, hence the coating did not act as a conductor as was expected. This is evident in the A-Scans shown in Figures 5-8 through 5-13, and 5-20 through 5-25 where pipes with conductive overlays/surfaces such as the GFRP pipe with CFRP strip, the PVC pipe with aluminum foil strip, and the steel pipe produced signal reflections with reversed polarity (negative reflection peak) while reflections from non-conductive pipes did not experience any reversal in polarity. The GFRP pipe with carbon nanoparticle coating did not experience reversal in signal polarity, indicating that it is not acting as a conductor.

Finally, it is observed that the 200 MHz GPR antenna is ideal for buried pipe detection. The 400 MHz antenna was much less effective in locating the buried pipes at 2 ft. depth. The 400 MHz antenna experiences higher signal attenuation compared to the 200 MHz one. Detailed analysis of the GPR signal attenuation for the different antennae along with the underlying theory can be found in another publication [36].

6 GAS LEAK DETECTION

6.1 Introduction

Utility production, transportation, and distribution drive the economy like few other forces. In the United States alone, there are over 3 million miles of oil, gas, and other utility pipelines buried underground. When these pipelines are buried, it is essential that an accurate mapping of their location be made to prevent damage to the lines, as well as to avoid accidentally rupturing the lines which could result in an emergency situation. Within the United States, many of these pipelines are falling into disrepair due to old age, and it has become necessary to revamp this infrastructure system.

A major facet of this revamp is the modernization of the materials with which the pipelines are constructed. These modern materials will allow the pipeline to be constructed in a more cost effective manner, and will also allow a much greater lifetime of use for the pipeline itself. Unfortunately, many of the modern materials are not made of metal, and, as a result, are difficult to detect underground and accurately map by traditional means. The focus of this research is to analyze new piping materials to determine their viability for use in an underground pipeline system, and to develop a method for the detection of underground leaks. New methods and techniques will be used to detect the pipes themselves and the guarantee the structural integrity of the piping system.

This particular section of the report investigated a leaking underground gas pipe. The experiment in the laboratory involved the construction of a box containing soil and a buried pipe. A small hole was drilled in the pipe to simulate a leak underground. A flow model was developed and tested experimentally to predict the leak rate knowing the hole size or conversely, knowing the leak rate, the size of the leak could be calculated. In addition, a gas-sensing system was placed at the surface of the soil and the detection of the leaking gas was verified. Finally, the diffusion of the leaking gas through the soil was measured and modeled using applicable mathematics.

6.2 Test Set-Up

Initially it was decided to simulate a leaking buried pipe by constructing a wooden box into which a pipe of up to six inches in diameter could be inserted. The pipe was then covered with a layer of soil. The size of this first box was roughly 3 feet wide by 5 feet long by 5 feet high. The box was then filled with crushed stone and soil to bury the pipe. The pipe had a tiny hole drilled in its wall to simulate a gas leak underground. Figures 6-1(a), 6-1(b), and 6-1(c) show schematic drawings of the initial box. The first wooden box was filled with highly saturated clay that was not porous once it dried, preventing the gas from flowing through the clay and out of the surface of the soil. Rather than digging all the non-porous soil out of the old box, it was decided to build a new wooden box for conducting additional experiments. This new box, shown in Figures 6-2(a), 6-2(b), and 6-2(c), was constructed with several improvements over the previous box. All of the seams were sealed with a silicone caulking and the inside of the box was lined with a three-millimeter thick plastic lining. The dimensions of the new box were roughly 1.5 feet wide by 5 feet long by 5 feet high. These dimensions were chosen so to reduce the volume of the box and thus speed up the diffusion experiments. The soil placed in the box was hand-mixed with sand, gravel, and top soil at a ratio of 1:1:2 respectively. An eight-inch diameter aluminum pipe was placed near the bottom of the box and acted as a sheath to allow for easy insertion and removal of test pipes. Reducing "Fernco" fittings were used to create a seal between the aluminum pipe and the test pipe. Overall, the new box provided a better and more flexible representation of gas flow through a porous medium, and therefore was a better mimic of an underground pipe leak. All of the experiments described below utilized this smaller and improved box. The box was initially filled to a depth of about 18 inches with the hand-mixed soil, and tests were run to ensure that carbon dioxide, the gas used for the leak detection, was leaking through PVC test pipe and the soil, and being detected (see description below) at the top of the box.

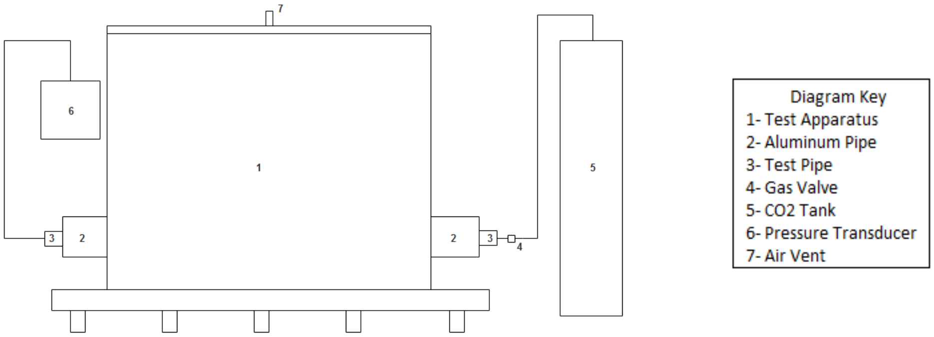

(a)

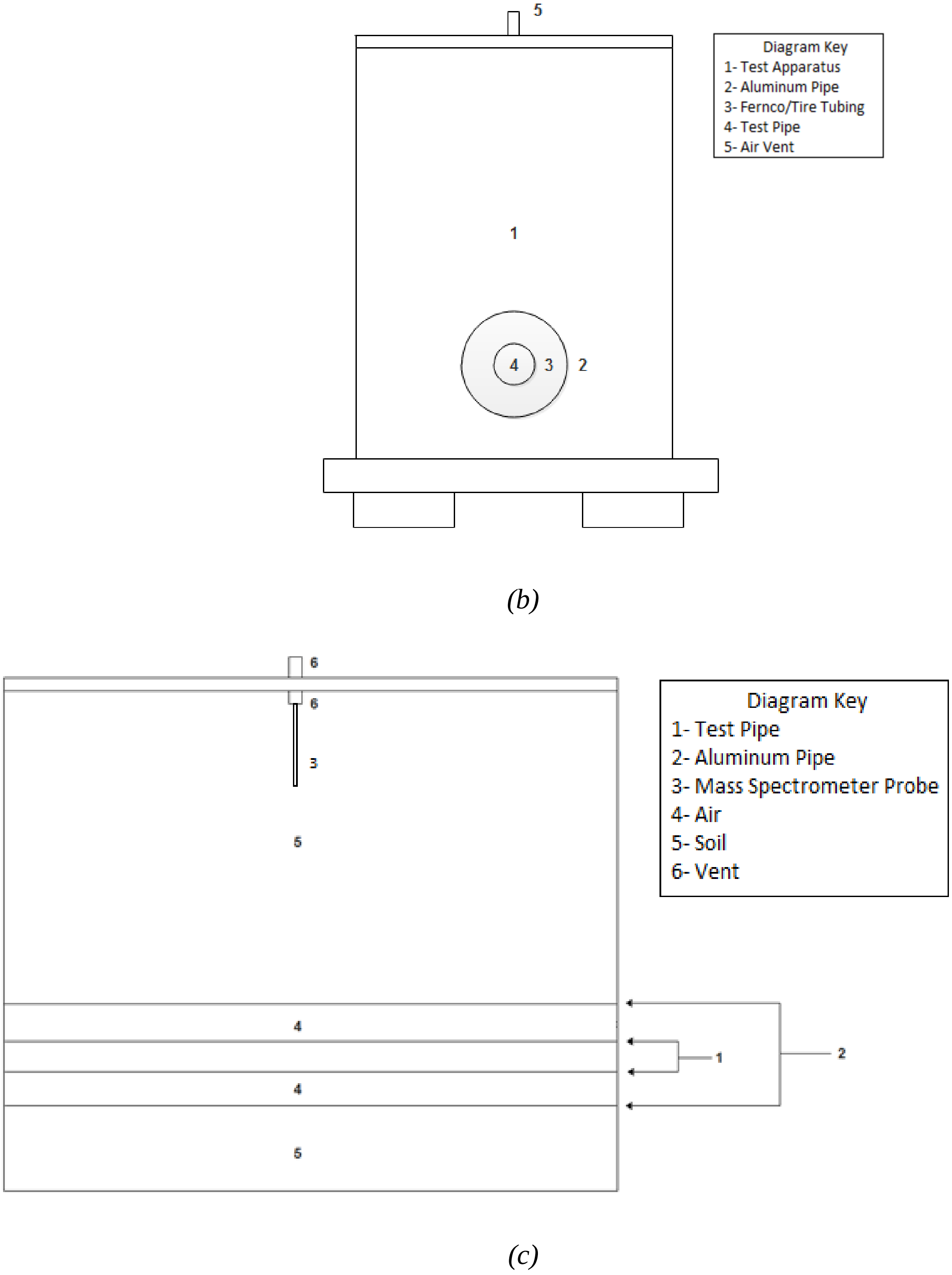

Figure 6-1: *(a) Testing apparatus schematic diagram side view, (b) Testing apparatus schematic diagram end view, and (c) Testing apparatus schematic, interior view*

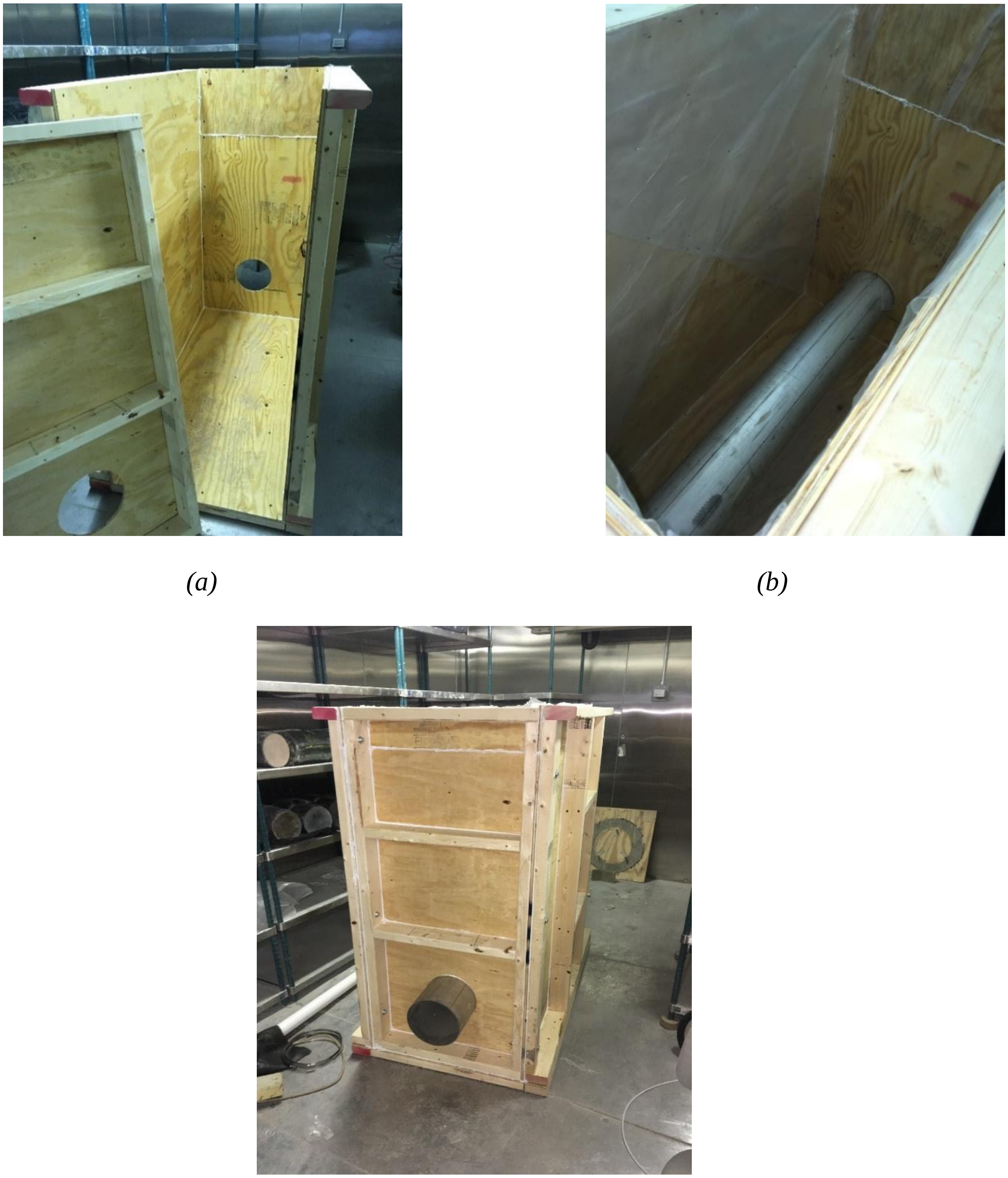

(a)

(b)

(c)

Figure 6-2: *(a) New wooden box, showing caulked seams, (b) Interior of assembled box, and (c) Exterior of assembled box*

Before any experimental trials could be conducted, a model pipe was selected. The chosen piping material for this model was a standard 2-inch PVC pipe roughly 56 inches long to allow for overhang outside of the aluminum pipe. This overhang was necessary to allow for the Fernco seal to be placed around outside of the PVC pipe as well as fitting around the edge of the aluminum pipe. The rubber seals were secured around the outside of both the 8-inch and 2-inch pipes with standard hose clamps. To accurately measure the pressure inside the test pipe, an Omega PX409-100GUSBH pressure transducer was connected to one end of the PVC pipe. The transducer is capable of measuring pressures up to 100 psig and is accurate to ±0.08%. The transient pressure data were logged by a computer. A cylinder of carbon dioxide (CO_2) was connected to the other end of the pipe through a standard ball valve. Carbon dioxide was selected as a surrogate for methane since it is non-toxic and readily available. The ball valve was placed in-line with the inlet from the CO_2 tank so that the system could be filled with CO_2 and then isolated from the CO_2 tank. A pressure regulator was installed on the CO_2 cylinder to allow the pressure inside the test pipe to be controlled precisely. Figure 6-3 shows the CO_2 tank and regulator.

Figure 6-3: *CO_2 Cylinder and pressure regulator*

A hole with a diameter of 0.0135 inch (No. 80 drill bit) was drilled into the mid-point of the length of PVC pipe to allow for the simulation of a gas leak in the system. The outer 8-inch pipe had several bigger holes in it to allow the gas to escape into the soil bed.

To detect the CO_2 leaking from inside of the PVC pipe, additional gas-sensing equipment was needed. The chosen experimental apparatus was an on-line mass spectrometer. The mass spectrometer for this analysis was the *LM99 Cirrus*, manufactured by MKS Instruments. The mass spectrometer can detect very low quantities of CO_2 (down to parts per million) in the air and was used to measure the concentration of CO_2 at the surface of the soil in the box once the CO_2 from the tank was released into the apparatus and the leak simulation tests began. Figure 6-4 shows the mass spectrometer as well as the computer necessary to operate it.

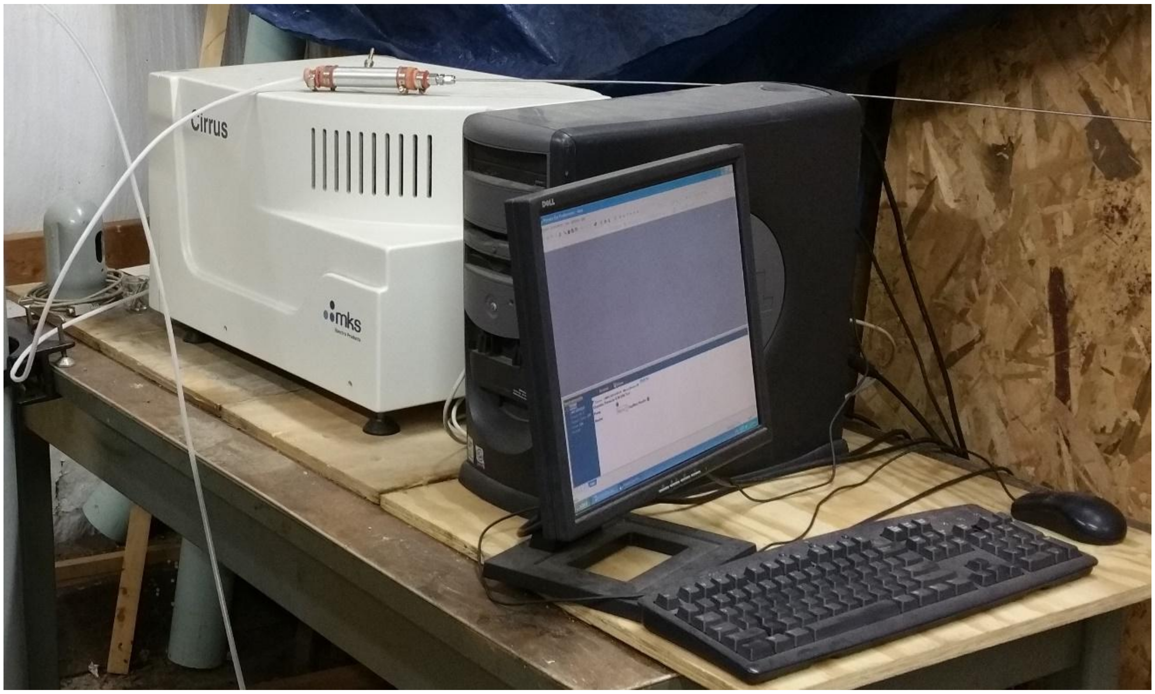

Figure 6-4: *Mass spectrometer and associated experimental equipment*

6.3 Test Results – Flow Studies

6.3.1 Gas Detection

Preliminary tests were performed to verify that the mass spectrometer was indeed capable of detecting the gas leaking from the pipe buried under the porous soil. To this end, the pressure regulator was set at a constant delivery pressure to give a steady flow rate and left to run so that as the CO_2 leaked into the box and diffused through the soil layer, the presence of CO_2 was detected at the surface of the soil inside the test box. This increase of CO_2 concentration was detected and the resulting data are shown Figure 6-5 which is a plot of the concentration (in arbitrary units) vs.

time. As can be seen, the mass spectrometer did indeed detect the leak of carbon dioxide when its probe was placed directly near the top surface of the soil.

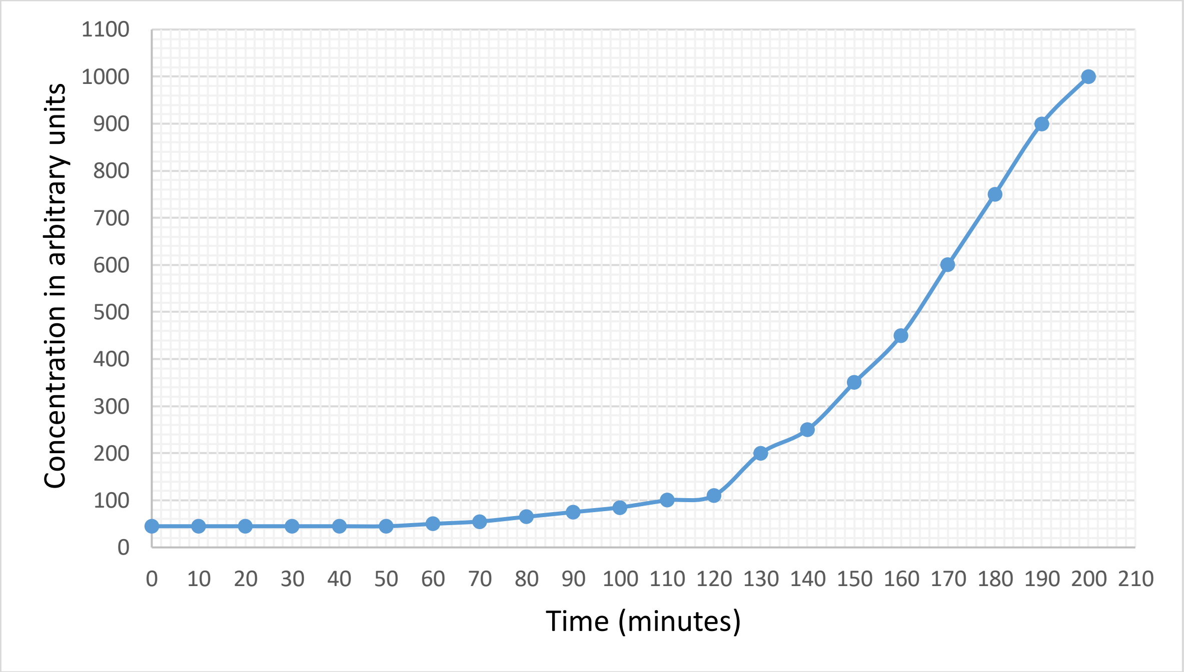

Figure 6-5: *Concentration of CO_2 as a function of time for a leak in the test pipe (expressed as arbitrary pressure)*

6.3.2 Leak Modeling

Trials were also run to model the rate at which the gas was leaking out of the “simulated” leak in the buried pipe. The experiment began by pressurizing the pipe to a pre-determined level and closing the valve between the pipe and the gas cylinder. The pressure in the pipe then decreased as the gas leaked out into the soil. The pressure vs. time data were fit to an appropriate mathematical model. Since the mass flow rate out of the PVC pipe is characterized as being choked, the equation used to model the mass flow rate through the leak hole in the PVC pipe is:

$$\dot{m}(t) = C_0 A P(t) \sqrt{\frac{\gamma g_c M}{R T_0} \left(\frac{2}{\gamma+1}\right)^{\frac{\gamma+1}{\gamma-1}}} \tag{6-1}$$

where:

$\dot{m}$ = Mass Flow Rate (lb_m/sec)

C_0 = Discharge Coefficient

A = Area of Leak Hole (ft^2)

P(t) = Pressure in the Pipe in psia with respect to time (psia)

γ = Heat Capacity Ratio of the Gas

g_c = Mass/Force Conversion Factor (32.17 $ft \cdot lb_m/lb_f \cdot sec^2$)

M = Molecular Weight of the gas (lb_m/lb_{mole})

R = Universal Gas Law Constant (1545 $ft \cdot lb_f/lb_{mole} \cdot R$)

T_0 = Absolute Temperature of Gas (R)

Equation 6-1 was then simplified to:

$$\dot{m}(t) = KP(t) \tag{6-2}$$

where K is a collection of constants:

$$K = C_0 A \sqrt{\frac{\gamma g_c M}{R T_0}\left(\frac{2}{\gamma+1}\right)^{\frac{\gamma+1}{\gamma-1}}} \tag{6-3}$$

It was possible to do this simplification because all the parameters in Equation 6-1 are constants except for the upstream pressure in the pipe and the mass flow rate. This creates a direct and simple relationship between the mass flow rate and the gas pressure in the pipe. Also, since the pressure inside the pipe can vary with time, the equation captures the linear relationship between the transient mass flow rate and the pressure provided that the flow stays in the choked regime. The experiment was repeated for several different starting pressures and the data are shown below in Figure 6-6. The collection of constants, K, was found to be 2.647 x 10^{-6} $\frac{lbm}{\sec \cdot psia}$ by using an experimentally-determined value for C_0 = 0.666.

Further since the mass flow of a gas can be related to the gas pressure through the ideal gas law, it is possible to integrate Equation 6-2 and derive and expression for the pressure as a function of time as the gas leaks from the pipe. The resulting expression for the internal pressure vs. time is shown in Equation 6-4.

$$\ln\left(\frac{P(t)}{P_0}\right) = -kt \tag{6-4}$$

Following the trend described by Equation 6-4, the simplest way to validate the theoretical assumption of choked flow was to plot the natural log of the transient pressure divided by the initial pressure versus time and determine a line of best fit. The slope of the best fit line yields a value for the constant, k, from Equation 6-4. Since all the values from the aforementioned plots as seen in Figure 6-6 (a), (b), (c), and (d) were within five percent, the best fit value of k is found to be 2.34 x 10^{-3} sec^{-1}.

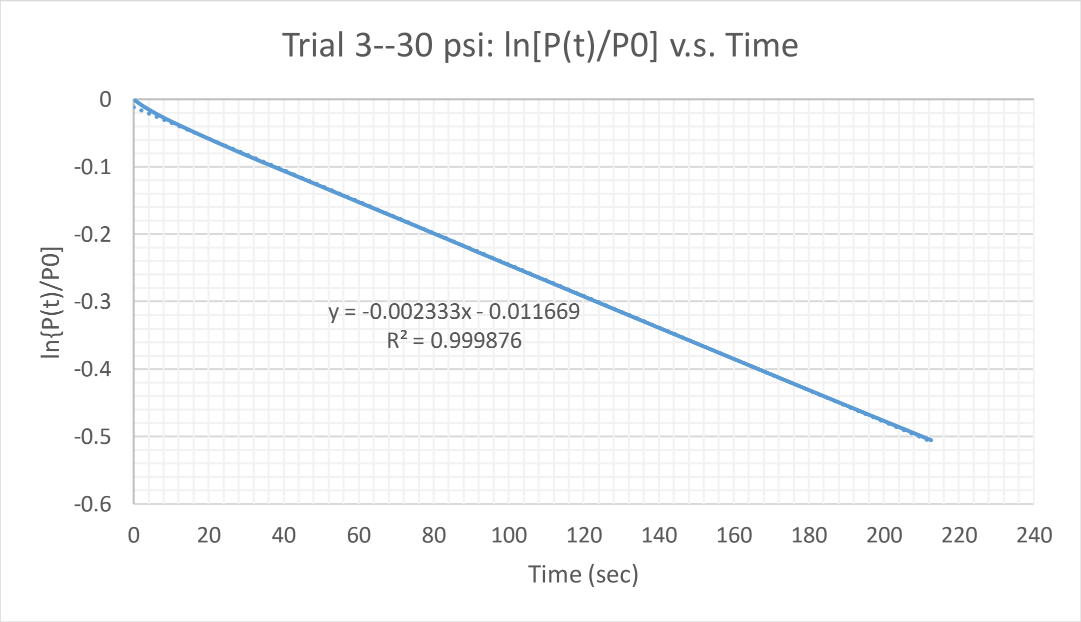

(a)

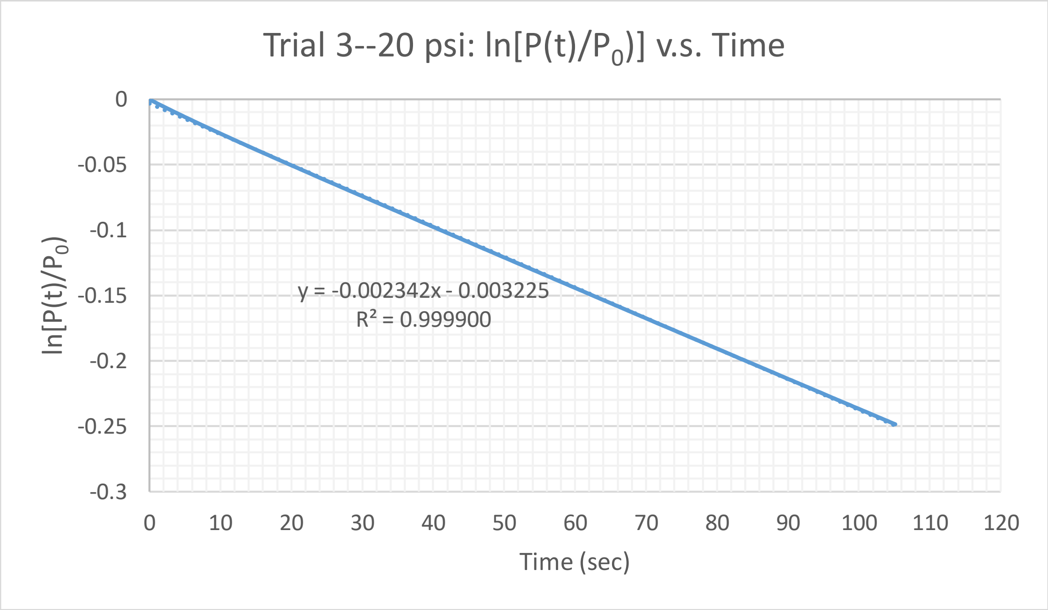
Trial 3--20 psi: ln[P(t)/P$_0$)] v.s. Time
ln[P(t)/P$_0$)
0
-0.05
-0.1
-0.15
-0.2
-0.25
-0.3
0
10
20
30
40
50
60
70
80
90
100
110
120
Time (sec)
y = -0.002342x - 0.003225
R² = 0.999900

(b)

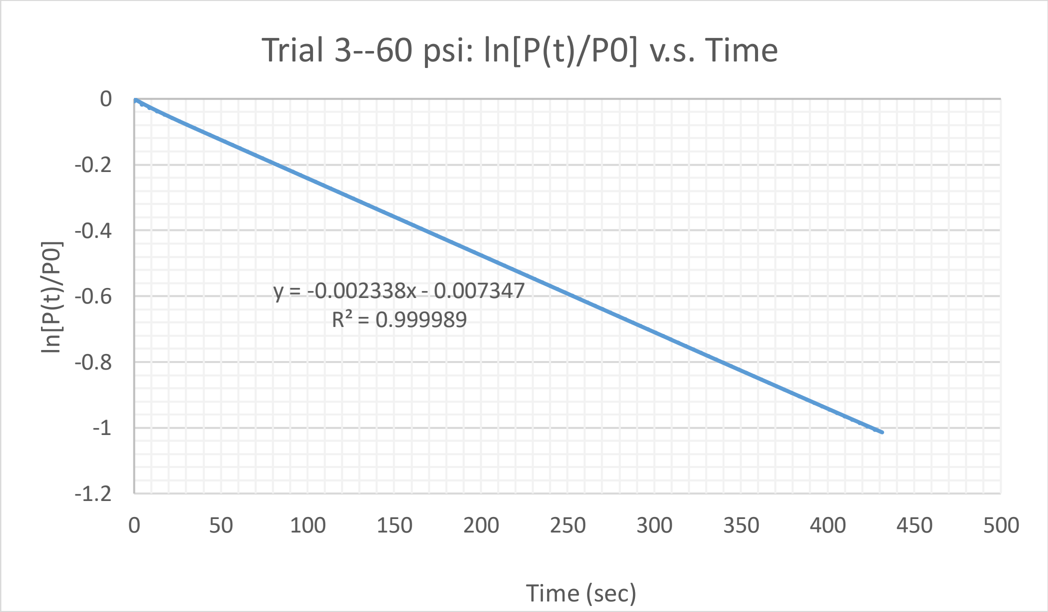
Trial 3--60 psi: ln[P(t)/P0] v.s. Time
ln[P(t)/P0]
0
-0.2
-0.4
-0.6
-0.8
-1
-1.2
0
50
100
150
200
250
300
350
400
450
500
Time (sec)
y = -0.002338x - 0.007347
R² = 0.999989

(c)

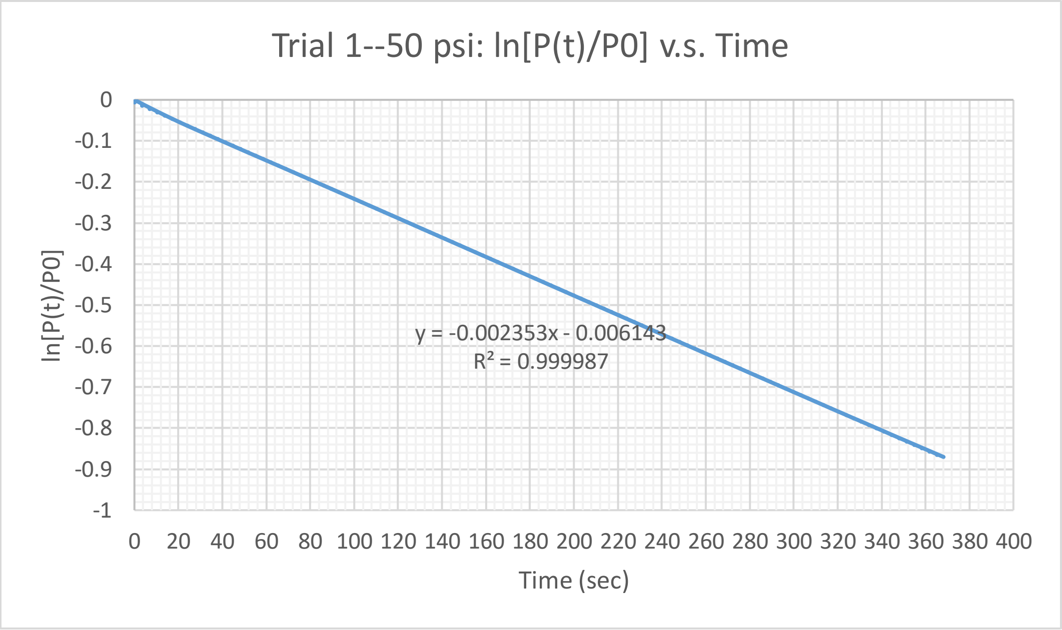

(d)

Figure 6-6: (a), (b), (c), (d): *All represent the titles given to each with the starting pressure for the shown trial listed after the trial number. The slopes of the best fit lines represent the experimental "k" values mentioned in the text above.*

After analyzing the data and creating the above plots, it was determined that the value of "K" as determined by the absolute value of the slope of the best fit line in the plots above and others like them agreed to within five percent of each other. Thus, knowing the size of the leak, the leak rate and drop in pressure may be calculated. Or conversely, by measuring the transient leak rate or pressure drop, the size of the leak can be estimated.

Thus, the conclusions that can be drawn from this portion of the work are that the mass flow rate out of the test pipe is in good agreement with the choked flow model and its assumptions. Furthermore, it has been demonstrated that the mass spectrometer is a viable method for detecting a leak from an underground pipe by placing the detection probe on the surface of the soil.

6.4 Gas Leak Detection and Diffusion Studies

The new wooden box, shown earlier in Figure 6-2, was used for all the following studies. The soil placed in the box was the same hand-mixed blend with sand, gravel, and top soil at a ratio of 1:1:2 respectively. This "typical" soil will lend itself nicely as a surrogate for common soils found in the field. The box was filled with about 18 inches of the soil blend with the test pipe located at the bottom of the soil layer. For the subsequent diffusion testing, the gas was switched from CO_2 to argon since the pure CO_2 was rapidly corroding the detector filaments in the mass spectrometer. Thus, argon was used in place of methane since in the laboratory methane represents an explosion hazard. However, the diffusion properties of argon are nearly identical to methane so the results found here can easily be extended to methane leaking from underground pipes. The experiments described in this section have two main objectives. The first is to verify that the mass spectrometer can indeed detect gas leaking underground as the gas diffuses through the soil and beaks through the surface. The second objective was to model the convective diffusion of the gas through the soil and fit it to a standard unsteady-state diffusion model. This fit will allow the determination of the dependence of the convective diffusivity of the gas through the soil with the leak rate and soil properties.

The experiment commenced by setting a constant flow of argon into the buried pipe with its accompanying simulated “leak”. The flow rate was carefully controlled by means of an Alicat mass flow controller. The box was sealed and the mass spectrometer’s probe was set directly at the surface of the soil layer. After starting the gas flow a period of time elapsed where no argon was detected at the surface. This time (called below the “dead time”) was the time required for the gas to enter the soil at the bottom of the box and diffuse through to the top of the soil. Once the argon “broke through” the soil bed, the mass spectrometer began to record the concentration of the gas as it emerged from the soil. This curve has a characteristic “s” shape that reflects the penetration and eventual saturation of the soil bed with the gas. The point of saturation is indicated when the experimental data level off at some constant value as shown below in Figure 6-7. The curves were then fit to a standard mathematical model to determine the value of the convective diffusion coefficient of the gas as it is being pushed “convectively” through the soil by the flow rate. The argon flow rate was varied between 1.5 and 2.0 liters/minute and the diffusion was monitored at the soil surface. An additional model was employed to represent the dependence of the convective diffusion coefficient with the flow rate of gas entering the soil. Good agreement was found between the data gathered here and the literature. The soil layer thickness was changed to 36 inches and an identical test was performed to evaluate the effect of bed thickness on the convective diffusivity.

6.4.1 *Data Analysis*

After collecting the argon concentration data from the mass spectrometer using the laboratory apparatus described previously, the data were exported to Excel^{TM}. The first step of the data analysis was to normalize the argon concentrations using Equation 6-5 where c(t) in ppm is the changing argon concentration with time, c_i is the initial argon concentration, and c_f is the final argon concentration.

$$Normalized\ Concentration = \frac{C(t)-C_i}{C_f-C_i} \qquad (6\text{-}5)$$

These normalized concentrations were used to identify the dead time of each trial. The dead time is characterized by several data points having normalized concentrations of zero at the start of the trial. This represents the time required for the argon to diffuse through the soil and initiate detection by the mass spectrometer. In most trials the experimental dead time was between 20 and 25 minutes. The dead time was subtracted from each trial to generate a "shifted time" such that all subsequent times have normalized concentrations greater than zero. The normalization of the argon concentration and removal of dead time allowed the system to be modeled using the complementary error function shown in Equation 6-6. Such an equation is the standard solution for the so-called transient penetration mass transfer model applicable here.

$$Fitted\ Normalized\ Concentration = 1 - \mathrm{erf}(\frac{H^2}{4Dt_s}) \qquad (6\text{-}6)$$

Here H is the thickness of the soil bed in cm and t_s in sec is the shifted run time from the data. D (cm^2/sec) is the effective diffusivity that describes how fast the argon will diffuse through the soil. It combines both free diffusivity due to Brownian motion and convective diffusivity due to the flow of argon "pushing" the gas through the bed. The fitting procedure uses the experimental transient concentration values with a known soil thickness to arrive at a value of D, the effective diffusivity. When deriving the fitted concentration values an initial estimate for the effective diffusivity (*D*) was applied. The value of D is changed until the "best fit" is obtained. To evaluate the best fit to the model, i.e., the difference between the actual normalized concentration and fitted normalized concentration values, a sum of squares calculation was used as defined in Equation 6-7 where ANC is the actual normalized concentration and FNC is the fitted normalized concentration with the estimated value of D. This difference represents the error between the fit and the data.

$$Difference = \sum(ANC - FNC)^2 \qquad (6\text{-}7)$$

To minimize the difference in Equation 6-7, Excel^{TM} solver was used to vary the effective diffusivity until the minimum difference between the data and the model was achieved. This procedure was followed for every trial to produce a set of effective diffusivities for each argon flowrate. These results were used to derive a fit for the results in the form of Equation 6-8 as described in the literature [37,38].

$$D = D_o + AV^n \qquad (6\text{-}8)$$

Here D is effective diffusivity, D_o is the free diffusivity through the soil bed, V is the argon flow rate in L/min, and *A* and *n* are fitted parameters. This equation describes how the effective diffusivity, D, changes with argon flow rate. Thus it captures the convective nature of the argon moving through the soil. Literature has suggested that the effective free diffusivity (D_o) is a function of the "free diffusion" coefficient of argon in the open air and the porosity of the soil bed. For the work here a value of D_o equal to 0.06 cm^2/sec was used when deriving the fit [39]. It should be noted that this value of D_o was arrived at by assuming a value of 0.4 for the porosity of the soil mix. Experimental values of D and V were inserted into Equation 6-8 and initial values for parameters *A* and *n* were provided. A fitted diffusivity was produced as the values of *A* and *n* were varied. A sum of squares approach was used once more to calculate the error between the model diffusivity and the experimental diffusivity. Excel solver was used to minimize this difference by changing the value of parameters *A* and *n*. In addition, a fit was also produced by fixing *n* to a value of 1 and only allowing *A* to be varied as suggested in the literature [38].

6.4.2 Results

The procedure to evaluate the effective diffusivity values from the data was the same for all trials. As a result, only a sample of the results for one trial will be highlighted in this section. Table 6-1 displays the results for trial 1 of the experiment with an argon flowrate of 1.50 L/min and a bed thickness of 18 inches.

Table 6-1: *Trial 1 of 1.50 L/min Argon flowrate with H = 18 inches of soil*

Time (min)	Concentration (ppm)	Normalized Concentration	Shifted Time (sec)	FNC*	Sum of Squares
0	80	0.000	-1500		
5	80	0.000	-1200		
10	77.5	-0.002	-900		
15	75	-0.004	-600		
20	70	-0.008	-300		
25	80	0.000	0		
30	95	0.012	300	0.000	0.0002
35	175	0.078	600	0.020	0.0033
40	275	0.160	900	0.121	0.0015
45	330	0.205	1200	0.245	0.0016
50	440	0.295	1500	0.352	0.0033
55	530	0.369	1800	0.438	0.0048
60	600	0.426	2100	0.506	0.0064
65	650	0.467	2400	0.561	0.0088
70	725	0.529	2700	0.605	0.0059
75	800	0.590	3000	0.642	0.0027
80	850	0.631	3300	0.672	0.0017
85	875	0.652	3600	0.698	0.0022
90	900	0.672	3900	0.721	0.0023
95	950	0.713	4200	0.740	0.0007
100	1000	0.754	4500	0.757	0.0000
105	1100	0.836	4800	0.771	0.0042
110	1150	0.877	5100	0.784	0.0086
115	1200	0.918	5400	0.796	0.0149
120	1200	0.918	5700	0.807	0.0124
125	1200	0.918	6000	0.816	0.0104
130	1250	0.959	6300	0.825	0.0180
135	1300	1.000	6600	0.833	0.0280
140	1300	1.000	6900	0.840	0.0257
145	1300	1.000	7200	0.846	0.0236
150	1300	1.000	7500	0.852	0.0218
				Total Sum	0.2130

*FNC = Fitted Normalized Concentration

The best fit for the diffusivity that resulted in the minimization of the total sum of squares in Table 6-1 was 0.53 cm^2/sec. The dead time in Table 6-1 was taken to be 25 minutes because that was the last point where the normalized concentration was less than 0. Figure 6-7 displays a plot comparing the experimental data and the derived fit. Good agreement between the fit and the model is found.

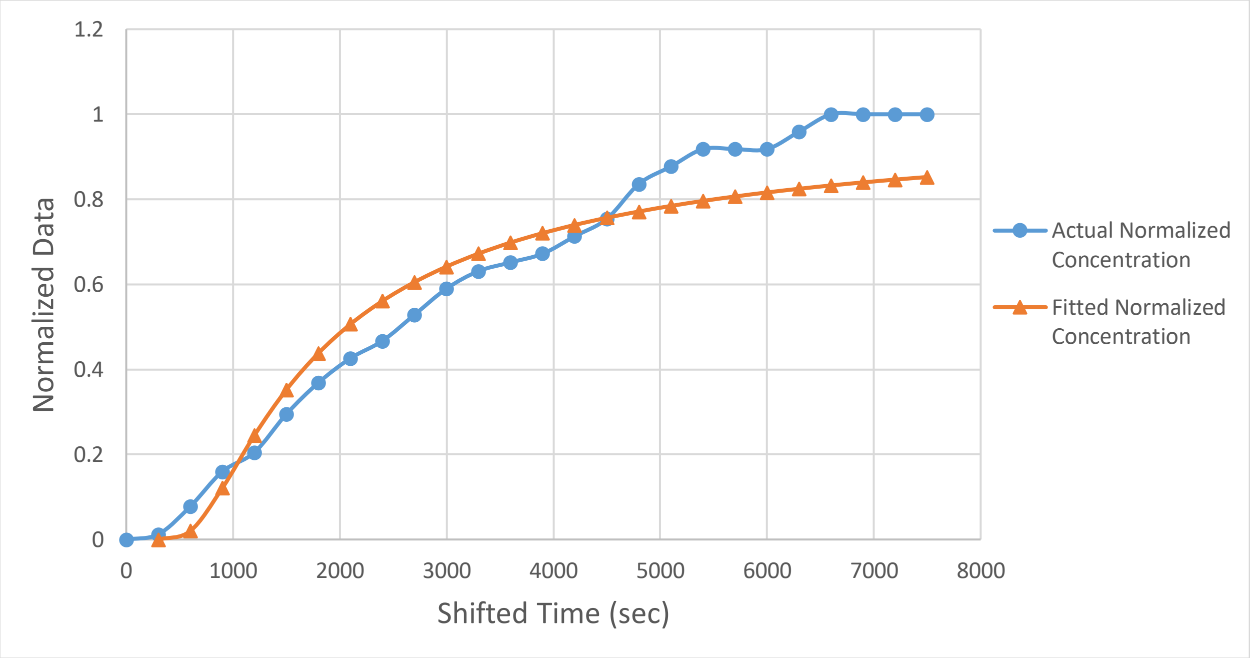

Figure 6-7: Actual and fitted normalized concentrations for trial 1 of 1.50 L/min Argon flowrate

Refer to the Appendix for tables of all remaining fits to the data and comparisons of the data and the fitted concentration values. Table 6-2 displays the calculated values of the effective argon diffusivities for all trials as a function of the argon flowrate.

***Table 6-2:** Effective Argon diffusivity as a function of flowrate*

Argon Flowrate (L/min)	Diffusivity (cm^2/sec)	Packing Height (in)
1.50	0.530	18
1.50	0.656	18
1.50	0.723	18
1.75	0.815	18
1.75	0.678	18
1.75	0.804	18
2.00	0.728	18
2.00	1.01	18
2.00	0.931	36

Table 6-2 demonstrates that as the argon flowrate increased, the effective diffusivity increased as expected. This is due to the increasing contribution of the convection of argon through the bed. The average effective diffusivity values as a function of argon flow rate are as follows: 0.636 cm^2/sec for 1.50 L/min, 0.766 cm^2/sec for 1.75 L/min, and 0.899 for 2.00 L/min. Table 6-2 also demonstrates that the effective diffusivity is not a function of bed thickness, H. The 36-inch packing height for the 2.00 L/min trial produced an effective diffusivity between the values for the 18-inch packing height. Using the results from Table 6-2, regression parameter values for A and n were found for Equation 6-8. Table 6-3 displays the parameter values that resulted in the minimization of the difference.

Table 6-3: *Fitted parameters for minimization of sum of squares*

Function Parameter	Value
D_o	0.06
A	0.347
n	1.26

The parameters shown in Table 6-3 yield Equation 6-9 which captures the effect of the convective nature of the movement of argon through the bed.

$$D = 0.06 + 0.347V^{1.26} \tag{6-9}$$

A graphical representation of the function from Equation 6-9 compared to the experimental data is shown in Figure 6-8. The standard error bars displayed in Figure 6-8 are equivalent to 1 standard derivation of the effective diffusivity for each tested flowrate. The 1.5 L/min argon flowrate had a standard deviation of 0.0802 cm^2/sec, 1.75 L/min argon flowrate had a standard deviation of 0.0622 cm^2/sec, and 2.0 L/min argon flowrate had a standard deviation of 0.118 cm^2/sec.

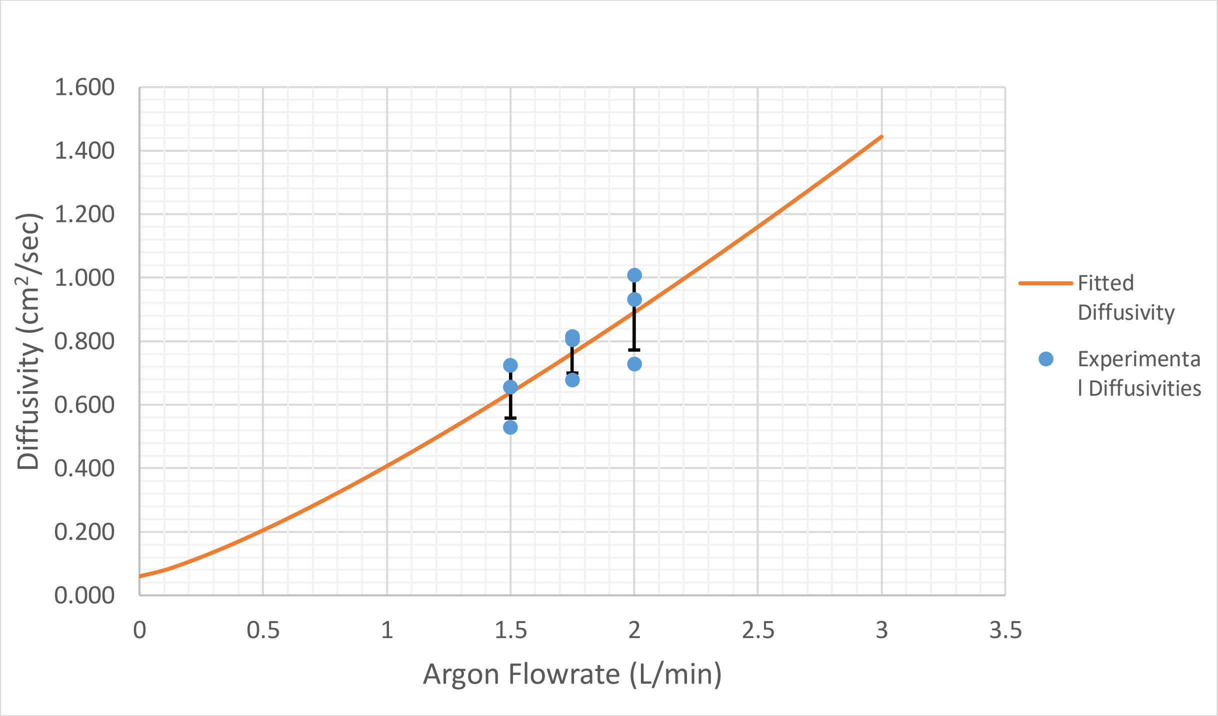

Figure 6-8: *Effective Argon diffusivity as a function of Argon flowrate*

Previous literature has suggested the value of parameter *n* should be approximately equal to 1 [38]. The value of *n* that resulted in the minimization of the sum of squares error between the experimental data and the model fit was 1.26. This deviation from 1 may be due to the argon flow rate being limited between 1.50 L/min and 2.00 L/min. If more data were present between 0 L/min and 1.50 L/min then the value of *n* may have been closer to the value suggested from literature.

If parameter *n* is fixed at a value of 1 to produce a linear fit, then the parameter values outlined in Table 6-4 will result in the minimization of the sum of squares error.

Table 6-4: *Minimized sum of squares with parameter n fixed*

Function Parameter	Value
D_o	0.06
A	0.403
n	1.00

The parameters shown in Table 6-4 form Equation 6-10 which represents the convective nature of the effective diffusivity as a function of argon flowrate.

$$D = 0.06 + 0.403V^{1.00} \tag{6-10}$$

A graphical representation of the function found in Equation 6-10 compared with the experimental data can be seen in Figure 6-9.

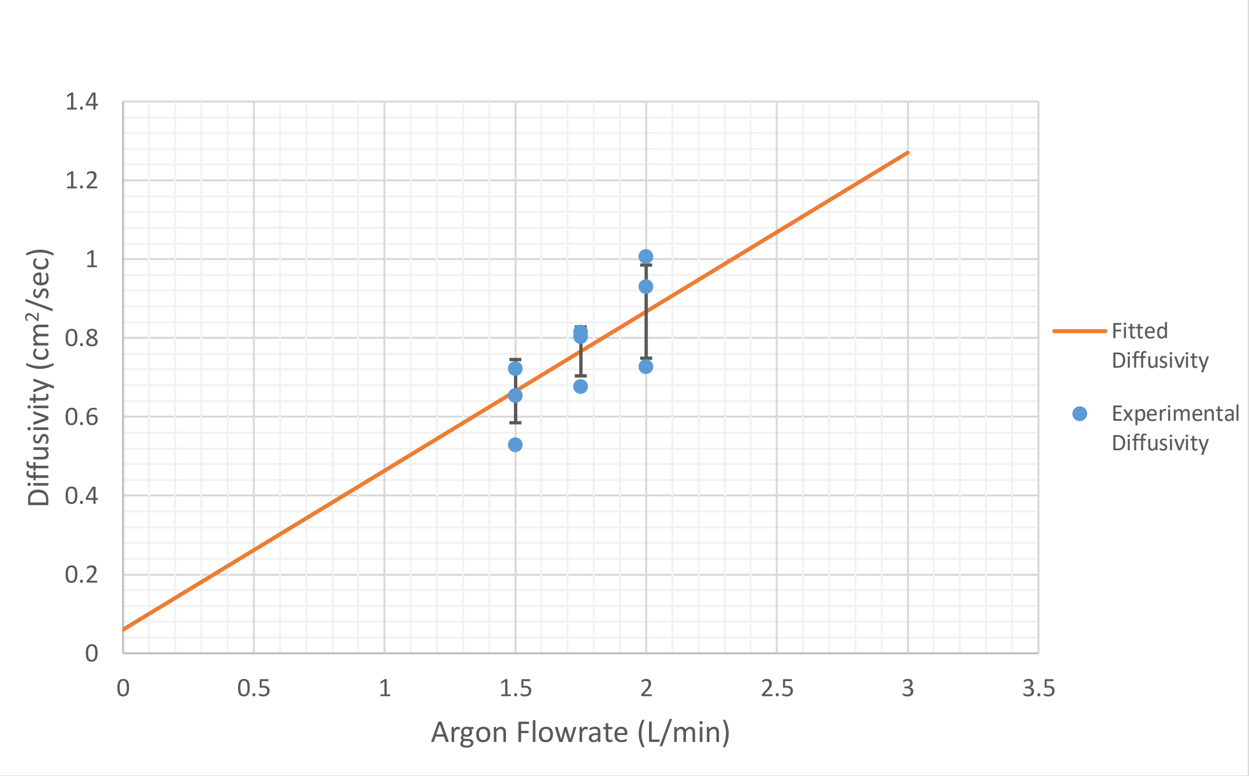

Figure 6-9: Effective Argon diffusivity as a function of flowrate with a linear model

The error bars in Figure 6-9 have the same values as the error bars in Figure 6-8 as they were derived from the same data set.

Both sets of parameter values presented in Tables 6-3 and 6-4 result in similar sum of squares errors around the experimental diffusivities. The parameters from Table 6-3 result in a sum of squares error of 0.0729. The parameters from Table 6-4 result in a sum of squares error of 0.0768. As a result, the derived fit is an accurate model of the experimental diffusivities and falls within experimental error regardless of the value of n. Furthermore, this supports the theory of modeling the system using the transient penetration theory and the complementary error function. Figure 6-10 overlays Figures 6-9 and 6-8 to highlight the differences between the fits.

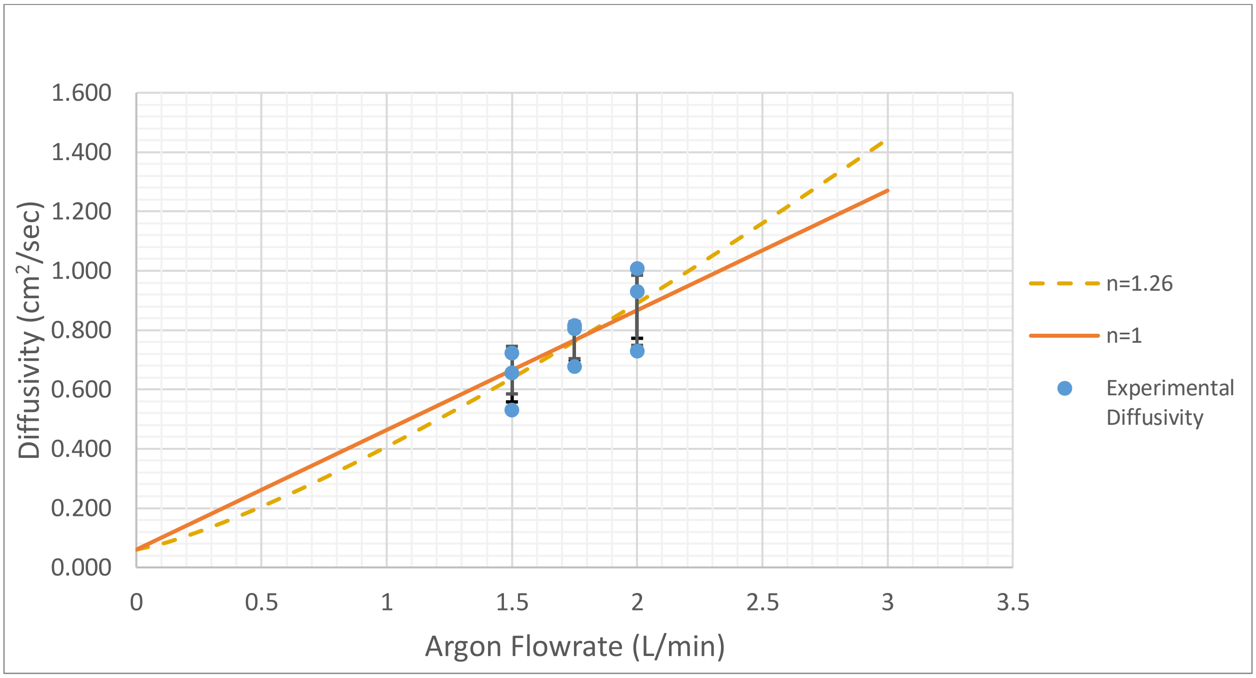

Figure 6-10: *Graphical representation of differences between fits for the experimental diffusivities and the Argon flowrate*

Figure 6-10 shows that between 1.5 L/min and 2.0 L/min, the range of argon flowrates used here, both fits model the experimental data quite well and provide similar effective diffusivity values within experimental error. Outside of this region the fits diverge from each other. This is especially significant as the argon flowrate approaches 3 L/min and beyond. If the flowrate continues to increase, then the fits will diverge from each other due to the differences in the value of parameter *n*. However, over the range of data in these experiments, the fitted models will adequately predict the diffusivity of the argon through the soil bed. Finally, it should be noted that argon and methane have nearly identical free diffusion coefficients (0.19 cm^2/sec for argon and 0.21 cm^2/sec for methane), hence the value of D_o should be the same for both gasses. So the model described by Equations 6-9 and 6-10 should work equally well for methane [40]. This is important for in the present study, argon was selected as the sample gas for safety reasons even though the focus of the work is on pipelines carrying natural gas in the field.

6.5 Conclusions

As a result of the work presented in this section, the following conclusions can be drawn:

1. The transient mass flow rate and pressure for a simulated leaking underground pipe can be accurately modeled by the choked flow analysis. Since gas pressures in typical methane pipelines are significantly higher than those used here, the choked flow assumption should work even better in the field.
2. If the pressure and size of the leak are known, the flow rate of gas through the leak can be determined.
3. If the flowrate and line pressure are known the size of the leak can be calculated.
4. The soil mix selected here for these experiments was a good surrogate for common soils with an experimentally determined porosity value of 0.4.
5. The mass spectrometer has been shown to be a useful tool in detecting and monitoring leaks in underground pipelines at the soil surface.
6. The transient penetration diffusion model proved to be a good fit for the convective diffusion of gas through the porous soil bed. The model yielded values for the convective diffusion coefficients of argon at different flow rates as the gas penetrated the soil from below.
7. The dependence of the convective diffusion coefficients on gas flowrate was determined and agreed with similar findings in the literature.

In closing it has been reported in the recent literature that researchers in Utah have developed a mass spectrometer on a chip the size of a postage stamp [41]. Hence it can be envisioned that such a device might be employed on a drone that, in conjunction with the ground penetrating radar, can locate pipelines in the field and simultaneously detect the presence of a leak underground. This would significantly enhance the feasibility of applying autonomous detection devices in the field [42].

7 BROADER IMPACTS

This project has made significant strides in the development of non-metallic Fiber Reinforced Polymer (FRP) composite pipes as possible replacement for steel pipes. The non-metallic FRP pipes are light-weight, possess high strength, and do not corrode in the buried environment. Strategies to detect such pipes using ground sensory technologies have also been successfully demonstrated.

The project work involved one Ph.D. student and several M.S. students who are now familiar with buried pipes, safe digging procedures, advanced composite technologies, etc. The Ph.D. student along with two M.S. students were lead participants in development and testing of composite pipes, buried pipe detection using Ground Penetrating Radar, and Gas Leak Detection using an advanced Mass Spectrometer. These three lead graduate students (research assistants) were assisted by several other M.S. level graduate students in the testing process, thus familiarizing them with the pipeline industry and related issues. One of the lead M.S. students (who focused on composite pipe development) already graduated in May 2018, and the lead Ph.D. student (who focused on Ground Penetrating Radar) is expected to graduate in December 2018. At least one other M.S. student will graduate within the next 12 months.

One Ph.D. and one M.S. student attended the research forum held in Baltimore, MD during September 11-12, 2018. The students presented two posters showcasing their research work. Both students interacted with several industry participants and learnt the issues and challenges facing the pipeline industry.

Internal pressure testing of GFRP pipes showed that current designs of FRP composite pipes are providing burst pressures up to 5,200 psi and FRP joints can take pressures up to 2,800 psi. This project work (coupled with a preceding study) has shown that buried FRP pipes can be detected using Ground Penetrating Radar up to 4’ below ground, provided that the pipe surface has a reflector such as carbon fabric strip or aluminum tape glued to it. For GFRP pipes, carbon fabric is the preferred surface material. Additionally, gas leak detection experiments coupled with spectral analysis revealed small leaks of gas after capturing and analyzing air samples around a pipe.

In addition to making significant strides in advancing the technology related to manufacturing high pressure FRP pipes and joints and their detection using ground sensory technologies, this USDOT-PHMSA funded research project has been immensely useful in training a number of graduate students, make them appreciate the requirements of the pipeline industry, raise awareness in the area of pipeline safety, and help them prepare for future work in pipeline related areas.

8 CONCLUSIONS

Literature review at the start of the project revealed a significant need in natural gas pipelines for new structural materials, with better strength, strength to weight ratio, and resistance to corrosion than steel. These materials need to be able to withstand stresses induced by operating pressures near 1,500 psi, for pipelines ranging from 10 inches to 48 inches in diameter. One such material that could meet this need is glass fiber reinforced polymer composite (FRP).

The purpose of this project was to investigate methods through which GFRP pipe behavior could be evaluated and predicted. This was done through the completion of several key objectives:

- Design and fabrication of a high strength burst pressure test frame
- Hydrostatic burst pressure testing of GFRP pultruded and filament wound pipes of 6 inch and 10 inch diameters
- Hydrostatic burst pressure testing of thin wall filament wound pipes to 3,000 psi
- Hydrostatic burst pressure testing of thick wall filament wound pipes to 5,200 psi
- Hydrostatic burst pressure testing of GFRP butt joints to 1,000 psi
- Split ring apparent hoop tensile strength testing of filament wound rings
- Development of elastic stress/strain predictions using Classical Lamination theory
- Analysis and comparison of experimental results and theoretical predictions.

Hydrostatic burst pressure testing was conducted to determine elastic behavior, failure progression, and failure strengths of 6 inch and 10 inch diameter pipes. These pipes (thin wall) failed at internal pressures as high as 3,000 psi, suggesting that these pipes could operate at pressures near 500 psi. Split ring testing was conducted as a possible alternative to hydrostatic pressure testing. The results were found to be relatively accurate in the elastic zone (within 25 percent) and inaccurate in terms of failure prediction (50 percent error).

Lamination theory was used as an analytical method to predict elastic behavior for these pipes. The theory was computationally rigorous and time consuming, but was found to accurately predict (within 25 percent) behavior in the elastic region (10 to 30 percent of ultimate stress). While the split ring test and CLT prediction perform reasonably in the elastic zone, burst pressure testing appears to be the quickest and most accurate way to evaluate pipe behavior. Split ring testing methodology needs to be modified if accurate results are to be produced and CLT is not a practical tool for design engineers. Furthermore, CLT does not sufficiently model failure progression or failure strength, unless paired with failure criteria. Nonetheless, this research has opened up opportunity for meaningful future investigation of GFRP pipes and joints. A few suggested topics are provided below.

This study demonstrated the success in detecting buried FRP composite pipes using Ground Penetrating Radar (GPR) for 2 feet depth. Coupled with a previous study, GPR has been shown to detect FRP composite and PVC pipes with burial depth up to 4 feet deep. While GPR could detect GFRP pipes with a weak signal, the GFRP pipe detection was significantly enhanced by bonding CFRP or aluminum strip or rings on the surface of the pipes. The study also showed that 200 MHz radar antenna was very successful in detecting buried pipes while the smaller 400 MHz antenna was not very successful.

The study also demonstrated the detection of gas leakage from buried pipes using mass spectroscopy.

9 REFERENCES

1. Future Pipe Industries' Handbook, "Fiberglass Technical Overview and Design Aspects, pp. 120-130.
2. "Life Management Methodology Development for Fiber Reinforced Hydrogen Pipelines," SRNL & ASME, 2008.
3. "Hydrogen Piping and Pipelines," ASME, 2008.
4. http://www.phmsa.dot.gov
5. wtsb.gov/doclib/reports/2011/PAR1101.pdf
6. Fiberspar™XT spoolable pipeline, National oil well Varco.
7. GangaRao, H., "Introduction of FRP composites in civil engineering," in Int. ***Handbook of FRP Composites in CE***, edited by M. Zoghi. ***Taylor & Francis***. Book: 2013, pp. 3-13.
8. Liang, R. and GangaRao, H., "Fiber-reinforced polymer (FRP) composites in environmental engineering applications," in ***Developments in Fiber-Reinforced Polymer (FRP) Composites for Civil Engineering***," edited by N. Uddin. ***Woodhead Publishing***. Book: 2013, pp. 410-468.
9. GangaRao, H. V. S., "Infrastructure applications of fiber-reinforced polymer composites," in ***Applied Plastics Eng Handbook***, edited by M. Kutz. ***Elsevier***. Book: 2011, pp. 565-584.
10. Qureshi, M.A.M. and GangaRao, H. V. S., "Torsional response of closed FRP composite sections (includes pipes)," **Composites: Part B**. 61: 2014, pp. 254-266.
11. Dispennette, D. W., Skidmore, M., and *GangaRao, H. V. S.*, "Bending Behavior of Pultruded Glass FRP Poles and Pipes," ***Proc. of ICERP 2013***, April, 2013, Mumbai, India.
12. Dispennette, D., Dittenber, D. B., and GangaRao, H. V. S., "Behavior of Pultruded Large Diameter Thin-Walled Orthotropic Cylindrical Tubes," ***Proc. of SAMPE 2012***, Baltimore, MD.
13. Losset, M., GangaRao, H. V. S., Liang, R. et al., "Development of a Manufacturing and Assembly Technology for Low Cost Pultruded Composites," ***ShipTech 2012: Affordability, Sustainability & Technology***, February 14-15, 2012, Orlando, FL.
14. Rawls, G., "Codification of Fiber Reinforced Composite Piping," Technical Report No. SRNL-STI-2012-00634 submitted to U.S. Department of Energy (USDOE) under Contract No. DE-AC09-08SR22470, October 2012.
15. Estep, D., GangaRao, H. V. S., and Dittenber, D., "Response of Pultruded Glass Composite Box Beams under Bending and Shear,"***Journal of Composites: Part B***, 2016, pp. 150-161.
16. GangaRao, H. V. S. and Liang, R., "Creep (stress) Response Characterization and Life Prediction…," ***Proceedings from Global Innovations in Infrastructure with Advanced Composites***, ISBN 978-7-112-17353, 2014.

17. Vadlamani, D., “Strain Energy Density Based Failure Criterion for GFRP Coupons under Tension and Bending,” M.S. Thesis, West Virginia University, Morgantown, WV, 2007.
18. GangaRao, H.V.S. and Faza, S., “Bending and Bond Behavior of Concrete Beams Reinforced with Plastic Rebars,” ***Transportation Research Reviews 1290***, V. 2, 155-173.
19. Rawls, G. and Adams, T., “Fiber Reinforced Composite Pipelines,” ***SRNL***, June 2014.
20. ANSI/AWWA C950, “Std for Fiberglass Pressure Pipes,” ***AWWA***, Denver, CO, 1995.
21. GangaRao, H. V. S. and Dittenber, D., “Evaluation of a Life Prediction Model and Environmental Effects of Fatigue for GFRP materials,” ***Structural Engineering International***, ***IABSE***, 2010 (4), pp. 379-384.
22. Dietsch, B.J., Densmore, B.K., and Strauch, K.R., Hydrographic Surveys at Selected Highway Bridges Crossing the Missouri River using a Multibeam Echosounder, 2011: U.S. Geological Survey Scientific Investigations Report 2014-5062, 2014, 53 p.
23. GangaRao, H. V. S., Narendra, T., and Vijay, P.V., Reinforced Concrete Design with FRP Composites, Taylor Francis Inc, United States, 2007.
24. ASCE-LRFD, Pre-Standard for Load & Resistance Factor Design (LRFD) of Pultruded Fiber Reinforced Polymer (FRP) Structures (Draft), ASCE, November, 2010.
25. Hearn, E., *Mechanics of Materials 1: An Introduction to Mechanics of Elastic and Plastic Deformation of Solid and Strucutral Materials.* Woburn, MA: Butterworth-Heinemann, 1997.
26. Xia, M., Takayangagi, H., and Kemmochi, K., “Analysis of Multi-Layered Filament-Wound Composite Pipes Under Internal Pressure.” *Composite Structures*, 2001.
27. ASME. (2015). Section X: Fiber Reinforced Plastic Pressure Vessels. In ASME, *ASME Boiler and Pressure Vessel Code.* New York, NY, 2015.
28. Barbero, E. J. *Introduction to Composite Materials Design.* Philadelphia, PA: Taylor & Francis Inc., 1998
29. Kuo-Shih, L., & Tsai, S. W., “A Progressive Quadratic Failure Criterion for a Laminate.” *Composites Science and Technology*, 1996, 1023-2031.
30. Roy, A. K., & Tsai, S. W., Pressure Vessels. In S. W. Tsai, *Composites Design.* Dayton, OH: Think Composites, 1988.
31. Kassapoglou, C., *Design and Analysis of Composite Structures with Applications to Aerospace Structures.* Chichester,UK: John Wiley and Sons Ltd., 2010.
32. Guo, B., & Ghalambor, A.. *Natural Gas Engineering Handbook (2nd Edition).* Houston, Tx: Gulf Publishing Company, 2012.
33. Boresi, A. P., and Schmidt, R. J. *Advanced Mechanics of Materials, Sixth Edition.* New Delhi: John Wiley and Sons Inc., 2005.

34. Knight, N. F., Factors Influencing Progressive Failure Analysis Predictions for Laminated Composite Structure. Chantilly, VA: American Institute of Aeronautics and Astronautics, 2008.

35. Halabe, U. B., GangaRao, H. V. S., Zondlo, J., Kavi, J., Imes, B., and Cvetnick, A. (2017). *Advancement in the Area of Intrinsically Locatable Plastic Materials*, Final Report submitted to USDOT-PHMSA. Contract No. DTPH5615HCAP09. Available from https://primis.phmsa.dot.gov/matrix/FilGet.rdm?fil=11715&s=CAC8CF221D2143B2ABB6524C05BF6D25

36. Kavi, J., "Detection of Buried Non-Metallic (Plastic and FRP Composite) Pipes Using GPR and IRT," Ph.D. Dissertation, Department of Civil and Environmental Engineering, West Virginia University, Morgantown WV, 2018.

37. Crowl, D. A., and Louvar, J. F., *Chemical Process Safety: Fundamentals with Applications, 3rd Edition*. 3rd ed. N.p.: Prentice Hall, 2011.

38. Perkins, T K, and Johnston, O. C., "A Review of Diffusion and Dispersion in Porous Media," *Society of Petroleum Engineers Journal*, March 1963, pp. 70–84.

39. Troeh, F. R., Jabro, J. D., and Kirkham, D., "Gaseous Diffusion Equations for Porous Materials." *Geoderma*, vol. 27, 1982, pp. 239–253.

40. Engineering ToolBox, (2018). *Air - Diffusion Coefficients of Gases in Excess of Air*. [online] Available at: https://www.engineeringtoolbox.com/air-diffusion-coefficient-gas-mixture-temperature-d_2010.html [Accessed 05 August 2018]

41. Tian, Y., Decker, T. K., McClellan, J. S., Bennett, L., Li, A., De la Cruz, A., Andrews, D., Lammert, S. A., Hawkins, A. R., and Austin, D. E., "Improved Miniaturized Linear Ion Trap Mass Spectrometer Using Lithographically Patterned Plates and Tapered Ejection Slit." *American Society for Mass Spectrometry*, vol. 29, no. 2, 23 Aug. 2017, pp. 213–222., doi:10.1007/s13361-017-1759-z.

42. Kolb, C. E, Herndon, S. C., McManus, J. B., Shorter, J. H., Zahniser, M. S., Nelson, D. D., Jayne, J. T., Canagaratna, M. R., and Worsnop, D. R., "Mobile Laboratory with Rapid Response Instruments for Real-Time Measurements of Urban and Regional Trace Gas and Particulate Distributions and Emission Source Characteristics," *Environmental Science & Technology*, vol. 38, no. 21, 22 Sept. 2004, pp. 5694–5703., doi:10.1021/es030718p.

APPENDIX A – Classical Lamination Theory

A.1 Coordinate Systems

A brief explanation of classical lamination theory is provided in this section. Two different coordinate systems, the global coordinate(X, Y, Z) system and the fiber coordinate system (1, 2, Z) are employed in this theory. This consideration is important because fiber orientation does not always align with the global orientation of an FRP member. **Figure A-1** shows a common coordinate system for FRP laminae. However, this system is not universally accepted. Some organizations define the fiber direction as the XYZ system and the global system as the 12Z system. For example, the ASME Boiler and Pressure vessel code follows this alternative coordinate system. However, most authors define the coordinate systems in accordance with the figure below.

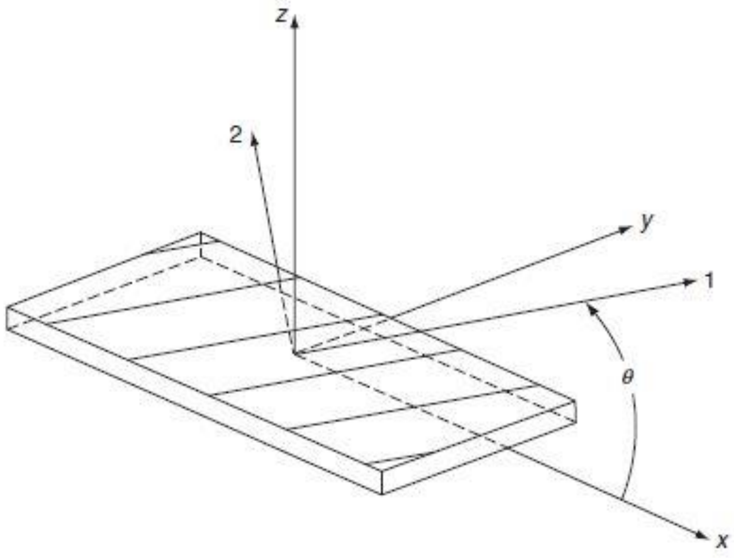

Figure A-1: *Lamina Coordinate System*

A.2 Stiffness Matrices

A.2.1 Specially Orthotropic Lamina

The first step in the classical lamination theory is to determine the stiffness matrix for a unidirectional lamina. Therefore, the five elastic constants must be determined. There are many equations, mechanics based and empirical, that aid in this process. The equations provided in this section were determined to be the most appropriate for this particular research.

A. Longitudinal Modulus of Elasticity

$$E_{11} = E_f * V_f + E_m * (1 - V_f) \qquad \text{(A-1)}$$

Where:

E_{11}= Modulus of Elasticity of the lamina in the fiber direction

E_f= Modulus of Elasticity in the fiber direction

V_f= Fiber volume fraction

E_m=Modulus of elasticity of the matrix

B. Transverse Modulus of Elasticity

$$E_{22} = E_m * \frac{1 + \zeta * \eta * V_f}{1 - \eta * V_f} \qquad \text{(A-2)}$$

Where:

E_{22}= Modulus of Elasticity of the lamina transverse to the fiber direction

ζ= empirical parameter for curve fit of experimental data= 2 for circular fibers

η= $(E_f/E_m-1)/(E_f/E_m+\zeta)$

C. Major Poisson Ratio

$$\nu_{12} = \nu_f * V_f + \nu_m * (1 - V_f) \qquad \text{(A-3)}$$

Where:

$\nu_{12=}$ Major Poisson ratio of the lamina

ν_f= Poisson Ratio of the fibers

ν_m= Poisson Ratio of the matrix

D. Minor Poisson Ratio

$$\nu_{21} = \frac{E_{22}}{E_{11}} * \nu_{12} \tag{A-4}$$

Where:

ν_{21}= Major Poisson Ratio of the lamina

E. Shear Modulus

$$G_{12} = \left[\frac{\left(1 + V_f\right) + \left(1 - V_f\right) * {}^{G_m}\!/_{G_f}}{\left(1 - V_f\right) + \left(1 + V_f\right) * {}^{G_m}\!/_{G_f}}\right] \tag{A-5}$$

Where:

G_{12}= Shear Modulus of the lamina

$G_{f=}$ Shear Modulus of the fibers

G_m= Shear Modulus of the matrix

A.2.2 Unidirectional Lamina

Based on these terms, generalized Hooke's law gives the equation for the stiffness matrix of unidirectional, specially orthotropic lamina. The stiffness terms in this matrix apply to the fiber coordinate system. Therefore, strains along the length of the fiber and transverse to the fibers can be determined for a unidirectional lamina.

$$\begin{Bmatrix} \epsilon_{11} \\ \epsilon_{22} \\ \gamma_{12} \end{Bmatrix} = [Q] * \begin{Bmatrix} \sigma_{11} \\ \sigma_{11} \\ \tau_{12} \end{Bmatrix} = \begin{bmatrix} Q_{11} & Q_{12} & 0 \\ Q_{21} & Q_{22} & 0 \\ 0 & 0 & Q_{66} \end{bmatrix} * \begin{Bmatrix} \sigma_{11} \\ \sigma_{11} \\ \tau_{12} \end{Bmatrix} \tag{A-6}$$

Where:

$Q_{11} = E_{11}/(1 - \nu_{12} * \nu_{21})$

$Q_{22} = E_{22}/(1 - \nu_{12} * \nu_{21})$

$$Q_{12} = Q_{21} = \frac{E_{22} * \nu_{12}}{(1 - \nu_{12} * \nu_{21})} = \frac{E_{11} * \nu_{21}}{(1 - \nu_{12} * \nu_{21})}$$

$$Q_{66} = 1/G_{12}$$

A.2.3 Transformed Unidirectional Lamina

Once the stiffness matrix for a specially orthotropic lamina is determined, the stiffness properties can be transformed to the out-of plane (global XYZ) coordinate system. This is done through the transformation matrix (T) and the angle of rotation (Θ).

$$[T] = \begin{bmatrix} Cos^2(\theta) & Sin^2(\theta) & 2 * Sin(\theta) * Cos(\theta \\ Sin^2(\theta) & Cos^2(\theta) & -2 * Sin(\theta) * Cos(\theta \\ -Sin(\theta) * Cos(\theta) & Sin(\theta) * Cos(\theta) & Cos^2(\theta) - Cos^2(\theta) \end{bmatrix} \tag{A-7}$$

The transformed stiffness matrix for a lamina is given by

$$\bar{Q} = \begin{bmatrix} \bar{Q}_{11} & \bar{Q}_{12} & \bar{Q}_{16} \\ \bar{Q}_{12} & \bar{Q}_{26} & \bar{Q}_{26} \\ \bar{Q}_{16} & \bar{Q}_{26} & \bar{Q}_{66} \end{bmatrix} = [T]^T * [Q] * [T] \tag{A-8}$$

A.2.4 Stiffness Matrix of Chopped Strand Mats

In addition to filament wound unidirectional fibers, many composite pipes also contain mats comprised of small strands of chopped fiber. Depending on the densities and volume content, mats can contribute a significant amount of stiffness. Since mats are composed of randomly oriented chopped strands, the stiffness can be approximated by the stiffness matrix for isotropic materials. Where E, ν, and G are given by:

A. Modulus of Elasticity of CSM

$$E = {}^{3}/_{8} * E_{11} + {}^{5}/_{8} * E_{22} \tag{A-9}$$

B. Shear Modulus of Elasticity of CSM

$$G = {}^{1}/_{8} * E_{11} + {}^{1}/_{4} * E_{22} \tag{A-10}$$

C. Poisson Ratio of CSM

$$\nu = \frac{E}{2 * G} - 1 \tag{A-11}$$

D. Stiffness Matrix of CSM

$$[Q] = \begin{bmatrix} 1/E & -\nu/E & 0 \\ -\nu/E & 1/E & 0 \\ 0 & 0 & 1/G \end{bmatrix} \tag{A-12}$$

A.2.5 ABD Stiffness Matrix

In the laminate, the individual laminae are stacked and identified in accordance with the figure below. This stacking sequence can be applied to laminates of n number of layers.

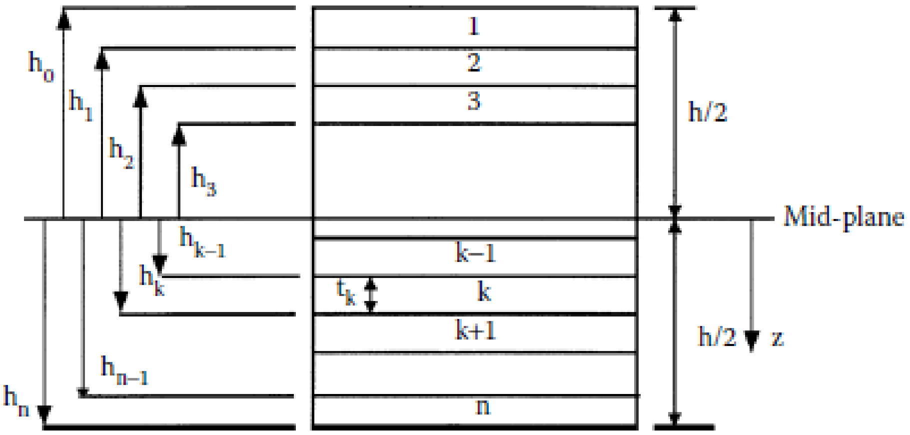

Figure A-2: *Laminate Layup*

The ABD stiffness matrix is determined so that a composite laminate may be analyzed for stresses and strains in the global directions. Therefore, the effects of the individual laminae must be compiled into a single matrix. The ABD matrix is assembled from the in-plane stiffness matrix ([A]), the coupling matrix ([B]), and the bending matrix ([D]). These are assembled in accordance with the laminate geometry and A, B, D matrix equations.

$$A_{ij=}\sum_{k=1}^{N}(\bar{Q}_{ij})_k * (Z_k - Z_{k-1}) \tag{A-13}$$

$$B_{ij=}\frac{1}{2}\sum_{k=1}^{N}(\bar{Q}_{ij})_k * (Z_k^2 - Z_{k-1}^2) \tag{A-14}$$

$$D_{ij=}\frac{1}{3}\sum_{k=1}^{N}(\bar{Q}_{ij})_k * (Z_k^3 - Z_{k-1}^3) \tag{A-15}$$

APPENDIX B – Gas Leak Detection Trials

Table B-1: *Trial 2 of 1.50 L/min Argon Flowrate with H=18 inches of soil*

Time (min)	Concentration (ppm)	Normalized Concentration	Shifted Time (sec)	FNC*	Sum of Squares
0	100	-0.006	-1500		
5	90	-0.011	-1200		
10	85	-0.014	-900		
15	90	-0.011	-600		
20	95	-0.008	-300		
25	110	0.000	0		
30	200	0.050	300	0.000	0.0025
35	325	0.120	600	0.060	0.0036
40	450	0.190	900	0.210	0.0004
45	600	0.274	1200	0.348	0.0055
50	740	0.352	1500	0.452	0.0101
55	850	0.413	1800	0.531	0.0139
60	950	0.469	2100	0.591	0.0149
65	1050	0.525	2400	0.639	0.0129
70	1200	0.609	2700	0.676	0.0045
75	1400	0.721	3000	0.707	0.0002
80	1500	0.777	3300	0.733	0.0019
85	1500	0.777	3600	0.754	0.0005
90	1550	0.804	3900	0.773	0.0010
95	1600	0.832	4200	0.788	0.0019
100	1700	0.888	4500	0.802	0.0074
105	1750	0.916	4800	0.814	0.0104
110	1750	0.916	5100	0.825	0.0083
115	1800	0.944	5400	0.835	0.0120
120	1850	0.972	5700	0.843	0.0166
125	1850	0.972	6000	0.851	0.0147
130	1900	1.000	6300	0.858	0.0202
135	1900	1.000	6600	0.864	0.0184
140	1900	1.000	6900	0.870	0.0168
145	1900	1.000	7200	0.876	0.0155
150	1900	1.000	7500	0.881	0.0143
				Total Sum	0.228

*FNC = Fitted Normalized Concentration

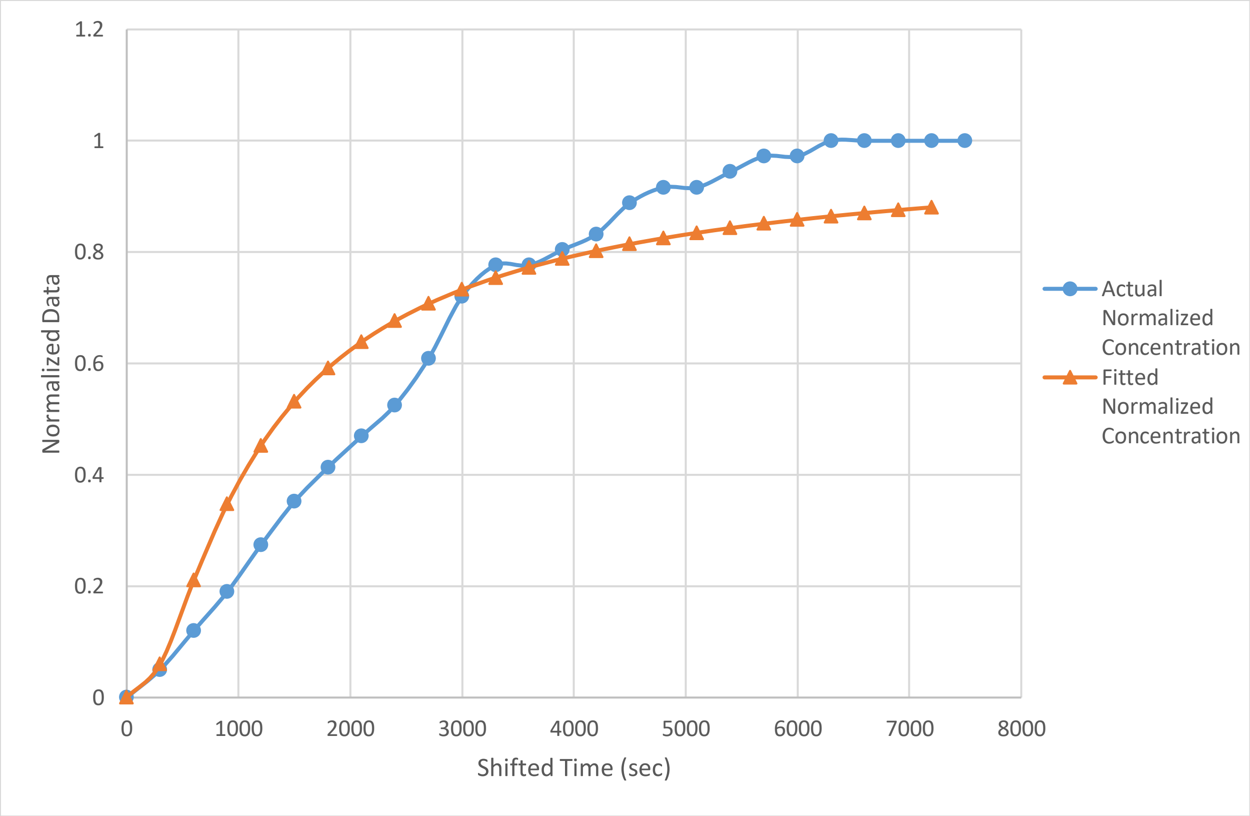

Figure B-1: *Trial 2 of 1.50 L/min Argon Flowrate with H=18 inches of soil*

Table B-2: *Trial 3 of 1.50 L/min Argon Flowrate with H = 18 inches of soil*

Time (min)	Concentration (ppm)	Normalized Concentration	Shifted Time (sec)	FNC*	Sum of Squares
0	105	-0.003	-1200		
5	105	-0.003	-900		
10	105	-0.003	-600		
15	105	-0.003	-300		
20	110	0.000	0	-	
25	175	0.035	300	0.001	0.0012
30	275	0.088	600	0.089	0.0000
35	440	0.177	900	0.256	0.0063
40	630	0.279	1200	0.394	0.0134
45	805	0.373	1500	0.496	0.0151
50	950	0.450	1800	0.570	0.0144
55	1100	0.531	2100	0.627	0.0092
60	1350	0.665	2400	0.670	0.0000
65	1400	0.692	2700	0.705	0.0002
70	1500	0.745	3000	0.733	0.0001

75	1600	0.799	3300	0.757	0.0018
80	1700	0.853	3600	0.777	0.0058
85	1750	0.879	3900	0.793	0.0074
90	1750	0.879	4200	0.808	0.0051
95	1800	0.906	4500	0.820	0.0074
100	1850	0.933	4800	0.831	0.0103
105	1900	0.960	5100	0.841	0.0141
110	1900	0.960	5400	0.850	0.0121
115	1900	0.960	5700	0.858	0.0104
120	1900	0.960	6000	0.865	0.0090
125	1950	0.987	6300	0.871	0.0133
130	1950	0.987	6600	0.877	0.0120
135	1950	0.987	6900	0.882	0.0109
140	1975	1.000	7200	0.887	0.0127
145	1975	1.000	7500	0.892	0.0117
150	1975	1.000	7800	0.896	0.0109
				Total Sum	0.215

*FNC = Fitted Normalized Concentration

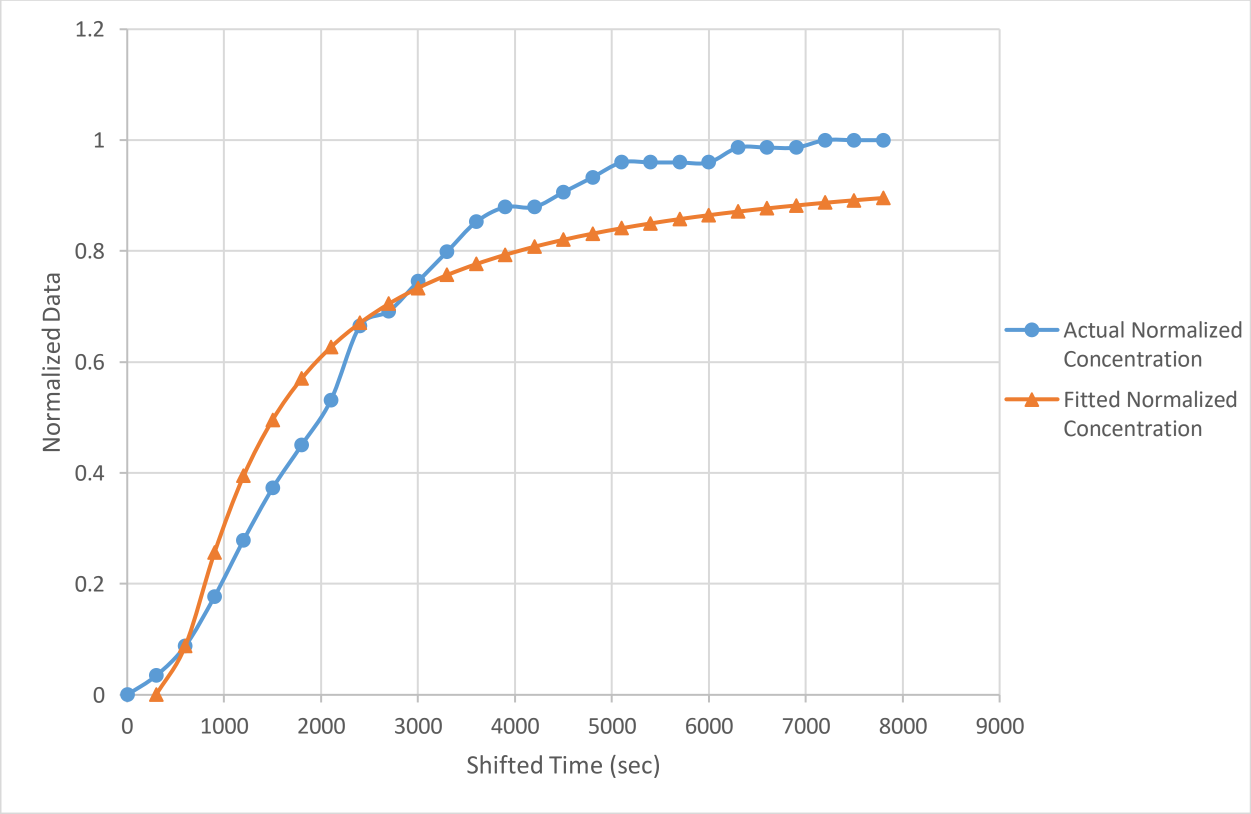

Figure B-2: *Trial 3 of 1.50 L/min Argon Flowrate with H = 18 inches of soil*

***Table B-3:** Trial 1 of 1.75 L/min Argon Flowrate with H=18 inches of soil*

Time (min)	Concentration (ppm)	Normalized Concentration	Shifted Time (sec)	FNC*	Sum of Squares
0	160	0.005	-1500		
5	150	0.000	-1200		
10	130	-0.010	-900		
15	125	-0.013	-600		
20	130	-0.010	-300		
25	150	0.000	0		
30	260	0.055	300	0.003	0.00276
35	410	0.130	600	0.131	0.00000
40	625	0.238	900	0.314	0.00581
45	800	0.325	1200	0.450	0.01560
50	1000	0.425	1500	0.546	0.01453
55	1200	0.525	1800	0.614	0.00800
60	1350	0.600	2100	0.666	0.00435
65	1500	0.675	2400	0.706	0.00094
70	1700	0.775	2700	0.737	0.00144
75	1800	0.825	3000	0.762	0.00391
80	1900	0.875	3300	0.784	0.00837
85	1900	0.875	3600	0.801	0.00545
90	1950	0.900	3900	0.816	0.00703
95	1975	0.913	4200	0.829	0.00696
100	2000	0.925	4500	0.840	0.00717
105	2000	0.925	4800	0.850	0.00560
110	2000	0.925	5100	0.859	0.00437
115	2050	0.950	5400	0.867	0.00695
120	2050	0.950	5700	0.874	0.00583
125	2100	0.975	6000	0.880	0.00905
130	2100	0.975	6300	0.886	0.00800
135	2100	0.975	6600	0.891	0.00710
140	2150	1.000	6900	0.895	0.01093
145	2150	1.000	7200	0.900	0.01004
150	2150	1.000	7500	0.904	0.00926
				Total Sum	0.169

*FNC = Fitted Normalized Concentration

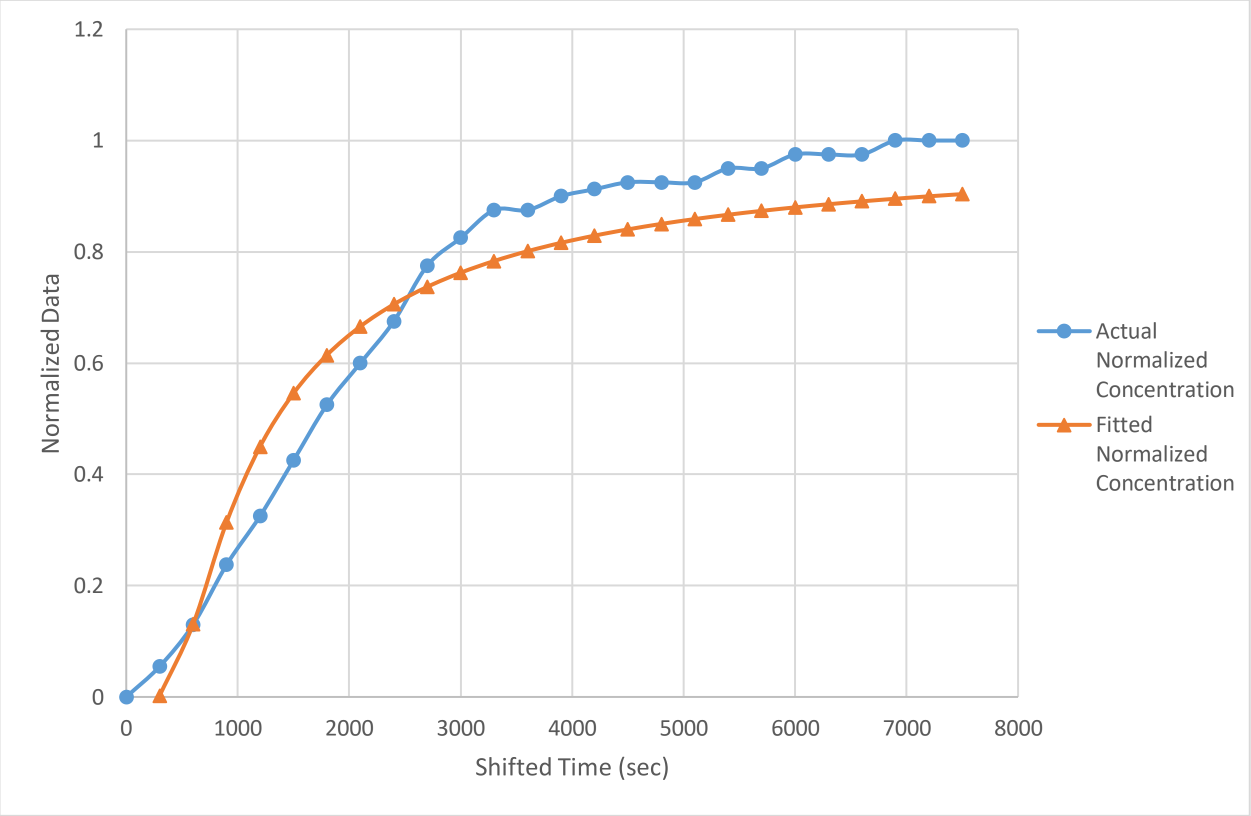

Figure B-3: *Trial 1 of 1.75 L/min Argon Flowrate with H=18 inches of soil*

Table B-4: *Trial 2 of 1.75 L/min Argon Flowrate with H =18 inches of soil*

Time (min)	Concentration (ppm)	Normalized Concentration	Shifted Time (sec)	FNC*	Sum of Squares
0	110	-0.003	-1500		
5	105	-0.006	-1200		
10	100	-0.008	-900		
15	100	-0.008	-600		
20	100	-0.008	-300		
25	115	0.000	0		
30	250	0.076	300	0.000	0.00568
35	375	0.146	600	0.069	0.00584
40	540	0.238	900	0.226	0.00015
45	700	0.328	1200	0.364	0.00129
50	800	0.384	1500	0.467	0.00699
55	950	0.468	1800	0.545	0.00593
60	1050	0.524	2100	0.604	0.00638
65	1100	0.552	2400	0.650	0.00957

70	1250	0.636	2700	0.686	0.00255
75	1300	0.664	3000	0.716	0.00275
80	1450	0.748	3300	0.741	0.00005
85	1500	0.776	3600	0.762	0.00019
90	1550	0.804	3900	0.780	0.00058
95	1600	0.832	4200	0.795	0.00135
100	1700	0.888	4500	0.809	0.00630
105	1700	0.888	4800	0.820	0.00457
110	1700	0.888	5100	0.831	0.00327
115	1700	0.888	5400	0.840	0.00230
120	1750	0.916	5700	0.848	0.00457
125	1800	0.944	6000	0.856	0.00777
130	1800	0.944	6300	0.863	0.00662
135	1850	0.972	6600	0.869	0.01065
140	1850	0.972	6900	0.874	0.00951
145	1900	1.000	7200	0.880	0.01448
150	1900	1.000	7500	0.884	0.01336
				Total Sum	0.133

*FNC = Fitted Normalized Concentration

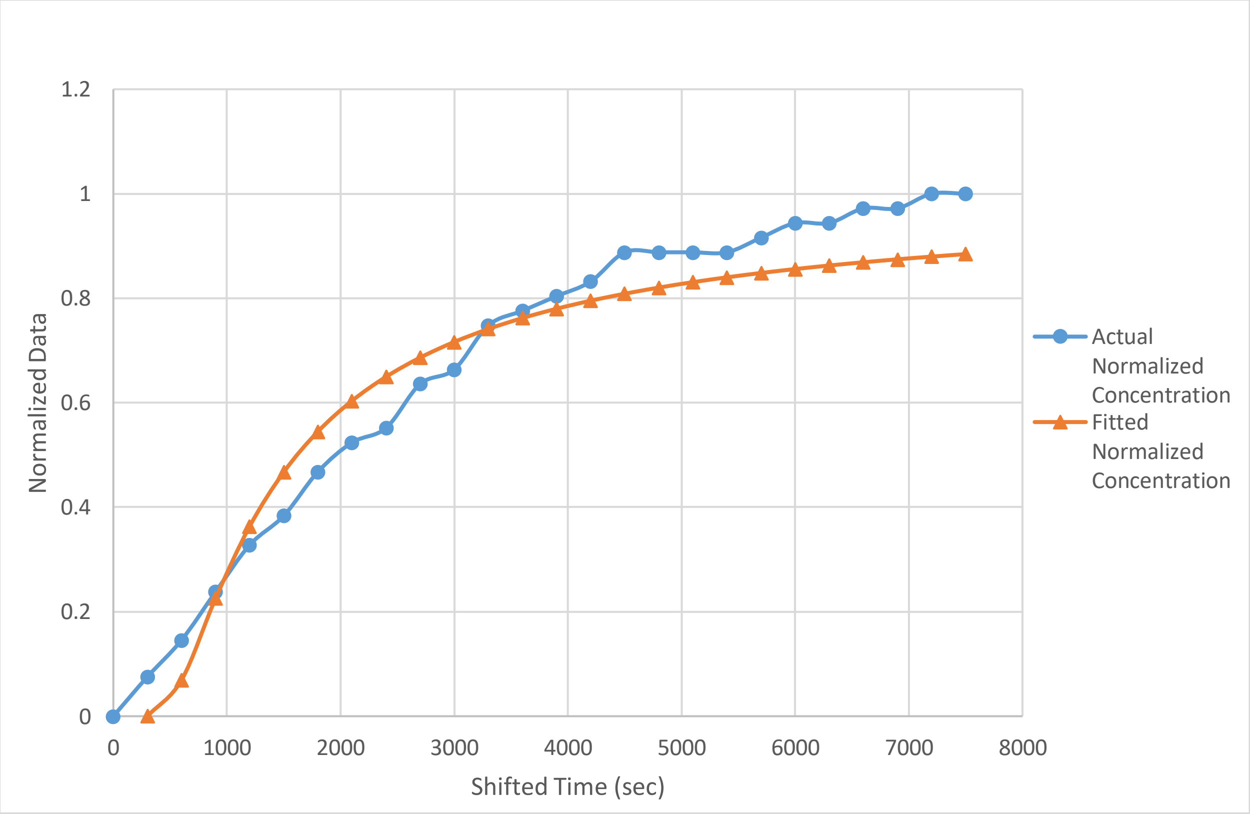

Figure B-4: *Trial 2 of 1.75 L/min Argon Flowrate with H =18 inches of soil*

Table B-5: *Trial 3 of 1.75 L/min Argon Flowrate with H=18 inches of soil*

Time (min)	Concentration (ppm)	Normalized Concentration	Shifted Time (sec)	FNC*	Sum of Squares
0	125	0.008	-1500		
5	110	0.000	-1200		
10	100	-0.005	-900		
15	90	-0.011	-600		
20	100	-0.005	-300		
25	110	0.000	0		
30	175	0.034	300	0.002	0.00104
35	350	0.127	600	0.125	0.00000
40	550	0.233	900	0.307	0.00551
45	750	0.339	1200	0.444	0.01103
50	950	0.444	1500	0.540	0.00912
55	1100	0.524	1800	0.610	0.00735
60	1250	0.603	2100	0.662	0.00341
65	1400	0.683	2400	0.702	0.00037
70	1500	0.735	2700	0.733	0.00000
75	1550	0.762	3000	0.759	0.00001
80	1650	0.815	3300	0.781	0.00117
85	1750	0.868	3600	0.798	0.00480
90	1800	0.894	3900	0.814	0.00648
95	1800	0.894	4200	0.827	0.00455
100	1800	0.894	4500	0.838	0.00314
105	1900	0.947	4800	0.848	0.00980
110	1900	0.947	5100	0.857	0.00812
115	1950	0.974	5400	0.865	0.01182
120	1950	0.974	5700	0.872	0.01034
125	1950	0.974	6000	0.878	0.00909
130	1950	0.974	6300	0.884	0.00802
135	1975	0.987	6600	0.889	0.00952
140	2000	1.000	6900	0.894	0.01123
145	2000	1.000	7200	0.898	0.01032
150	2000	1.000	7500	0.902	0.00952
				Total Sum	0.156

*FNC = Fitted Normalized Concentration

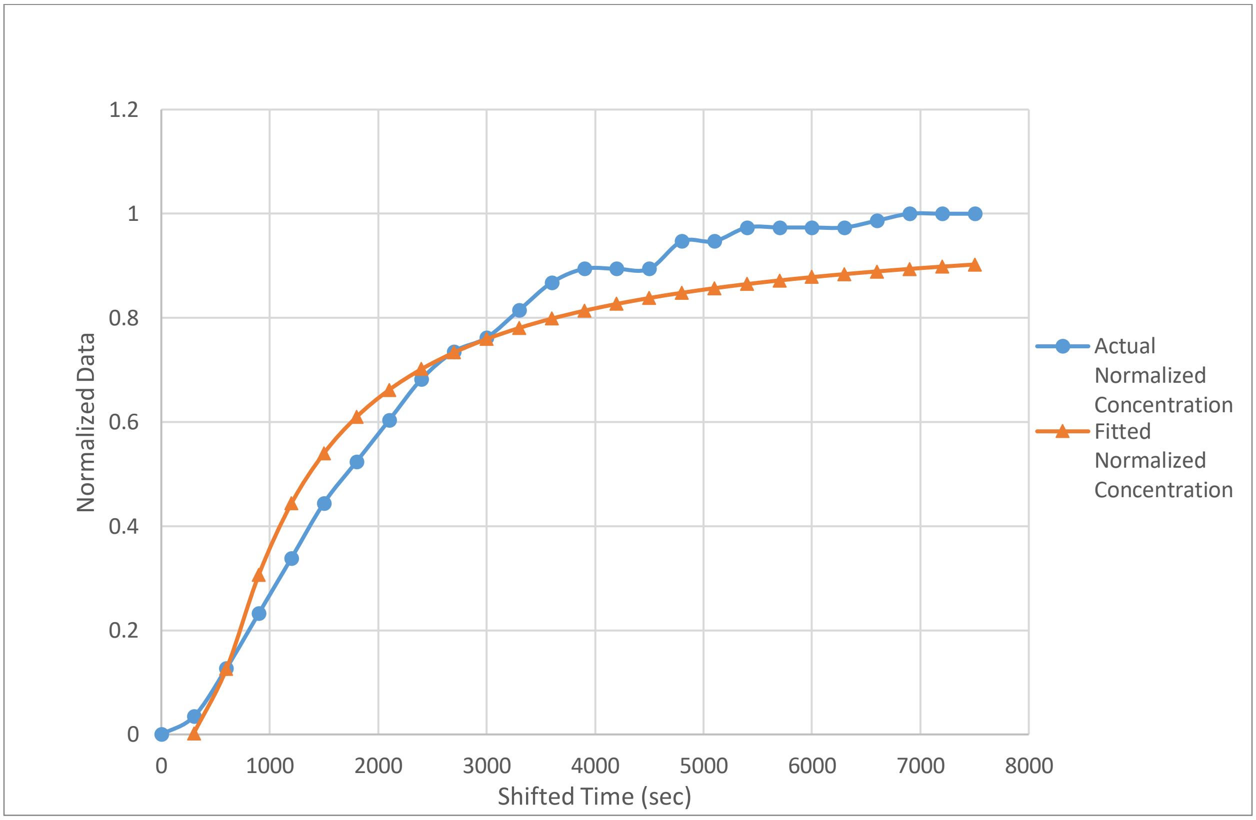

Figure B-5: *Trial 3 of 1.75 L/min Argon Flowrate with H=18 inches of soil*

Table B-6: *Trial 1 of 2.00 L/min Argon Flowrate with H =18 inches of soil*

Time (min)	Concentration (ppm)	Normalized Concentration	Shifted Time (sec)	FNC*	Sum of Squares
0	115	0.008	-1500		
5	105	0.003	-1200		
10	100	0.000	-900		
15	100	0.000	-600		
20	100	0.000	-300		
25	100	0.000	0		
30	140	0.022	300	0.001	0.00046
35	300	0.111	600	0.091	0.00042
40	485	0.214	900	0.259	0.00206
45	650	0.306	1200	0.398	0.00846
50	800	0.389	1500	0.499	0.01202
55	950	0.472	1800	0.573	0.01011
60	1050	0.528	2100	0.629	0.01020
65	1250	0.639	2400	0.672	0.00112
70	1400	0.722	2700	0.707	0.00023
75	1500	0.778	3000	0.735	0.00182
80	1500	0.778	3300	0.758	0.00038
85	1550	0.806	3600	0.778	0.00076
90	1550	0.806	3900	0.795	0.00012
95	1600	0.833	4200	0.809	0.00059
100	1700	0.889	4500	0.822	0.00454
105	1750	0.917	4800	0.832	0.00708
110	1800	0.944	5100	0.842	0.01045
115	1850	0.972	5400	0.851	0.01472
120	1850	0.972	5700	0.859	0.01290
125	1850	0.972	6000	0.866	0.01136
130	1875	0.986	6300	0.872	0.01303
135	1900	1.000	6600	0.878	0.01494
140	1900	1.000	6900	0.883	0.01368
145	1900	1.000	7200	0.888	0.01257
150	1900	1.000	7500	0.892	0.01159
				Total Sum	0.176

*FNC = Fitted Normalized Concentration

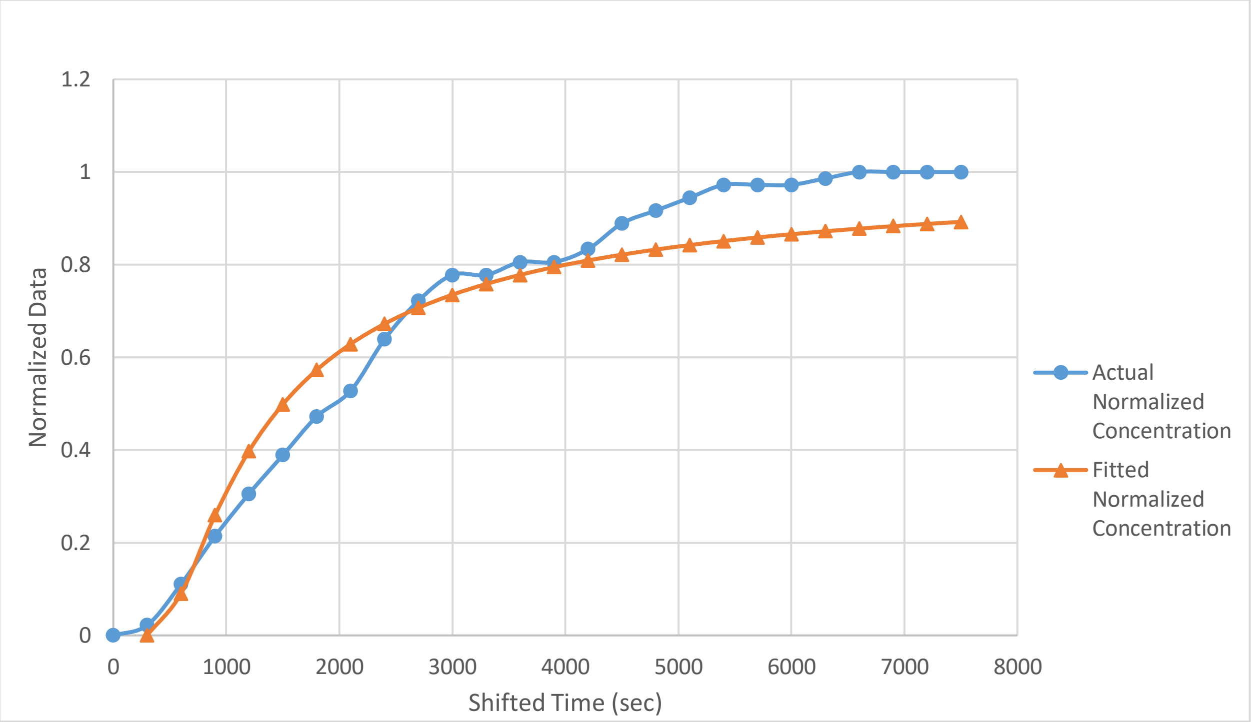

Figure B-6: *Trial 1 of 2.00 L/min Argon Flowrate with H =18 inches of soil*

Table B-7: *Trial 2 of 2.00 L/min Argon Flowrate with H=18 inches of soil*

Time (min)	Concentration (ppm)	Normalized Concentration	Shifted Time (sec)	FNC*	Sum of Squares
0	125	0.000	-600		
5	125	0.000	-300		
10	125	0.000	0		
15	250	0.065	300	0.01455	0.00253866
20	425	0.156	600	0.221823	0.00435318
25	650	0.273	900	0.415	0.020
30	850	0.377	1200	0.541	0.02712
35	1150	0.532	1500	0.625	0.00858
40	1350	0.636	1800	0.684	0.00225
45	1500	0.714	2100	0.727	0.00016
50	1600	0.766	2400	0.760	0.00004
55	1750	0.844	2700	0.786	0.00338
60	1850	0.896	3000	0.807	0.00795
65	1900	0.922	3300	0.824	0.00958
70	1950	0.948	3600	0.839	0.01197
75	2000	0.974	3900	0.851	0.01516
80	2000	0.974	4200	0.861	0.01267

85	2000	0.974	4500	0.871	0.01070
90	2000	0.974	4800	0.879	0.00910
95	2000	0.974	5100	0.886	0.00780
100	2000	0.974	5400	0.892	0.00672
105	2000	0.974	5700	0.898	0.00583
110	2000	0.974	6000	0.903	0.00508
115	2050	1.000	6300	0.907	0.00858
120	2050	1.000	6600	0.912	0.00782
125	2050	1.000	6900	0.915	0.00716
130	2050	1.000	7200	0.919	0.00658
135	2050	1.000	7500	0.922	0.00606
140	2050	1.000	7800	0.925	0.00561
145	2050	1.000	8100	0.928	0.00520
150	2050	1.000	8400	0.930	0.00484
				Total Sum	0.223

*FNC = Fitted Normalized Concentration

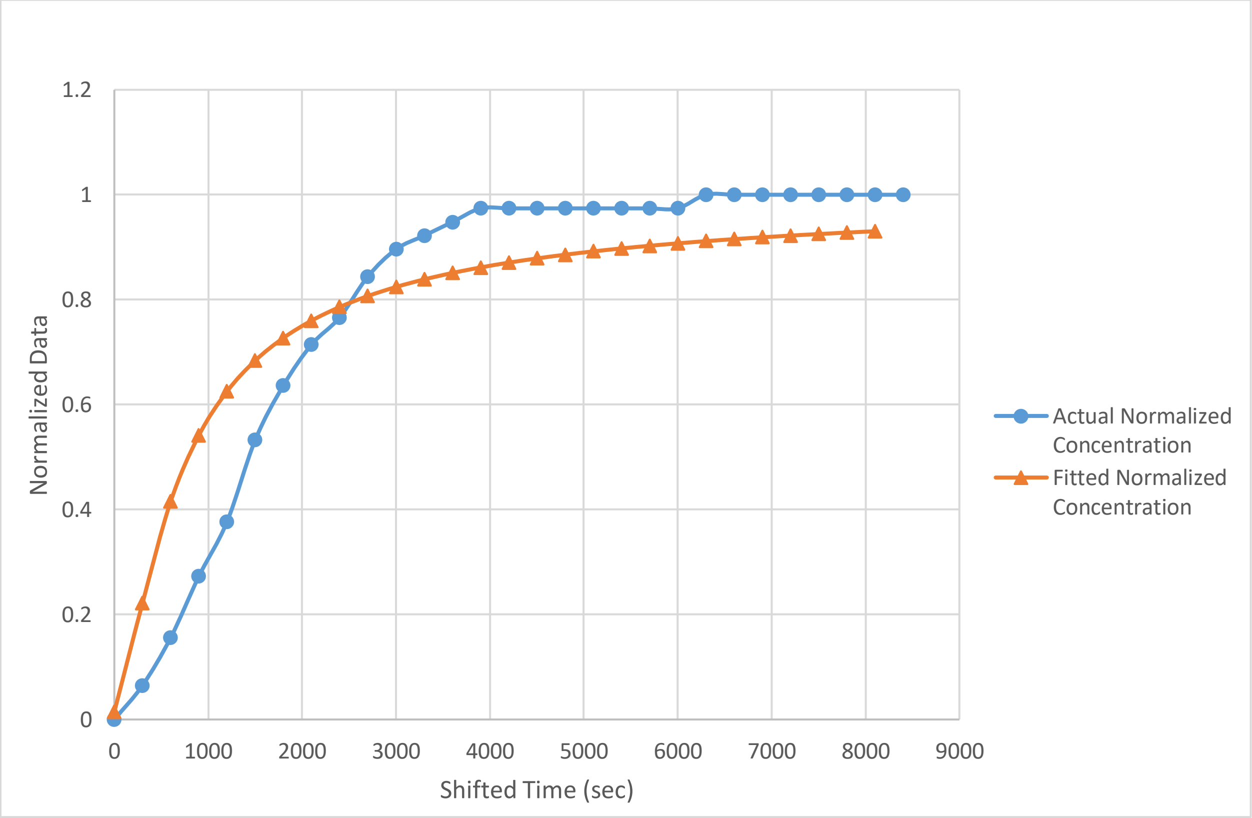

Figure B-7: *Trial 2 of 2.00 L/min Argon Flowrate with H=18 inches of soil*

Table B-8: *Trial 3 of 2.00 L/min Argon Flowrate with H= 36 inches of soil*

Time (min)	Concentration (ppm)	Normalized Concentration	Shifted Time (sec)	FNC*	Sum of Squares
0	35	0.026	-1200		
5	34	0.021	-900		
10	30	0.000	-600		
15	30	0.000	-300		
20	30	0.000	0		
25	32.5	0.013	300	0.000	0.000
30	32.5	0.013	600	0.000	0.000
35	35	0.026	900	0.000	0.001
40	35.5	0.028	1200	0.008	0.000
45	40	0.051	1500	0.034	0.000
50	50.5	0.105	1800	0.078	0.001
55	57.5	0.141	2100	0.130	0.000
60	69	0.200	2400	0.186	0.000
65	72.5	0.218	2700	0.240	0.000
70	75.5	0.233	3000	0.290	0.003
75	77.5	0.244	3300	0.336	0.009
80	81	0.262	3600	0.378	0.013
85	87.5	0.295	3900	0.415	0.015
90	89	0.303	4200	0.450	0.022
95	93	0.323	4500	0.480	0.025
100	97.5	0.346	4800	0.508	0.026
105	110	0.410	5100	0.533	0.015
110	125	0.487	5400	0.556	0.005
115	135	0.538	5700	0.577	0.002
120	140	0.564	6000	0.597	0.001
125	155	0.641	6300	0.614	0.001
130	195	0.846	6600	0.630	0.047
135	210	0.923	6900	0.645	0.077
140	225	1.000	7200	0.659	0.116
145	225	1.000	7500	0.672	0.108
150	225	1.000	7800	0.684	0.100
				Total Sum	0.586

*FNC = Fitted Normalized Concentration

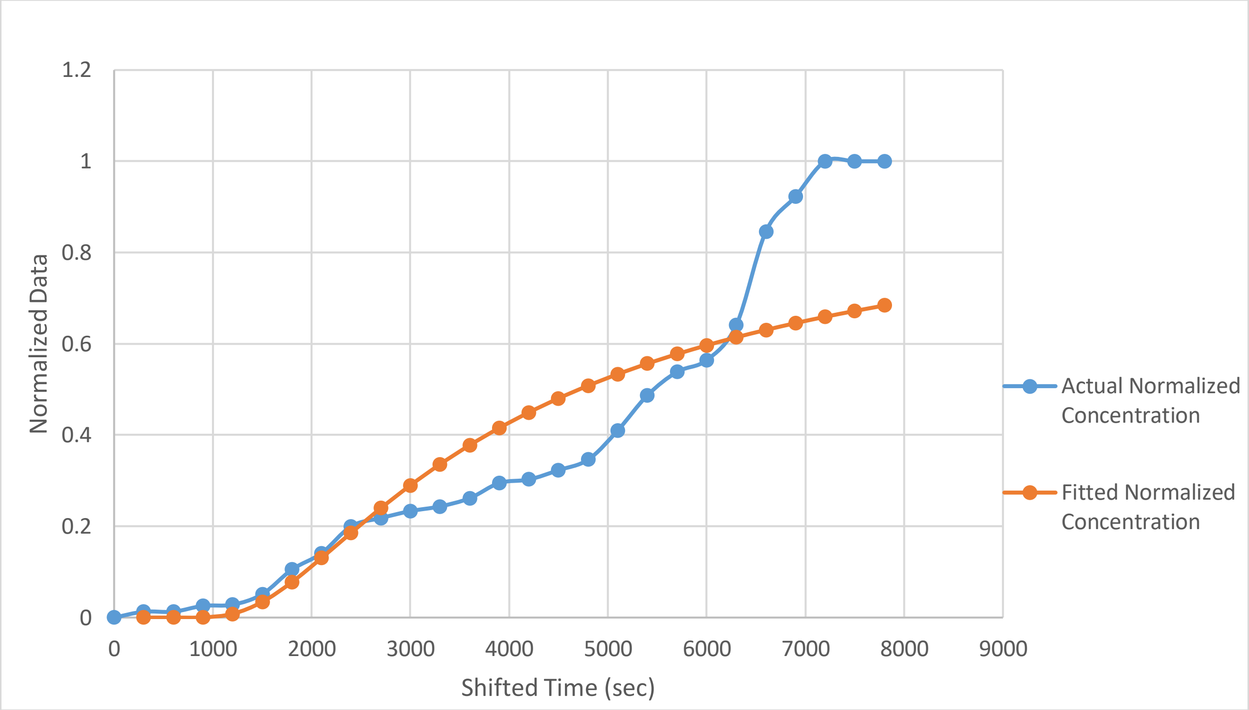

Figure B-8: *Trial 3 of 2.00 L/min Argon Flowrate with H= 36 inches of soil*